

Electronic Thesis and Dissertation Repository

11-24-2014 12:00 AM

Ultrasound-Guided Mechatronic System for Targeted Delivery of Cell-Based Cancer Vaccine Immunotherapy in Preclinical Models

Adem Nadjib Hadj Boussaad
The University of Western Ontario

Supervisor
James Lacefield
The University of Western Ontario

Graduate Program in Biomedical Engineering
A thesis submitted in partial fulfillment of the requirements for the degree in Master of Engineering Science
© Adem Nadjib Hadj Boussaad 2014

Follow this and additional works at: <https://ir.lib.uwo.ca/etd>



Part of the [Biomedical Devices and Instrumentation Commons](#)

Recommended Citation

Hadj Boussaad, Adem Nadjib, "Ultrasound-Guided Mechatronic System for Targeted Delivery of Cell-Based Cancer Vaccine Immunotherapy in Preclinical Models" (2014). *Electronic Thesis and Dissertation Repository*. 2530.

<https://ir.lib.uwo.ca/etd/2530>

This Dissertation/Thesis is brought to you for free and open access by Scholarship@Western. It has been accepted for inclusion in Electronic Thesis and Dissertation Repository by an authorized administrator of Scholarship@Western. For more information, please contact wlsadmin@uwo.ca.

ULTRASOUND-GUIDED MECHATRONIC SYSTEM FOR TARGETED DELIVERY OF
CELL-BASED CANCER VACCINE IMMUNOTHERAPY IN PRECLINICAL MODELS

(Thesis format: Monograph)

by

Adem Nadjib Hadj Boussaad

Graduate Program in Biomedical Engineering

A thesis submitted in partial fulfillment
of the requirements for the degree of
Master of Engineering Science

The School of Graduate and Postdoctoral Studies
The University of Western Ontario
London, Ontario, Canada

© Adem Nadjib Hadj Boussaad 2014

Abstract

Injection of dendritic cell (DC) vaccines into lymph nodes (LN) is a promising strategy for eliciting immune responses against cancer, but these injections in mouse cancer models are challenging due to the small target scale ($\sim 1 \text{ mm} \times 2 \text{ mm}$). Direct manual intranodal injection is difficult and can cause architectural damage to the LN, potentially disrupting crucial interactions between DC and T cells. Therefore, a second-generation ultrasound-guided mechatronic device has been developed to perform this intervention. A targeting accuracy of $< 500 \text{ }\mu\text{m}$ will enable targeted delivery of the DCs specifically to a LN subcapsular space. The device was redesigned from its original CT-guided edition, which used a remote centre of motion architecture, to be easily integrated onto a commercially available VisualSonics imaging rail system. Subtle modifications were made to ensure simple workflow that allows for live-animal interventions that fall within the knockout periods stated in study protocols. Several calibration and registration techniques were developed in order to achieve an overall targeting accuracy appropriate for the intended application. A variety of methods to quantify the positioning accuracy of the device were investigated. The method chosen involved validating a guided injection into a tissue-mimicking phantom using ultrasound imaging post-operatively to localize the end-point position of the needle tip in the track left behind by the needle. Ultrasound-guided injections into a tissue-mimicking phantom revealed a targeting accuracy of $285 \pm 94 \text{ }\mu\text{m}$ for the developed robot compared to $508 \pm 166 \text{ }\mu\text{m}$ for a commercial-available manually-actuated injection device from VisualSonics. The utility of the robot was also demonstrated by performing *in vivo* injections in mice.

Keywords

medical robotics, image-guided interventions, small animal imaging, high-frequency ultrasound, imaging phantom design and construction

Author's Contributions

My contributions to this research project include adapting the designs for a micro-CT guided needle-positioning robot for small-animal injections to function as an ultrasound-guided device with a specific end-user application in mind. The original CT-guided robot was designed for general purpose needle placement by Christopher Waring and Jeffery Bax in partial fulfillment of their respective Master's and PhD in Biomedical Engineering at Western University.

Jacques Montreuil was the lead machinist paired with me to replicate the high-tolerance components of the device. Alex Lyadski was tasked with installing the hardware and software of the robot's control system using the previous CT-guided system as a template; I provided supplementary support debugging software errors that held back progress.

Several aspects of the robot were modified to better adapt to end-user requirements and workflow. For example, I adapted the robot to perform injections using a large, near-zero dead-space Hamilton syringe rather than a cannula and tubing. I also enabled a robot-mounted needle to perform as an electric-contact sensor. This modification served its purpose in my newly developed needle calibration (**Figure 12**) and registration (**Figure 16**) techniques. I also designed and tested multiple techniques to validate the targeting accuracy of the ultrasound-guided injection robot (**Sections 3.2, 3.3, and 3.4**).

I undertook a 60 hour hands-on metal machining course at Fanshawe College to acquire the necessary skills to operate safely in the machine-shop setting at Robarts Research Institute. I also received training for an Objet-30 plastic 3D printer which I used thereon myself to fabricate parts rapidly when necessary. Following safety training, I used a GE eXplore RS scanner and Vevo 2100 micro-ultrasound scanner to acquire micro-CT and ultrasound images of various phantoms, respectively. The majority of phantoms were constructed by myself and prepared with a tissue-mimicking agar mixture by Mandolin Bartling, Lacefield Lab 2014 summer student.

Injection experiments into phantoms were designed by myself, and executed with the help of Mandolin Bartling. Mouse-handling and surgical procedures were performed by PhD Candidate, Matthew Lowerison, for *in vivo* experiments (**Section 3.6**).

Dedicated to my parents

Acknowledgements

I would like to thank the various individuals who have helped contribute to my graduate education and made my experience throughout my Master's pleasant and successful.

First, I would like to thank my supervisor, James Lacefield, for his close guidance throughout both my graduate and undergraduate careers. I would also like to thank my advisory committee, Aaron Fenster and Paula Foster, who generously lent the aid of their students and technicians to complete my project.

Thanks to all members of the Lacefield and Fenster labs. Special thanks to Matthew Lowerison for his expert help in surgical planning for small-animal interventions. Thanks to Jeff Bax whose experience in mechanical design was invaluable, and to Jacques Montreuil and Chris Blake for their aid in high-tolerance machining and lending their knowledge of practical fabrication processes. Alex Lyadski's electronics configuration and David Tessier's technical support is also greatly appreciated.

Thanks to Joseph Umoh and John Moore for their training in safe use of the micro-CT scanners and 3D printer, respectively. Thanks to the Lacefield Lab's summer student, Mandolin Bartling, for patiently spending many hours acquiring ultrasound images.

This research was supported by the Ontario Preclinical Imaging Consortium funded by the Ontario Research Fund, the Canadian Institutes of Health Research, the NSERC-CREATE Training Program in Computer Aided Medical Interventions, and the Ontario Graduate Scholarship program.

Table of Contents

Abstract	ii
Author’s Contributions	iii
Acknowledgements	v
Table of Contents	vi
List of Figures	ix
List of Acronyms & Abbreviations	xiv
1 Introduction	1
1.1 Motivation.....	1
1.2 Preclinical Image Guidance Modalities	2
1.2.1 MRI Guidance.....	2
1.2.2 Micro-CT Guidance	4
1.2.3 Ultrasound Guidance	5
1.3 Review of Current Preclinical Technologies	7
1.4 Registration	11
1.5 Image Artifacts in Ultrasound.....	15
1.6 Dendritic-Cell Cancer Vaccine Immunotherapy Research.....	21
1.7 Thesis Objectives	22
1.8 Thesis Outline	22
2 Adaptation of Robot for Ultrasound Guidance	24
2.1 Mechanical Hardware	24
2.2 Remote Centre of Motion Needle Calibration	28
2.2.1 Earlier Generation Techniques: Camera Calibrations and Fixture-Based	28
2.2.2 Electrical-Contact Calibration	29

2.2.3	Compensation for Needle Bevel	29
2.3	VisualSonics Rail System Error.....	32
2.4	Registration Approach	33
2.4.1	Two-Step Registration Phantom.....	33
2.4.2	One-Step Registration.....	36
3	Targeting Accuracy Experiments.....	39
3.1	Air-Track Intersection Targeting Phantom.....	39
3.2	Physical Micro-CT Validation Markers.....	41
3.3	Use of Contrast Agents for Micro-CT Validation	44
3.4	High-Frequency Ultrasound for Validation of Needle Tracks in Tissue-Mimicking Phantoms.....	46
3.5	Targeting Accuracy of Ultrasound-Guided Robot Versus VisualSonics Micromanipulator	49
3.6	Ultrasound-Guided Robotic and Manual Injections Performed on Mice	53
4	Summary, Conclusions, and Future Work	58
4.1	Summary and Conclusions	58
4.1.1	Mechanical Hardware	58
4.1.2	Calibration.....	59
4.1.3	Registration.....	60
4.1.4	Targeting Experiments.....	61
4.2	Future Work	64
4.2.1	Ultrasound-Guided Interventional Platform Modifications.....	64
4.2.2	Compensation of Tissue Deformation	65
4.2.3	Clinical Translation.....	67
4.3	Conclusion	68
	References	69

Curriculum Vitae 72

List of Figures

- Figure 1:** (a) Two 3D volumes differ in translation and rotation. Selecting fiducial landmarks using easily detected features (red and blue dots), it is possible to perform a rigid registration for alignment (b)..... 12
- Figure 2:** Ultrasound registration phantom by Waspe *et al.* [29]. Phantom was scanned in micro-CT pre-operatively to determine the spatial relationship between the needle tip and fiducial beads. 13
- Figure 3:** (a) Orienting a needle parallel to the ultrasound transducer provides for optimum visualization. (b) However, accurate visualization becomes more difficult as the angle of incidence increases. (c) Beam steering can be used to compensate for this angular offset. (d) There has also been promising progress in the development of ‘echogenic’ needles. In the case depicted above, small grooves act as miniature reflectors overcoming the needle insertion angle to reflect the ultrasound back to the transducer (Adapted from Reusz et al. [48])..... 16
- Figure 4:** (a) Tissue mimicking phantom containing two plastic cones. (b) The occurrence of an air bubble near the transducer face results in a ring-down artifact, hiding underlying features. 17
- Figure 5:** Chicken embryo vertebrae imaged in ultrasound using a VisualSonics MS-250 transducer. Acoustic shadowing appears distal to each vertebra. 17
- Figure 6:** (a) Graphic depicting physical theory behind reverberations. Back-and-forth reflections between a highly reflective surface and the transducer face causes equally-spaced reverberation artifacts that diminish in amplitude with each occurrence. (b) The surface of a tissue-mimicking phantom causes a reverberation artifact beneath. 18
- Figure 7:** (a) Graphic depicting physical theory behind needle reverberations. Subsequent reflections between the interior and exterior walls of the needle result in echoed signal that diminishes with each round trip. (b) Micro-ultrasound image of 30 gauge conical needle imaged near-parallel to the transducer. (Adapted from Reusz et al. [48])..... 19
- Figure 8:** Cross-sectional view of needle imaged using high-frequency ultrasound. (a) Illustrates how the needle can still be detected by transducer subapertures it is not directly distal to via side lobes (red) even though it is missed by their main lobe (blue). This leads to the side lobe artifacts shown in (b). (Adapted from Reusz et al. [48])..... 20
- Figure 9:** (a) Solidworks model of original 2nd generation image-guided injection robot designed for micro-CT. (b) Solidworks model of original needle driver mechanism. Needle is inserted to RCM position. 24

Figure 10: VisualSonics provides a railing system equipped with an adjustable transducer arm and manual needle manipulator. A specialized mouse stage allows for easy anaesthesia and ECG monitoring. The VisualSonics motor allows for 3D image acquisition by stepping the MS-550D transducer at small increments. This transducer is generally used for mouse abdominal, reproduction, tumour, and vascular imaging as well as some similar rat applications. 25

Figure 11: (a) Solidworks model of new ultrasound-guided needle positioning robot. (b) Solidworks model of modified needle driver mechanism mounted external to the robot’s spherical linkages. A linkage joint was hollowed to allow the near-zero dead-space Hamilton syringe to pass through. 27

Figure 12: Overview of RCM needle calibration technique developed for the ultrasound-guided device. The top surface of the conductive plate meets the RCM point. Contact between the needle tip and plate is detected by a multimeter. The closed circuit path is such: multimeter → brass bushing → steel needle → aluminum plate → multimeter. 29

Figure 13: Micro-CT image of 30G needles with 12° bevel angle. Offset was determined by calculating the axial distance between the centre of the lumen and the needle tip. 30

Figure 14: (a) Solidworks model of calibration tool designed to shift the RCM calibration of a bevelled needle mounted on the robot from its tip to the centre of its lumen. (b) Conductive brass block with two precisely placed locating pinholes on either side. The distance between each pinhole and its corresponding side face differed by the lumen-tip offset (666 μm) previously measured in micro-CT. 31

Figure 15: Boxplot comparing the localization error found from consecutive 3D scans of a bead-phantom with the localization error found when removing and repositioning the transducer over the phantom by gliding it along its railing system. 32

Figure 16: (a) Micro-CT slice of first-generation two-step registration phantom at 49.6 μm isotropic voxel size. (b) Solidworks representation of registration phantom. Each electronic pad is connected to multimeter set to Continuity Test. 33

Figure 17: Ultrasound and CT scans of the phantom are linked by a rotation (R1) and translation (T1), while the CT scan of the phantom and the robotic workspace are linked by a rotation (R2) and translation (T2). (a-i) Rendering of 3D ultrasound scan of phantom. (a-ii) Multiplane view of micro-CT scan of phantom. (a-iii) Prototype registration setup. (b) The two-step rigid registration process produced an overall FRE and TRE of $146.23 \pm 73.86 \mu\text{m}$ and $135.38 \pm 47.83 \mu\text{m}$, respectively. 34

Figure 18: Cross-sectional view of second-generation registration phantom containing 8 outer fiducial beads and 4 inner target beads (observable in ultrasound and micro-CT). Six 2 mm ∅ steel rods were sharpened at each end to create 8 fiducial, and 4 target, ~50 μm ∅ point-like pads (observable in micro-CT and detectable by the robot’s end-effector). 35

Figure 19: Cross-sectional view of 27 gauge needle, N, and 400 μm tungsten bead, B, scanned in (a) high-frequency ultrasound and (b) micro-CT. A phantom was constructed to determine the error introduced by ultrasound artifacts in localizing a needle lumen in ultrasound versus CT. Ten ultrasound images of the phantom were registered to its micro-CT scan and a Mann-Whitney rank-sum test (c) showed that there is a significant increase ($p < 0.001$) in error when localizing a lumen in ultrasound versus fiducial beads (by $\sim 50 \mu\text{m}$)..... 37

Figure 20: The robot stages are used to move the needle tip to multiple positions in the 3D ultrasound field of view. At each point, the needle tip’s lumen centre is localized to collect a fiducial point in ultrasound, while also recording the stage coordinates. Eventually, a common point set is obtained to perform a rigid-body point-based registration..... 38

Figure 21: (a) Solidworks model of air-track intersection targeting phantom. (b) Micro-CT slice of targeting phantom with pixel intensities negated. Faint white lines indicate grid pattern of $100 \mu\text{m}$ \varnothing air channels. (c) Single side-view slice of targeting phantom in micro-CT (negated). Poor contrast between the air channels and surrounding agar mixture prevented from accurate localization of an intersection target. (d) Single ultrasound frame depicting a typical intersection of air-channels for targeting experiments. (e) Rendering of 3D ultrasound image of targeting phantom. Compared to micro-CT, ultrasound volumes of the phantom contain enough contrast to localize a target accurately and repeatedly. 39

Figure 22: Micro-CT image acquired after injection of barium into air-track intersection targets showing estimation of needle targeting errors. (Adapted from Waspe et al. [38])...... 41

Figure 23: Solidworks model of Hamilton syringe adapted to deposit concentrically sharpened steel pellets. Design was based on ‘stacking pencil’ 42

Figure 24: (a) Solidworks model of plastic sheath and silver crimp marker fitted onto a needle. (b) Micro-CT isosurface of silver crimp segmented in MicroView. (c) Transparent Solidworks view of sheath and crimp marker on a needle. The sheath is 3D printed such that the needle tip is placed roughly at the centroid of the surrounding silver crimp..... 43

Figure 25: (a) Micro-CT image of agar phantom enhanced with iodine contrast agent. A 30 G needle was used to pierce its surface. (b) Micro-CT image of iodine-enhanced phantom pierced with 18 G needle. This technique could be used to localize needle-track tips in micro-CT for clinical applications, but not preclinical. (c) Anechoic iodine-agar phantom in ultrasound. (d) Tungsten-agar phantom in high-frequency ultrasound. 44

Figure 26: Mean needle track endpoint FLE in ultrasound and CT for different needle gauges. (One-way ANOVA, Krustal-Wallis, multiple comparisons. *: $p < 0.05$, ****: $p < 0.0001$, error bars denote standard deviation of 10 trials). 45

Figure 27: Micro-CT image of Microfil $\text{\textcircled{R}}$ contrast agent used in tissue-mimicking phantoms to reveal needle tracks..... 46

Figure 28: (a) Ultrasound frames of 30G needle inserted into a tissue-mimicking phantom. (b) Needle being removed from phantom, leaving a distinct track that may be localized to estimate where the needle tip was positioned. The Euclidean distance between the needle tip localization and the track tip is the ‘Track-Needle Error’. Ultrasound cine loop of this procedure indicated no deformation of the tracks or surrounding phantom material. 47

Figure 29: Steel (a) and 3D-printed plastic (b) needles inserted into an agar phantom. Plastic needles appear to result in slightly less artifacts; however, this did not improve needle-tip localization. 47

Figure 30: (a) Image of 3D printed plastic needle (left) next to 30G steel needle (right). (b) Solidworks wireframe schematic of plastic needle. 48

Figure 31: (a) Boxplot depicting the FLE estimate from localizing metal needles, plastic needles, and needle tracks in ultrasound. A nonparametric one-way ANOVA (Kruskal-Wallis) found no significant difference ($p = 0.3241$) between each FLE. (b) Boxplot depicting the track-needle errors found when using both metal and 3D-printed plastic needles. A nonparametric Mann-Whitney test found no significant difference ($p = 0.9873$) between the track-metal needle and track-plastic needle errors. 49

Figure 32: Solidworks model (a) and ultrasound image (b) of targeting phantom. The vertex of each cone is localized to determine the midpoint virtual target for needle placement. 50

Figure 33: Ultrasound image of a lymph node located within the mammary fat pad of a mouse. The cross-sectional inner-diameter measurements of $0.885 \text{ mm} \times 1.714 \text{ mm}$ indicate the size and position of the lymph nodes. A 30 gauge needle on the left-hand side of the image has been localized within the VisualSonics software, generating an estimated path when driven forward into the lymph node. In this example image, this was the maximum advancement of the needle just prior to the manual manipulator contacting the transducer’s side. 50

Figure 34: A nonparametric Mann-Whitney test yielded a significant difference ($p = 0.0029$) between the targeting accuracy of robot and manual injections into tissue-mimicking phantoms. Their means (bars) and standard deviations (error bars) are $285 \pm 94 \mu\text{m}$ and $508 \pm 166 \mu\text{m}$, respectively. Dotted line denotes design goal of 0.5 mm maximum targeting error. 51

Figure 35: Boxplot depicting the error found when comparing the localization coordinate of a needle tip in ultrasound during an injection into a phantom with the localization of the tip of the track left behind after removal of the needle from the phantom; the manual injection accuracy; and the robotic-aided injection accuracy. A one-way ANOVA showed a significant difference between the track-needle error and manual injections, but not with robotic injections. (*: $p < 0.05$ **: $p < 0.01$, error bars denote standard deviation of 10 trials). 52

Figure 36: (a) Photograph of mouse surgical preparation prior to ultrasound-guided injection. (b) Illustration of manual injection setup. The solid black line section indicates the region of incision through the dermal layer. The dotted black line indicated where this flap of skin was pinned during the injection. The dotted red line indicates the placement of the ultrasound transducer. The needle is advanced in-plane to the ultrasound image between the transducer face and the mouse’s body towards the lymph node..... 54

Figure 37: Photograph of ultrasound-guided manual injection in mouse. The needle is carefully positioned between the transducer and the mouse..... 55

Figure 38: Ultrasound frames of VisualSonics’s micro-manipulator manual injection into inguinal lymph node located within the mammary fat pad of a mouse (~ 0.8 x 1.3 mm internal diameter). When visualising such a small target, it is difficult to make adjustments such that both the target and the needle are within the field of view. The needle must be angled appropriately at an inclination that allows the syringe to avoid hitting the transducer upon being driven forwards and for the target to be reached. In (a), a short length of the cannula is visible to position two points (green +) along the shaft to create a projected trajectory (green dashed line). In (b), the needle has been driven through the mammary fat pad and the bevelled tip is buried within the lymph node. Considerable deformation has taken place, and the initial guess (red ‘x’) as to the required needle insertion depth has been overshoot by 1.5-2.0 mm. 55

Figure 39: (a) Photograph of robotic injection into anaesthetised mouse’s lymph node targeted using high-frequency ultrasound as the guidance modality. (b) Close-up of robotic injection..... 57

List of Acronyms & Abbreviations

ANOVA	analysis of variance
2D	two-dimensional
3D	three-dimensional
CCD	charged coupled device
CT	computed tomography
FLE	fiducial localization error
FRE	fiducila registration error
LV	left ventricle
MRI	magnetic resonance imaging
RCM	remote centre of motion
ROI	region of interest
RMS	root mean squared
SNR	signal-to-noise ratio
TRE	target registration error
DOF	degrees of freedom
WBC	white blood cell
T-cell	thymus cell
T1, T2	translation 1, translation 2
R2, R2	rotation 1, rotation 2
FOV	field of view

1 Introduction

In this thesis, a general-purpose CT-guided injection robot, collaboratively developed by the Lacefield and Fenster labs at Robarts Research Institute, was adapted to perform high-frequency ultrasound-guided injections with a specific application in mind. The end-user, an immunology collaborator, required a device suitable for image-guided, minimally-invasive injections of dendritic-cell cancer vaccines into the lymph nodes of mouse models. Several hardware design modifications were made to accommodate preclinical-intervention constraints. Calibration, registration, and validation techniques were also developed to meet the end-user workflow demands.

1.1 Motivation

Preclinical studies of new therapies and pharmaceuticals are performed to determine their safety and effectiveness. These studies are often taken for granted but are necessary to justify translation of new treatments to the clinical setting [1]. Preclinical research often involves the injection of substances, such as cancer cells, stem cells, or contrast agents [2] [3] into small-animal disease models. The current gold standard for microinjections involves surgically exposing the target of interest; however, minimally invasive procedures are preferable since they are believed to better preserve physiologic and immune functions.

Image-guided approaches exist, such as in the use of ultrasound imaging, but they are normally done freehand [4] or through the use of a manually actuated manipulator [5]–[7]. Manual injections are susceptible to poor accuracy and high variability, which can damage internal organs and confound results. Alternatively, accurate use of stereotactic devices, while relatively precise, typically relies on anatomical knowledge to accurately place a needle within a target [8]. Ultimately, percutaneous injections are highly dependent on operator skill and training, which differs wildly from person to person.

Medical robotics is a well-established field that has successfully combined the accuracy and repeatability of robotics with a variety of imaging modalities for guided procedures – many of which have been adopted in the clinical setting. While workflow requirements are comparable, if

not more lenient when dealing with small animals, image-guided preclinical robotics provides a unique challenge in that it requires a positioning accuracy and image resolution an order of magnitude better than is necessary in the clinical setting (30 -100 μm is required to obtain images of rodents equivalent to a 1 mm voxel size in humans [9]) due to the small scale of common targets of interest (**Table 1**). While developments in the imaging field have met this standard, there is much room for improvement in terms of robotic designs.

Table 1: Representative intervention targets and dimensions in mice, adapted from [4]. \emptyset denotes target diameter. Cardiac dimensions are thicknesses measured in the long axis view.

Target	Dimension (mm)
Tumours (initial detected diameter)	\emptyset 0.22 – \emptyset 2.4
Mesenteric veins	\emptyset 0.2
Embryonic Cavity (E7.5)	\emptyset 0.3
Ascending Aorta (systole)	\emptyset 1.5
Common carotid artery	\emptyset 0.5
Left ventricle end-diastole (LV-ED)	\emptyset 3.8
Left ventricle end-systole (LV-ES)	\emptyset 2.5
Anterior wall (LV-ED)	0.86
Posterior wall (LV-ED)	0.74
Anterior wall (LV-ES)	1.36

1.2 Preclinical Image Guidance Modalities

1.2.1 MRI Guidance

Magnetic resonance imaging (MRI) is an imaging technique that utilizes strong magnetic fields and radio-frequency pulses to acquire anatomical and functional information from a patient without exposure to harmful radiation. The three-dimensional (3D) imaging capability of MRI

allows for an advantage over typical two-dimensional (2D) techniques, such as most ultrasound systems and X-ray fluoroscopy, during pre-operative planning for minimally invasive procedures. MRI relies on the water content and local magnetic properties of a body region of interest [10], making it an ideal tool for viewing soft tissue.

The large scaling difference between human patients and small animals introduces several challenges to using MRI guidance for preclinical interventions. In order to achieve the necessary spatial resolution, the voxel size must be reconstructed to be much smaller, resulting in a lower signal-to-noise ratio (SNR). High-field MRI scanners have been developed to compensate for this SNR loss by operating at fields of 11 T. However, the necessarily small bore size limits workspace and makes robotic design prohibitive [11]. It is also possible to adapt clinical scanners for preclinical application through the use of specialized gradient coils.

Complementary to MRI are hybrid imaging systems such as single-photon emission computed tomography (SPECT) and positron emission tomography (PET) imaging. SPECT and PET both require the injection of radiotracers to produce 3D images with contrast dependent on the concentration of the radiotracer in target areas of the body. The major difference between the modalities is that SPECT, in comparison to PET, can be performed using radiotracers that are more readily available to most research groups due to lower cost. However, SPECT imaging is at much lower resolution than PET (~10 mm compared to ~1 mm, respectively). Studies are often performed using MRI with either SPECT or PET. The reason is to combine MRI's high resolution, soft-tissue contrast (but low sensitivity to metabolic activity) and SPECT or PET's high sensitivity (despite low resolution). The popularity of such image fusion methods has led to hybrid systems that perform PET and MR imaging in the same machine. Work is currently being done to achieve the same fusion of SPECT with MRI [12]. Huang *et al.* [13] developed a device that uses combined MR and PET images for guidance in small animal biopsies. The device was found to have a positioning error of 1.20 ± 0.39 mm in a tissue mimicking phantom and the authors concluded the current system was not suitable for animal interventions [13]. Robotic devices using hybrid MR-guidance are not in routine use for small animal interventions.

1.2.2 Micro-CT Guidance

The development of CT imaging revolutionized clinical medical imaging and its inventors were awarded the Nobel Prize in 1979. However, the approximately 1 mm spatial resolution of clinical CT scanners limits their effectiveness in preclinical small animal imaging. For instance, an order of magnitude smaller voxel size of 30 - 100 μm is required to obtain images of rodents equivalent to a 1 mm voxel size in humans [9]. To address the shortcomings of CT in small animal imaging, the first micro-CT system with μm -scale spatial resolution was developed in 1982 [14]. Since then, there has been an exponential growth in the yearly publications on the topic and commercial availability of micro-CT scanners from at least one dozen manufacturers [15]. Typical scanners are available with voxel sizes ranging from 5 μm to 450 μm . Decreasing the voxel size of images also decreases the trans-axial scanner field of view. Typical trans-axial fields of view range from 1 to 20 cm [16].

Micro-CT scanners measure the attenuation of X-ray beams by a specimen at hundreds of angular views and use a reconstruction algorithm to produce a 3D image [9]. As a result, micro-CT scanners possess a number of unique strengths and weaknesses. Micro-CT images can be acquired at a high spatial resolution, which is valuable in localizing targets for interventions. Micro-CT is well suited for image-guided interventions requiring differentiation between tissues with large differences in X-ray attenuation. At X-ray intensities suitable for living tissue, micro-CT is well suited for differentiation between air (i.e. lungs), fatty tissue, non-fatty tissue (i.e. muscle), and bone. However, micro-CT provides limited contrast within these groups and is therefore not ideal for many abdominal interventions. The use of contrast agents with high X-ray attenuation such as iodine and barium have proved useful in visualizing soft tissues such as vasculature and the gut [14]. The use of micro-CT exposes animals to ionizing radiation which can result in physiological effects that confound the results of experiments [17]. The small bore size of micro-CT makes the development of an interventional device difficult. Finally, micro-CT cannot acquire images in real time which prevents real time monitoring and correction during interventions. The strengths and weaknesses of micro-CT must be carefully considered when determining its suitability for guidance during an intervention.

1.2.3 Ultrasound Guidance

Micro-ultrasound operates using the same principles as traditional clinical ultrasound imaging. However, micro-ultrasound imaging for small animals uses specialized transducers with higher frequencies than clinical systems (20-60 MHz) to increase the spatial resolution and allow clear identification of structures of interest [18]. The higher lateral resolution of 65 μm (for 50 MHz) to 140 μm (for 20 Mhz) provided by the higher frequencies makes this a useful tool for small animal imaging and needle guidance. However, these higher frequencies also have an associated lower penetration depth of < 20 mm. Ultrasound imaging creates tissue contrast based on differences in density and compressibility (and, hence, acoustic impedance) of adjacent tissue structures and is commonly used to visualize muscles, tumors, and many internal organs. A micro-ultrasound system is safe, portable, and is cost-effective compared to other micro-imaging systems such as CT or MRI. Ultrasound is strongly reflected by high changes in acoustic impedance making it not suitable for bone specific imaging such as transcranial imaging and imaging of bony interfaces. Furthermore, imaging of gas filled organs such as the lungs and intestines also suffer from poor image quality and high attenuation.

Ultrasound offers several imaging techniques including: one-dimensional imaging (M-mode) to provide high temporal resolution needed in cardiovascular research, 2D imaging (B-mode) to visualize anatomical structures, 3D static and real-time imaging to capture their size and structure, and 4-D color Doppler imaging to provide information about blood flow through vessels. To image capillaries, the sensitivity and specificity of ultrasound can be further increased with the injection of gas-filled microbubble contrast agents [19]. This is commonly referred to as contrast-enhanced ultrasound and it relies on specific pulsing sequences to increase the contrast-to-tissue ratio. In addition, microbubbles can be conjugated to markers for site specific targeting of imaging to provide molecular visualization or delivery of therapeutic agents [20].

Micro-ultrasound is used to guide freehand percutaneous micro-injections of drugs [6], [7], [21], stem cells, or contrast agents into animals without the need for surgical intervention [12], [22]. Micro-ultrasound is exceptional among imaging modalities for its routine use in needle guidance due to its real-time imaging capabilities. Despite the advantages of micro-ultrasound, its use as a guidance modality for preclinical robotic systems is not evident in the literature. Potential

reasons include: smaller margins of error make clinical tool-tracking techniques (optical tracking, electromagnetic tracking) insufficient for the accuracy requirements [23], disproportionate effects of needle artifacts and shadowing on image quality, and limited workspace due to the smaller imaging field of view.

The Vevo 2100 ultrasound system (VisualSonics Inc., Toronto, ON) used in this thesis utilizes a linear array transducer to acquire high-frequency, high-resolution, ultrasound images. While the typical clinical scanner operates at frequencies ranging from 1 MHz to 15 MHz, yielding an optimal resolution of around 200 μm [24], it cannot be used to resolve various preclinical structures of interest (see **Table 1**). The Vevo 2100 is custom designed for preclinical imaging and uses a modular transducer design optimised to the imaging application. The MS-550D transducer used in this thesis is a 256 element linear array transmitting at a 40 MHz centre frequency to achieve a nominal resolution of $40 \times 80 \times 180 \mu\text{m}^3$ in the axial, lateral, and elevational axes, respectively. The maximum imaging depth is 15 mm; however, image quality degrades after 10 mm. This is due to the geometric focus being at 7mm, and that the SNR worsens as the limit of the penetrative depth is approached for a given frequency. The system can produce multiple transmit foci, and achieves a near-uniform lateral resolution through dynamic receive focusing [24]. Focusing in the elevational direction is achieved with a fixed focus lens.

The VisualSonics system has the potential to serve as an excellent tool for interventional needle guidance as it is capable of acquiring a rapid series of B-mode slices as it is stepped along the elevational axis by a step motor, allowing for the reconstruction of a three-dimensional image. This is optimal when used for the guidance of a robotic device as it provides the preferable three-dimensional fiducial pattern for registration, which is discussed later. VisualSonics provides a variety of analysis toolkits that may be used for interventional planning, giving the user the ability to view the internal anatomy and select targets within the mouse. B-mode imaging can also be used in real-time (300 Hz maximum frame rate); this rapid acquisition allows for continual imaging of the target region while the intervention is being performed which may be used as feedback to control needle position or velocity.

1.3 Review of Current Preclinical Technologies

A need for small-animal image-guided robotic systems exists, and as a result designs for this application have emerged in the literature. Below is a review of the systems that differ in the imaging modality used, which influences the design of the robot itself due to inherent constraints.

With exception of the device by Rodriguez *et al.* [22], needle insertions under ultrasound guidance are typically performed using a dedicated system where the ultrasound transducer and needle guide are supported by a manually actuated positioning device [6], [7], [25], [26]. The ultrasound-guided device by Rodriguez *et al.* is only used to support the ultrasound probe while the needle is inserted free-hand. None of these designs are robotic, and require manual manipulation of the needle and ultrasound transducer.

A few dedicated systems for CT-guided interventions exist, but their routine use has not yet been adopted by preclinical researchers. However, dedicated systems do exist to perform radiation therapy in small animals. The robots in this category support both the X-ray tube, which is used for imaging and radiation therapy, and the detector [27]. By combining imaging and therapy in the design of the robot, errors due to image registration and repositioning the animal bed are eliminated. This concept would be useful for image-guided robotic needle interventions in small animals. Matinfar *et al.* [27] developed a system where the animal is positioned using a rotary table attached to a (x, y, z) commercial platform. In this design, the X-ray gantry is manipulated about a fixed point in the animal using a custom made 2 degree of rotation pinned structure. One degree of rotation about the isocentre is used for imaging and two degrees of rotation were used for therapy. By measuring the focal point of the X-ray tube for each gantry position and calculating positioning correction factors, the authors were able to position the animal to the focal point with a positioning accuracy of ~ 0.2 mm.

The use of micro-CT for image guidance during interventions is also limited. Nicolau *et al.* [28] developed a mechatronic system using a commercial robotic manipulator and a stereoscopic system to complete interventions using micro-CT guidance. The overall targeting accuracy of the system was never quantified; but, the accuracy of tracking the needle tip was 0.7 mm. The system was also never demonstrated to complete an intervention. Waspe *et al.* [29]

developed a custom 6 degree of freedom (DOF) mechatronic system for use with micro-CT to complete interventions. The device had a needle positioning error of $154 \pm 113 \mu\text{m}$ using micro-CT guidance in tissue mimicking phantoms. The system was demonstrated by inserting $200 \mu\text{m}$ beads into rat brains. A second-generation device was developed by Bax *et al.* [30] to improve the accuracy and clinical workflow of micro-CT guided needle placement while reducing the positioning variability and reducing the size of the device to enable it to be used with a 25 cm diameter micro-CT bore. They achieved targeting error of $149 \pm 41 \mu\text{m}$ (quantified in tissue mimicking experiments) and performed a pilot *in vivo* experiment in a xenograft mouse model in which projection views obtained from sequential CT scans were used for visual confirmation of contact between the needle tip and a target bead surgically implanted within the specimen. Beyond the experimental development of these systems, the routine use of micro-CT to complete interventions in small animals is not evident within literature.

Compared to those utilizing ultrasound and CT, there have been relatively few devices developed for small-animal image-guided procedures using MRI. It is speculated that this is due to the amount of technical challenges associated with developing such a system. However, using MRI for guidance is becoming more popular due to its high tissue contrast, multiplanar capability, and ability to provide spectral information. There are no dedicated systems for preclinical MRI-guided robotic needle interventions. However, a dedicated MRI-guided system created by Waspe *et al.* [31] does exist for delivering focused ultrasound to small animals. MRI-guided high-intensity focused ultrasound (HIFU) is a rapidly growing technology that is showing enormous potential to treat a wide range of conditions. As a noninvasive technique for tissue ablation, HIFU has many advantages over traditional surgery without the repeated sessions and ionizing radiation needed for radiotherapy. The system developed consists of a three-axis positioning system for positioning the ultrasound transducer and a custom RF receive coil for high-resolution imaging in the vicinity of the target tissue. The positioning system is MR-compatible, actuated by piezoelectric ultrasonic actuators, and encoded using nonmagnetic linear optical encoders. The device fits inside the bore of a clinical MR scanner and the procedure is performed in the scanner with imaging simultaneously. This concept is useful for MR-guided needle interventions. Ultrasound to MRI registration is performed through the sonication of a phantom that is temperature-sensitive. The device was tested by performing sonications on the brains of five mice. To evaluate the accuracy

of the procedure, the distance between two sonications was measured. The desired separation between sonications was 4 mm and the measured separation was 3.8 ± 0.4 mm.

MR-guided devices are typically designed for the clinical setting, and small-animal models may only be used for validation. Hempel *et al.* [32] developed an MR-guided surgical robot for radiological interventions. The positioning accuracy was reported to be ~ 1 mm when tested in tissue-mimicking phantoms; however, no preclinical experiments were performed. Huang *et al.* [13] developed a device that uses combined MR and PET images for guidance in small animal biopsies. The device was found to have a positioning error of 1.20 ± 0.39 mm in a tissue mimicking phantom and the authors concluded the current system was not suitable for animal interventions. Robotic devices using MR-guidance are not in routine use for small-animal needle interventions.

To resolve the issue of lack of accessibility in a closed bore scanner, a number of multi-modality designs have been proposed where imaging and the intervention are performed in separate workspaces. These systems require the animal to be scanned in a fixture that is later reattached to the robot. These designs utilize industrial robots [13], [28], a built up system composed of commercially available linear and rotary stages [33], or special purpose machines [34]–[38].

Of particular interest are the special purpose machines that were designed according to the specifications outlined by Taylor *et al.* [39] where the tasks of needle placement, orientation and, insertion are mechanically decoupled using a remote centre of motion (RCM). By decoupling the motion of the needle about the RCM, it is no longer necessary to control multiple DOFs to control the needle insertion, which is the most delicate part of the procedure. By aligning the needle axis to the RCM of the machine, the needle can be pivoted about a fixed point and inserted through a predetermined entry point without the need to adjust the XYZ placement of the machine.

Waspe *et al.* [37] developed a 6 DOF robotic needle positioning system consisting of two parallel four-bar linkages. With the needle placed at the RCM, the needle tip remains stationary while the needle orientation is adjusted. The RCM allows the needle tip to be placed at the skin surface and its orientation adjusted without puncturing the animal's skin. The robot is registered to the micro-CT by using the robot to position a needle at five different positions in ultrasound

standoff pad. The needle is retracted from the pad while injecting barium. The pad and barium filled needle tracks are imaged using the micro-CT scanner. The barium tracks are segmented slice-by-slice in the images. The barium track centroids are registered to the known robot trajectory using a rigid-body and iterative closest point registration. The accuracy of the robotic system is next determined through targeting experiments in a tissue mimicking phantom. The phantom consists of gelatin which contains a grid of 250 μm air tubes that intersect to form targets. The phantom was imaged using micro-CT and the air tube intersections localized. The robotic system was used to position a needle at a total of 70 targets in 14 phantoms. Once in position, the needle was withdrawn while again injecting barium into the needle track. The phantom was re-imaged using micro-CT and the targeting error ($154 \pm 113 \mu\text{m}$) of the system determined by measuring the distance from the air tube intersection to the segmented barium track.

The device developed by Ramrath *et al.* [36] uses an arc based design commonly used in neurosurgery to create an RCM. Two degrees of rotational motion are created by mounting the needle driver on a ring which is connected by a pivot at one end to the base of the machine. However, since the tool tip (electrode) does not align to the theoretical pivot point of the machine, 4 different offset parameters were used to account for both the needle misalignment and deflection of the robot. The parameters used correspond to the x-y position of the needle as seen from 2 orthogonal directions. Since the system was designed to implant an electrode into an animal brain, the issue of tool deflection was not considered here as the geometry of the tool tip was symmetrical about its long (insertion) axis. In addition, the potential issue of target movement during the insertion of the electrode is also addressed. They proposed to vibrate the needle at a high frequency along the insertion axis as a potential compensation strategy. To measure the system performance, the following two scenarios were analyzed using stereoscopic camera images of the device supporting an electrode: repeatability which is defined as the ability of the robot to return to the same point in space (mean: 0.011mm), and the ability of the device to position the tool tip at a fixed point in space regardless of the orientation (mean: 0.032mm, maximum 0.11mm).

A device by Bebek *et al.* [34], [35] supports the needle by means of a pair of spherical couplings connected to parallelogram linkages. The RCM of each spherical coupling and attached needle is permitted to telescope between the front and rear parallelogram linkages giving the needle 4 degrees of freedom (2 degrees of rotation about each RCM). They calibrated the device using an

optical tracking system with a root mean square error of 0.25 mm. After calibration of the device, they tested its accuracy by using the robot to draw a line on a piece of paper [40]. They compared the length of the line on the paper to what it should be based on the robot kinematics, and found the average error to be 2 mm, with no stated standard deviation. Later methods to quantify the positioning error of the device by Bebek *et al.* include using optical trackers mounted on the end-effector to determine the actual position of the needle tip and compare it to the position given by the encoders; a root-mean-squared needle positioning accuracy of $419 \pm 166 \mu\text{m}$ was found [35].

Table 2: Summary of current preclinical robots. (Adapted from [41]).

Authors (et al.)	Mechanical design	Degrees of Freedom	RCM ?	Imaging Modality	Application	Mean Free-Space Positioning Accuracy (μm)	Image-Guidance Positioning Accuracy (μm)	Ref
Matinfar (2008)	Custom stage	3 Translational 1 Rotational	No	CT	Radiotherapy	N/A	< 200	[27]
Nicolau (2007)	Industrial articulated arm robot	6 Rotational	No	CT	Needle placement	N/A	N/A	[28]
Waspe (2007)	Custom parallel four-bar linkage	4 Translational 2 Rotational	Yes	CT/ Ultrasound	Needle placement	54 ± 12 (Pitch axis plane) 91 ± 21 (Roll axis plane)	154 ± 114 (CT) 550 ± 112 (Ultrasound)	[37]
Bax (2013)	Custom spherical linkage	4 Translational 2 Rotational	Yes	CT	Needle placement	71 (Pitch axis plane) 75 (Roll axis plane)	149 ± 41	[30], [42]
Hempel (2003)	C-bow and swivel arm	3 Translational 3 Rotational	No	MRI/CT	Radiotherapy	N/A	~ 1000	[32]
Waspe (2010)	Custom stage	3 Translational	No	MRI	Focused Ultrasound	N/A	3800 ± 400	[31]
Huang (2006)	Commercial desktop robot	4 Translational 1 Rotational	No	MRI-PET	Needle placement (biopsies)	50 ± 12	1200 ± 390	[13]
Ramrath (2008)	Custom stereotactic frame/ goniometric arc	3 Translational 2 Rotational	Yes	N/A	Arbitrary probe placement	32 ± 11	N/A	[36]
Bebek (2013)	Custom parallel gimbal joints	5 Rotational	No	N/A	Needle placement (biopsies)	419 ± 166	N/A	[35]

1.4 Registration

Registration is the process by which the correspondence between two imaging workspaces is determined (**Figure 1**). It is a highly researched topic in the field of medical imaging, as well as image-guided interventions, due to its widespread utility. Registration may be used to enable physicians to accurately compare longitudinal medical images of a patient undergoing treatment for a particular disease, technicians to calibrate the coordinate systems of two scanners to enable

dual-imaging capability, and engineers to correlate the position of robot-mounted surgical tools to an imaging modality for computer-aided medical interventions.

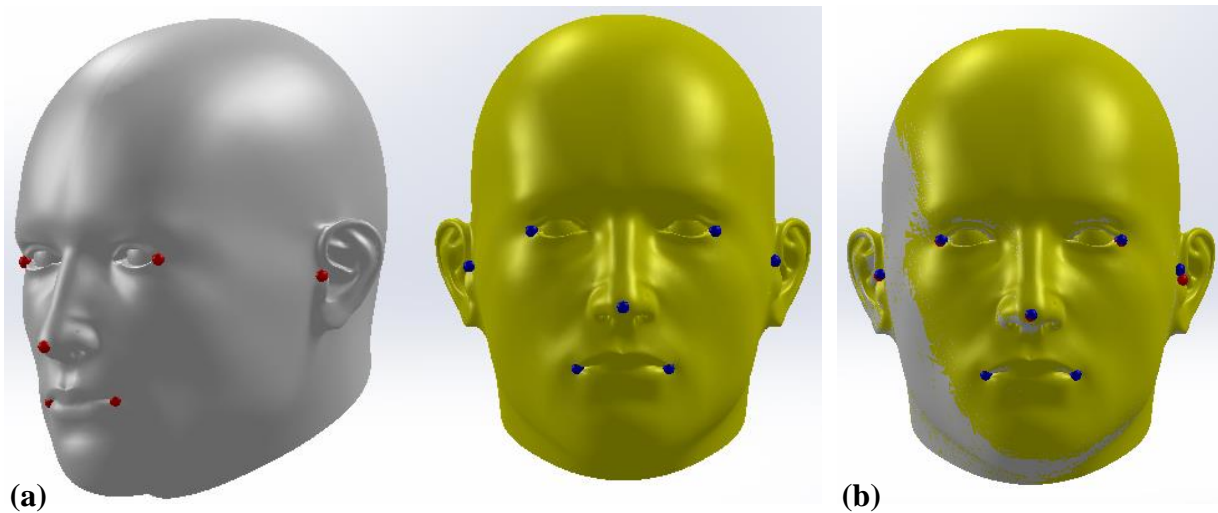


Figure 1: (a) Two 3D volumes differ in translation and rotation. Selecting fiducial landmarks using easily detected features (red and blue dots), it is possible to perform a rigid registration for alignment (b).

Landmark-based rigid registration is the simplest form of registration commonly used to integrate a robotic device with an isotropic imaging modality. Rigid registration assumes only six degrees of freedom which include three translational XYZ components and 3 rotations. Landmark-based rigid registration involves collecting a point-set of fiducials that are common to both image volumes, or workspaces, being registered. A fiducial is a point of reference that can be easily and repeatedly localized with minimal operator variance. Using these common point-sets, the rotational and translational components of a transformation can be calculated using a least-squares fitting technique [43].

Previously in our lab, Waspe *et al.* developed a technique to register high-frequency ultrasound to a first-generation robotic device intended for small-animal injections [29]. It involved designing a registration phantom containing a prescribed pattern of 12 fiducial beads that attached onto the end of the intervention needle (**Figure 2**). This assembly was then scanned to acquire a 20 μm voxel 3D image under micro-CT requiring several hours to yield an image depicting the fiducials as well as the needle tip. The needle was then detached from the phantom and attached to the robot for RCM calibration, in which a CCD camera was used to precisely

position the needle tip at a point within the device’s kinematics at which it is fixed in space regardless of its orientation. The phantom was then reattached to the robot-mounted needle and the device’s stages were used to move the needle tip to seven fiducial positions within the field of view of the 3D ultrasound image acquired by a Vevo 770 transducer, an earlier generation of VisualSonics micro-ultrasound system. This procedure was cumbersome: in addition to moving the robotic stage several times, a 3D ultrasound image had to be acquired for every robot pose and, for each of the seven poses, 12 beads had to be manually localized in ultrasound coordinates for a total of 96 bead localizations (12 in micro-CT, 84 in ultrasound) for a single intervention. Furthermore, this procedure prevented the use of different needles for one experiment, making a series of experiments with multiple mice impractical.

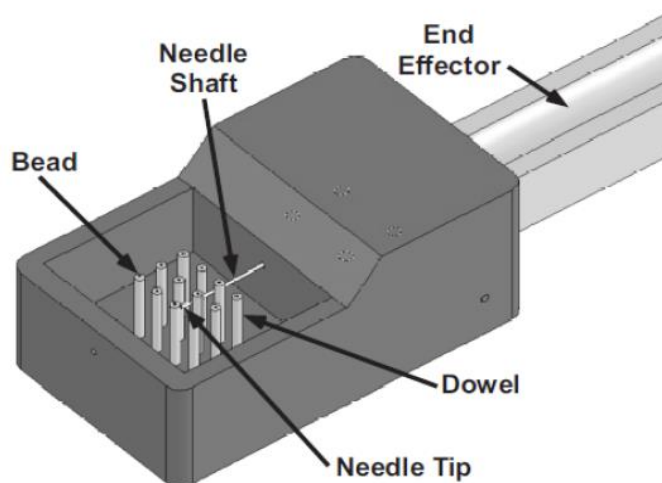


Figure 2: Ultrasound registration phantom by Waspe *et al.* [29]. Phantom was scanned in micro-CT pre-operatively to determine the spatial relationship between the needle tip and fiducial beads.

Bax *et al.* developed the second-generation device and validated its accuracy under micro-CT guidance [30]. For their registration procedure, a single borosilicate 6 mm bead was placed at the RCM of the robot; the XYZ stages then moved the robot to four fiducial positions within the bore of the micro-CT scanner that were used to calculate a one-step rigid registration between the micro-CT scanner and the mechatronic system. Since the scanner was not dedicated to robotic interventions, which is usually the case, additional fiducial beads were placed at the base of the device so that any error resulting from the removal and reattachment of the robot onto the scanner could be accounted for.

Although other types exist, point-based rigid-body registration techniques are most prevalent in preclinical robotics. Waspe *et al.* used points of ablation in a tissue mimicking phantom to register their high-intensity focused ultrasound device to MR for guidance [31]. A variety of plastics and contrast-filled phantoms have also been used to create easily identifiable fiducial markers in MRI [13], [44]. While six degree-of-freedom rigid registrations are routinely used, affine registrations also exist that assume 12 degrees of freedom: 3 translation, 3 rotation, 3 scaling, and 3 shearing components. Scaling would most likely be considered in an image-guided intervention where the guidance procedure relies on preoperative scans using a modality other than that used for guidance, especially in the case of voxel anisotropy. While most bore-scanners typically do not have this issue, shearing may be a factor in ultrasound if the 3D volume is acquired by stepping a linear array on a motor. In this case, shearing could arise if the device is handheld, or the assembly for attaching the transducer onto the motor is not robust.

The three error metrics commonly looked at to determine the accuracy of point-based rigid registration are: fiducial localization error (FLE), fiducial registration error (FRE), and target registration error (TRE). FLE gives an idea of the variability of an operator when selecting, or localizing, fiducial markers for a registration. It is defined as the root mean squared (RMS) distance between the localized points in a set from their true (unknown) positions [45]. It is worth comparing to the registration error metrics, FRE and TRE, since it may indicate how much of their errors are attributed to the inconsistency of the operator during fiducial localization. FRE is a registration error metric that is defined as the RMS distance between the landmarks in a ‘fixed’ image/workspace and the transformed landmark positions from a ‘moving’ image/workspace. These landmarks used to calculate a registration will here on be referred to as *fiducials*. Similarly, TRE is also the RMS distance between the landmarks in a ‘fixed’ image and the transformed landmark positions from a ‘moving’ image; however, these landmarks are specifically not used to calculate the transformation and will be referred to as *targets*.

In image-guided interventions, FRE has incorrectly been used in the past as the metric that represents whether a procedure would be accurate or not [46]. FRE merely informs the operator how well the fiducials used to calculate the registration line up afterwards, while TRE reveals how well the registration will serve for actual targets not used in the registration calculation. Furthermore, while it may seem intuitive that a large FRE result will lead to a large TRE, this is

not necessarily the case. For a normal distribution of FLE across all fiducials, it was found by Fitzpatrick *et al.* that FRE and TRE are uncorrelated [46]. Furthermore, fiducial placement, as well as the number of fiducials used, plays an indirect role in the resulting TRE. TRE can be minimized by 1) maximizing the number of fiducials used and 2) arranging the fiducials in a widespread, non-collinear pattern such that the centroid of the arrangement is located at the intended target position[47].

1.5 Image Artifacts in Ultrasound

Ultrasound may serve as a useful guidance tool for minimally invasive procedures such as injections and laparoscopic surgeries; however, it is beset by a variety of artifacts introduced by the intervention tools themselves. For the purpose of this thesis, it is important to understand the different types of ultrasound artifacts not only found when analysing images depicting the internal anatomy of small animals, but also when localizing metal needles (for registration) and plastic phantoms (for targeting experiments) and so forth. In this section, we will discuss the different types of artifacts as well as some techniques used to minimize their effect on procedure accuracy.

Ultrasound imaging relies on the reflection of the transmitted beam from a surface. While rough surfaces cause the beam to be scattered, smooth surfaces, such as metal or plastic interventional tools, act like a mirror [48] and reflect the beam in a straight line. This interferes with the scanner's receive signal processing since echoes from interventional tools do not match the spherical wavefronts expected for scattering from soft tissue. Metal needles act as smooth reflectors and seem to reflect at an angle approximately equal to the angle of incidence [49]. Orienting a needle such that it is parallel to the transducer face is ideal for the reduction of artifacts (**Figure 3**); the ability to localize the needle degrades as the reflection angle is increased due to the presence of heavier artifacts. In the case where neither the needle nor transducer can be adjusted such that they are parallel to each other, it is possible to redirect the ultrasound beams. This is known as beam steering, and can be done by electronically altering the timing of excitation of the piezoelectric elements [48]. "Echogenic" needles may also be used to overcome this insertion-angle issue using either an echogenic coating on the exterior of the needle, or small grooves to create mimicking mini-reflectors (**Figure 3 (d)**) directing ultrasound back to the transducer. Another custom-design approach involves placing a piezoelectric sensor at the needle tip location.

Once activated by the ultrasound beam, it emits an electrical signal detected by the machine [48]. This technique would not be suitable for preclinical applications due to the small needle gauges commonly used.

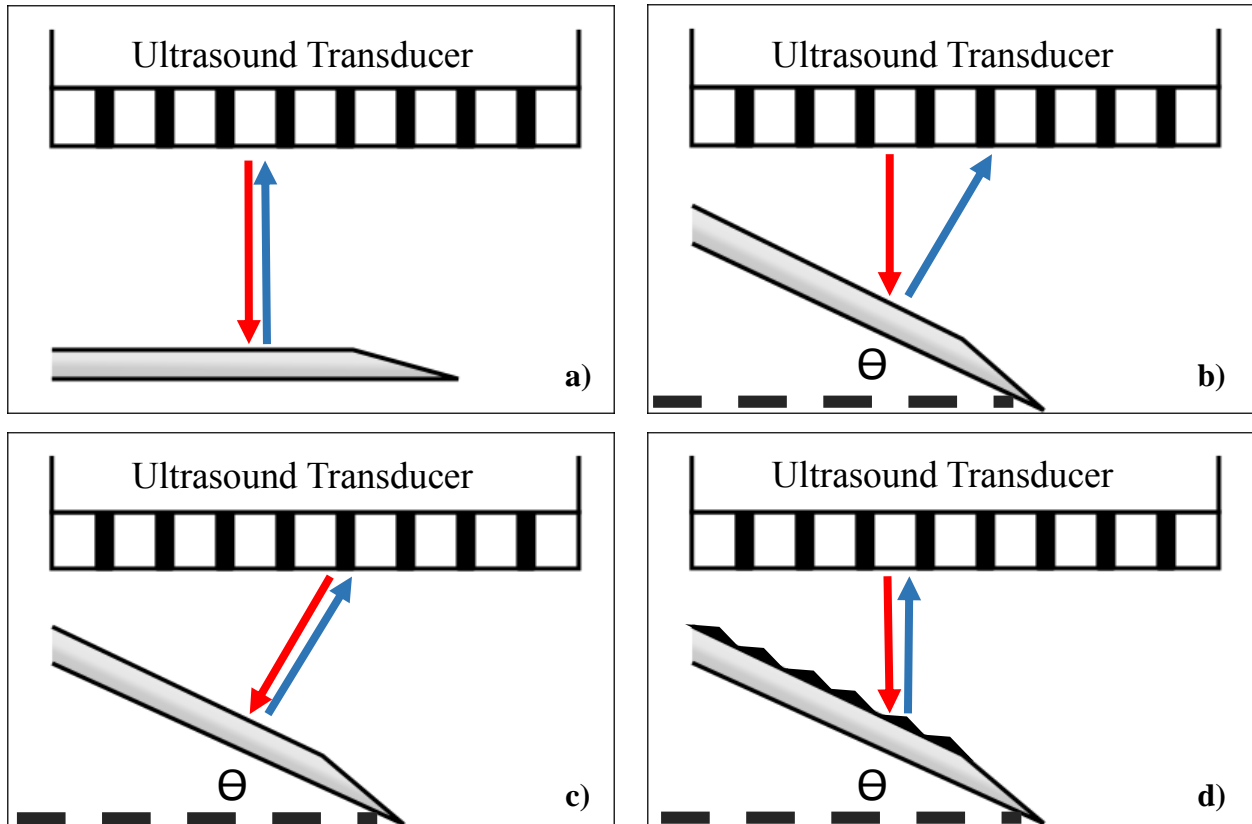


Figure 3: (a) Orienting a needle parallel to the ultrasound transducer provides for optimum visualization. (b) However, accurate visualization becomes more difficult as the angle of incidence increases. (c) Beam steering can be used to compensate for this angular offset. (d) There has also been promising progress in the development of ‘echogenic’ needles. In the case depicted above, small grooves act as miniature reflectors overcoming the needle insertion angle to reflect the ultrasound back to the transducer (Adapted from Reusz *et al.* [48]).

A ring-down artifact (**Figure 4**) is commonly seen when imaging using a coupling gel rather than water. Sound waves trapped within an air bubble being imaged create reverberant vibrations which, when transmitted back to the transducer face, leads to region below the bubbles which have a higher than expected signal [50].

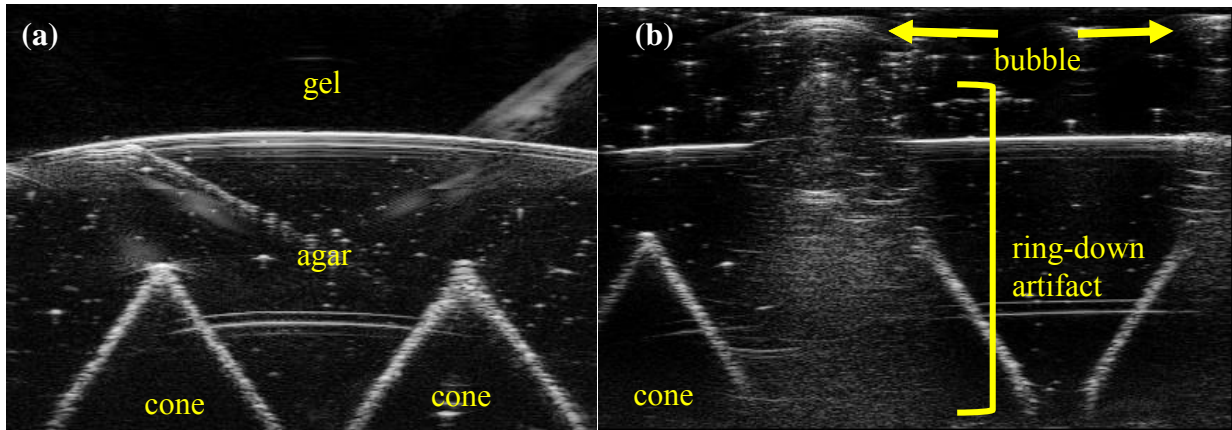


Figure 4: (a) Tissue mimicking phantom containing two plastic cones. (b) The occurrence of an air bubble near the transducer face results in a ring-down artifact, hiding underlying features.

Acoustic shadowing is another important artifact that describes the reduction in the echo strength of the signals arising behind a strong reflector or attenuating structure. Examples of these structures commonly seen in clinical practice include calcified tissues, bone, or gas. When an ultrasound beam is incident upon an object that is a strong reflector, such as the ribs or steel needle (acoustic impedance of 7.8 and 45.7 MRayl, respectively [48]), very little of the sound energy will be transmitted distal to the object. This will cast a very strong anechoic shadow yielding a signal intensity within this shadow that is very close to zero (**Figure 5**).

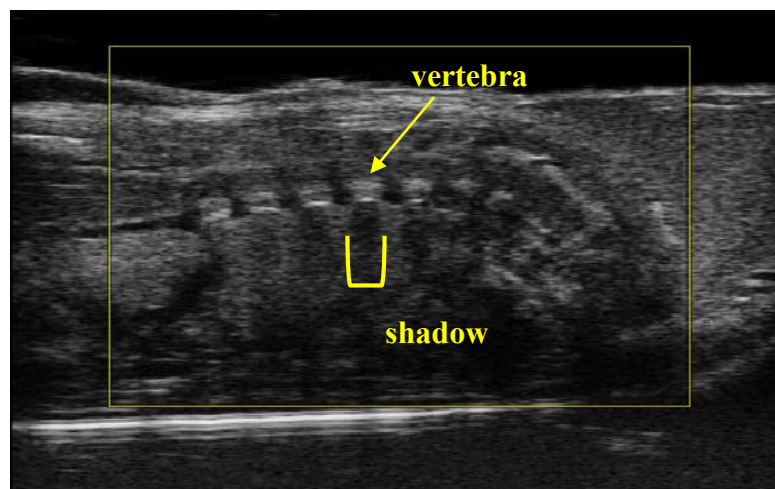


Figure 5: Chicken embryo vertebrae imaged in ultrasound using a VisualSonics MS-250 transducer. Acoustic shadowing appears distal to each vertebra.

In practice, however, artifacts below the needle are dominated by reverberations rather than shadowing; this will be discussed shortly. These artifacts make localizing the needle difficult and are detrimental to ultrasound-guided injection procedures where the needle must be kept in-plane and slightly above a region of interest. Reverberation is an intuitive phenomenon that is associated with sound and that involves the bouncing back-and-forth around a central object. It is analogous to multiple reflections in optics. In the case of ultrasound, repetitive reflections of waves occur between two or more highly reflective layers resulting in equally spaced hyperechoic signal that become diminishingly less in amplitude distal from the object of interest. In short, it is a reflection phenomenon, but can conceivably be used as a useful tool in ultrasound, such as in the identification of bullets in a gunshot victim or radioactive pellets in a patient undergoing brachytherapy treatment for prostate cancer. Ultrasound waves emanated from a transducer face in the form of pulses towards a highly-reflective interface will be reflected back towards the transducer. This reflective echo provides the information to form the image of the object at its correct distance from the face based on its propagation time. The transducer face in turn suffers another reflection [51]; therefore, you have a second round trip of the ultrasound wave at a smaller amplitude that travels to the object of interest and is reflected back to the transducer again. This is repeated until the amplitude of the signal is diminished. Each round trip the wave results in an equally spaced reverberation artifact (**Figure 6**).

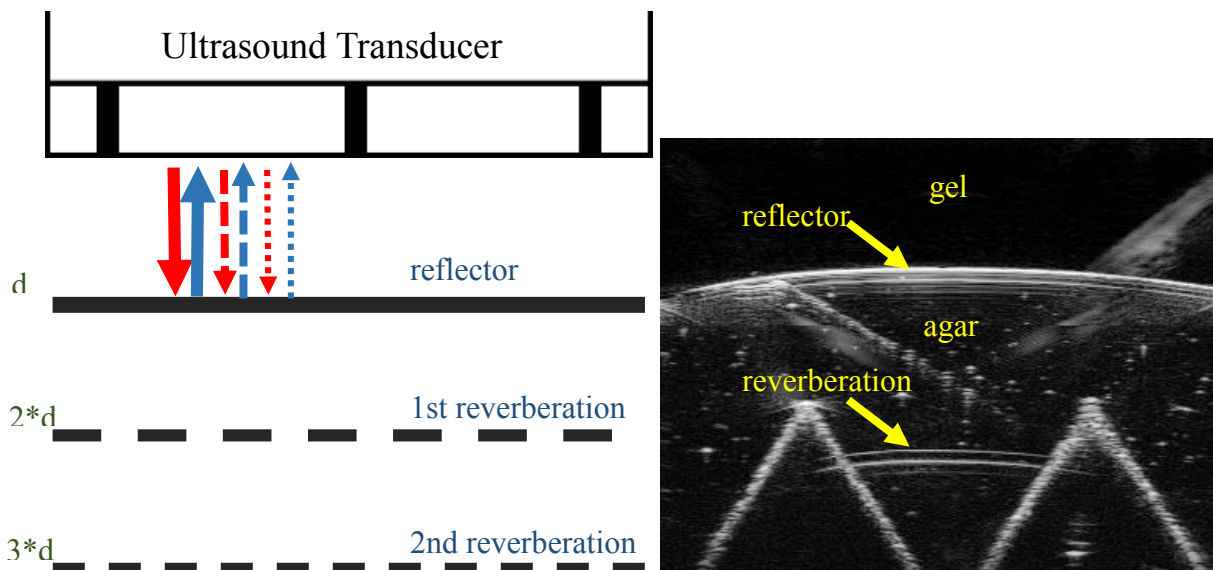


Figure 6: (a) Graphic depicting physical theory behind reverberations. Back-and-forth reflections between a highly reflective surface and the transducer face causes equally-spaced reverberation

artifacts that diminish in amplitude with each occurrence. **(b)** The surface of a tissue-mimicking phantom causes a reverberation artifact beneath.

In the case of metal needles, the back-and-forth reflections of the ultrasound waves between the interior and anterior walls of the needle are the cause of the proximate reverberation artifacts seen as in **Figure 7** [48]. Comparable to reverberations, we can see in **Figure 8** what is called a comet tail artifact. Both reverberations and comet tails are based on the same physical mechanism; however, a comet tail is the common term used to describe such effects caused by a small object, such as a fiducial bead or needle cross-section.

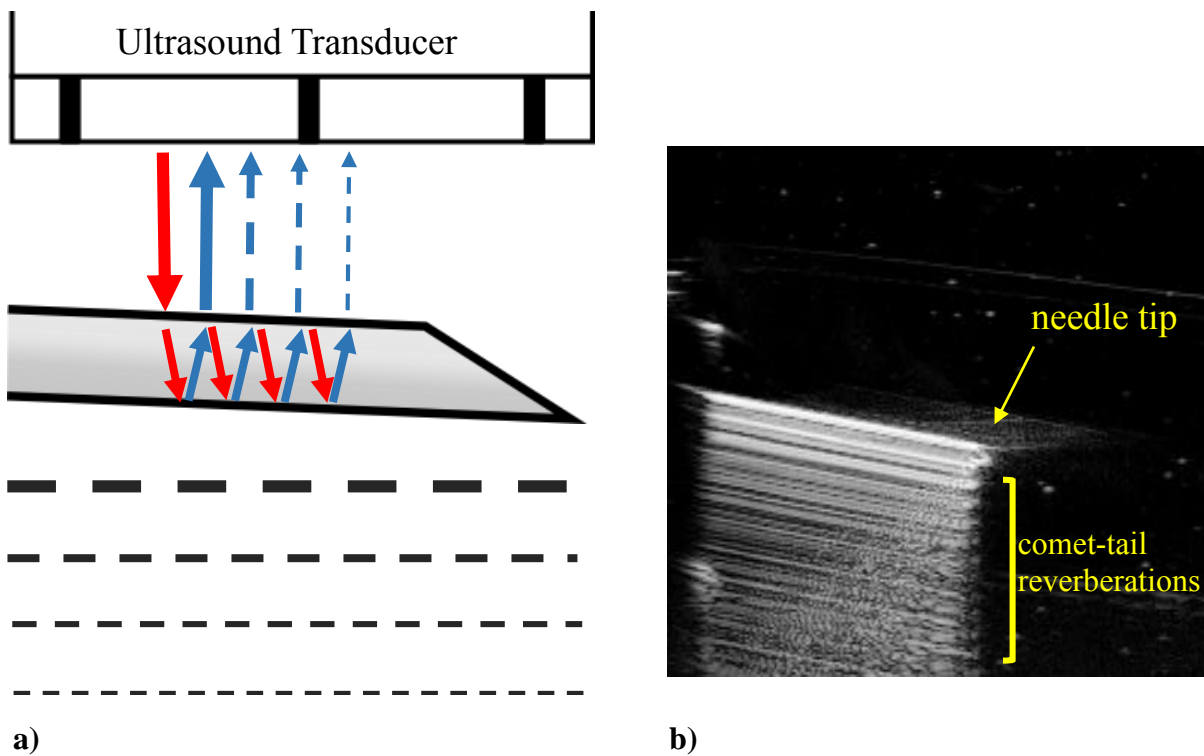


Figure 7: **(a)** Graphic depicting physical theory behind needle reverberations. Subsequent reflections between the interior and exterior walls of the needle result in echoed signal that diminishes with each round trip. **(b)** Micro-ultrasound image of 30 gauge conical needle imaged near-parallel to the transducer. (Adapted from Reusz *et al.* [48]).

Side lobes describe sound energy reflections that are generated at improper off-axis locations alongside the main beam (**Figure 8 (a)**). They are added to, or assigned as, part of the main beam and occur in both single and array transducers. Side lobes appear as hyperechoic densities within a hypoechoic/anechoic background. As the depth of the object increases, the extent of the side-lobe artifact increases due to the effect of side lobes from multiple scan lines

overlapping. In **Figure 8 (b)**, a needle cross-section is imaged within an agar phantom, resulting in prominent side-lobe artifacts. These side lobes would not be so obvious in a background of scattering from tissue; however, they would reduce the contrast of features lateral to the needle.

One of the basic assumptions of an ultrasound scanner is that the velocity of sound through all soft tissues is 1540 m/s. However, if the beam passes through a structure consisting mainly of fat, the actual velocity of 1450 m/s causes the object to appear further away from the transducer face. On the other hand, if the reflector of interest has a velocity higher than 1540 m/s, it will appear closer to the face than its true position. This can cause a discontinuous representation of an interventional tool when being guided by ultrasound imaging through inhomogeneous tissue, making *in vivo* needle-guidance procedures confusing to the unprepared operator. The smaller the object the larger the increase in velocity necessary for this to take effect [52].

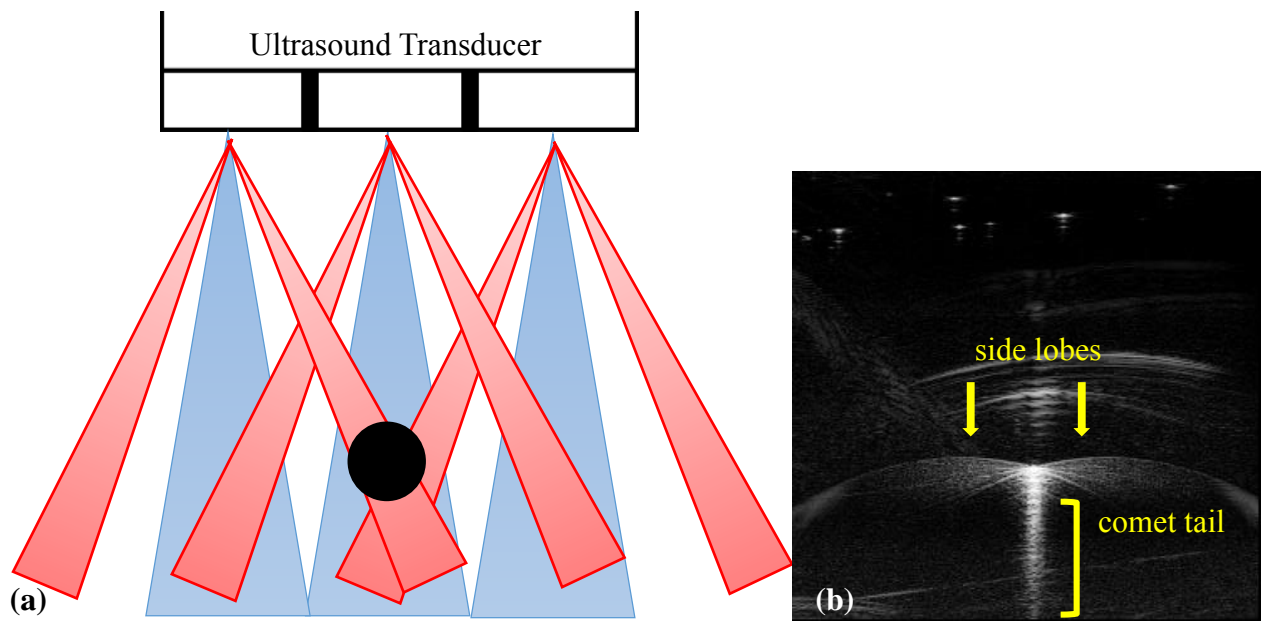


Figure 8: Cross-sectional view of needle imaged using high-frequency ultrasound. (a) Illustrates how the needle can still be detected by transducer subapertures it is not directly distal to via side lobes (red) even though it is missed by their main lobe (blue). This leads to the side lobe artifacts shown in (b). (Adapted from Reusz *et al.* [48]).

1.6 Dendritic-Cell Cancer Vaccine Immunotherapy Research

There are many potential applications to preclinical image-guided robotic systems which favour the high accuracy and precision of said devices over the moderate accuracy and relatively large variability of human operators performing the small-scale intervention manually. One such application focused on in this thesis is the injection of dendritic-cell (DC) cancer vaccines into the lymph nodes of mouse cancer models to determine the efficacy of this minimally-invasive approach.

Surveillance cells exist in the immune systems of our bodies whose main function are to recognize foreign microorganisms, such as viruses and bacteria; process the information presented by their antigens, and relay the obtained information by migrating back from tissues in contact with the external environment (i.e., skin and the inner lining of the stomach, nose, and lungs) to lymph nodes packed with white blood cells (WBCs) and other immune cells. Therefore, the surveillance cells act as messenger cells with the purpose of activating a group of WBCs, known as lymphocytes, which are involved in forming adaptive immune responses. T-cells, a type of lymphocyte, govern cell mediated immune responses. Once they are activated by DCs, the T-cells take on a search-and-destroy role [53].

In the case of cancer, DCs are unable to identify the malignant cells as foreign. This is due to the secretion of immunosuppressant molecules by the tumour itself [53]. The theory behind cancer-immunotherapy is that DCs can be isolated from the blood sample of an infected patient in a laboratory; similarly, the distinct antigens presented by the cancer cells may also be isolated from the tumour sample. Through similar techniques, the DCs may be loaded with the tumour antigens and left to mature. The hypothesis behind these treatments is that, after re-injection, the loaded DCs are expected to stimulate an immune response against the tumour [54].

One question this process poses is where the mature DCs should be injected. Some practices have been: intravenously (into a vein), and subcutaneously (into the layer of skin directly below the dermis and epidermis). Previous studies have shown that when using either of these two methods, few of the DCs actually make it to the lymph nodes of the body. This means that few

lymphocytes are activated and begin an immune response [53], [55], [56]. One way of working around this problem is to inject the loaded DCs into the lymph nodes themselves, in which case, a high percentage of the DCs would make it into the lymph node to potentially activate an immune response. However, previous studies using this method have yielded mixed results [57]. It is believed to be due to the fact that 1) these injections have been done manually (by hand) and blind (through palpation without image guidance), and that 2) the risks of injecting manually and blind may cause damage to the lymph nodes.

It is speculated that a more careful injection harnessing the accuracy and precision of an ultrasound guided mechanical device to better control the velocity, force, and trajectory of the needle will minimize damage to the lymph nodes, and ultimately increase the effectiveness of the treatment.

1.7 Thesis Objectives

The objectives of this thesis were to (1) redesign certain mechanical features of our existing micro-CT guided injection robot to adapt it for high-frequency ultrasound guidance, specifically for the injection of dendritic-cell cancer vaccines into the lymph nodes of small-animal cancer models. A targeting accuracy requirement of $< 500 \mu\text{m}$ meant that the inherent error from calibration, robot-ultrasound registration, and other various maneuvers necessary to maintain the workflow of such a procedure must be sufficiently low as well. (2) Determine the fiducial and target registration errors of the proposed registration technique in tissue-mimicking phantoms. Finally, (3) demonstrate that the targeting accuracy of the robot for ultrasound-guided injections into tissue-mimicking phantoms exceeds the $500 \mu\text{m}$ design goal and demonstrate that the robot produces smaller targeting errors than a commercial manually operated injection device.

1.8 Thesis Outline

Chapter 2

Chapter 2 describes the mechanical adaptation of a micro-CT guided robot for ultrasound guidance. Other design changes involved the consideration of the end-user immunology application of intranodal injections in live mice. Integration of the robot to the commercially

available VisualSonics Inc. interventional platform/railing system was justified by determining the inherent error caused by moving components along the railing. Two registration techniques were designed to link the coordinate system of the robotic device to the image volume acquired by the ultrasound transducer. The one-step method was preferred over the two-step registration technique due to the considerably lower execution time while yielding comparable error metric results.

Chapter 3

Chapter 3 covers the numerous validation techniques investigated to determine the ultrasound-guided needle-positioning robot's accuracy in tissue-mimicking phantoms. These range from the use of contrast agents to depositing physical markers for micro-CT validation. The technique chosen involved localization of a needle-track tip within an agar phantom using micro-ultrasound as the visualization modality. This needle track was used to estimate the targeting accuracy of the robotic and manual injections in order for a comparison. Injections were performed in live mice using both the robot and competing VisualSonics micro-manipulator to demonstrate the feasibility of minimally invasive intranodal injections in mice under ultrasound guidance.

Chapter 4

Chapter 4 includes a summary of the main thesis topics. The Future Work section discusses some recommended modifications to the system to address some of the weaknesses of the robotic system: platform rigidity, tissue deformation, and a lack of real-time image feedback capability. The clinical translation of this work is also discussed.

2 Adaptation of Robot for Ultrasound Guidance

2.1 Mechanical Hardware

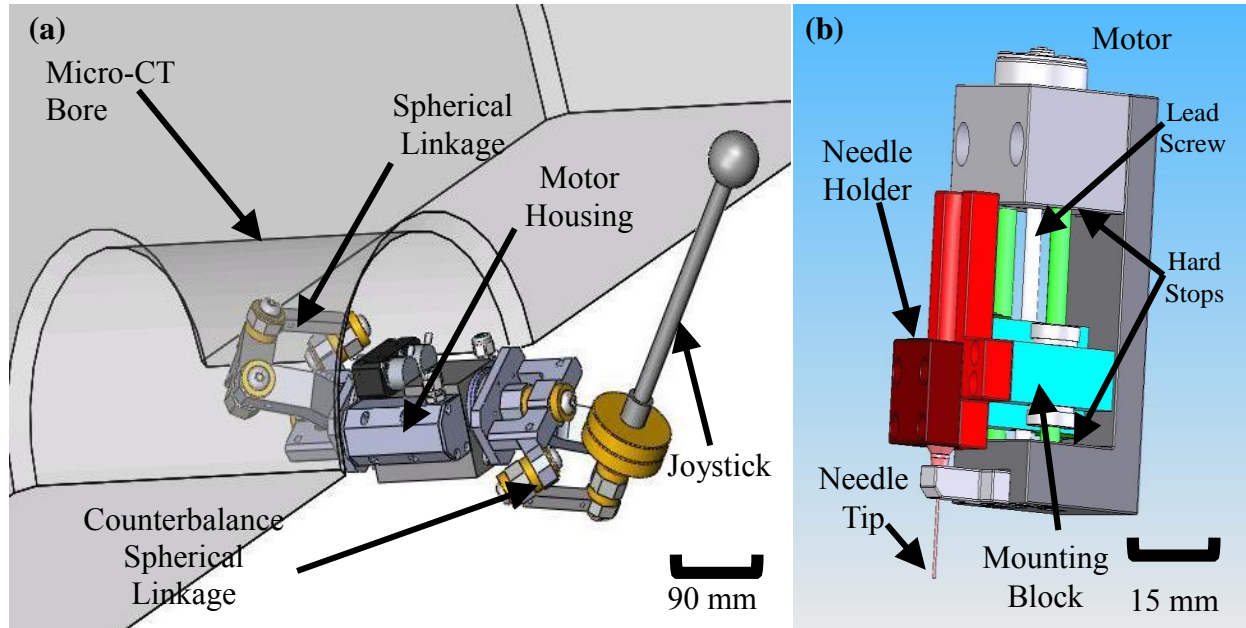


Figure 9: (a) Solidworks model of original 2nd generation image-guided injection robot designed for micro-CT. (b) Solidworks model of original needle driver mechanism. Needle is inserted to RCM position.

Our lab's second-generation image-guided needle-placement robot [41] (**Figure 9**) was designed based upon spherical linkage mechanisms used in a clinical breast-biopsy device developed by Smith *et al.* [58]. The rotational axes of the spherical linkages intersect to form an RCM. They are designed to eliminate the positioning error from deflection of the four-bar mechanism, implemented in our first-generation device [29], while also miniaturizing the device to fit within the bore of a micro-CT scanner [30]. A mirrored spherical linkage counterbalanced the weight of the needle positioning linkage. The total range of the device was set to be $\pm 22.5^\circ$ in the pitch directions and $\pm 90^\circ$ in the roll direction. The needle position could be adjusted manually using a joystick or stepper motors. A motorized 3D micrometer stage was used to adjust the position of the RCM relative to the animal to reach specific targets. The RCM was positioned such that it was at the target location within the animal rather than at the surface of the skin to simplify the needle driver design; this allowed for the RCM positioning of the robot to rely, solely, on the high accuracy of the XYZ motors. The needle driver was designed to place the needle tip at one

of two positions: retracted or inserted to the RCM (~14 mm travel distance). A miniature stepper motor and lead screw were used to drive a needle mounting block to a hard stop equipped with a limit switch. Set screws were used to adjust the position of the hard stop to ensure the needle tip was positioned at the RCM after insertion. Overall, the positioning accuracy of the device was dependent on the accuracy of the motorized stages, calibration of the hard stop, and the ability of the device to maintain a consistent RCM position throughout its full range of motion (~12.5 μ m deviation).

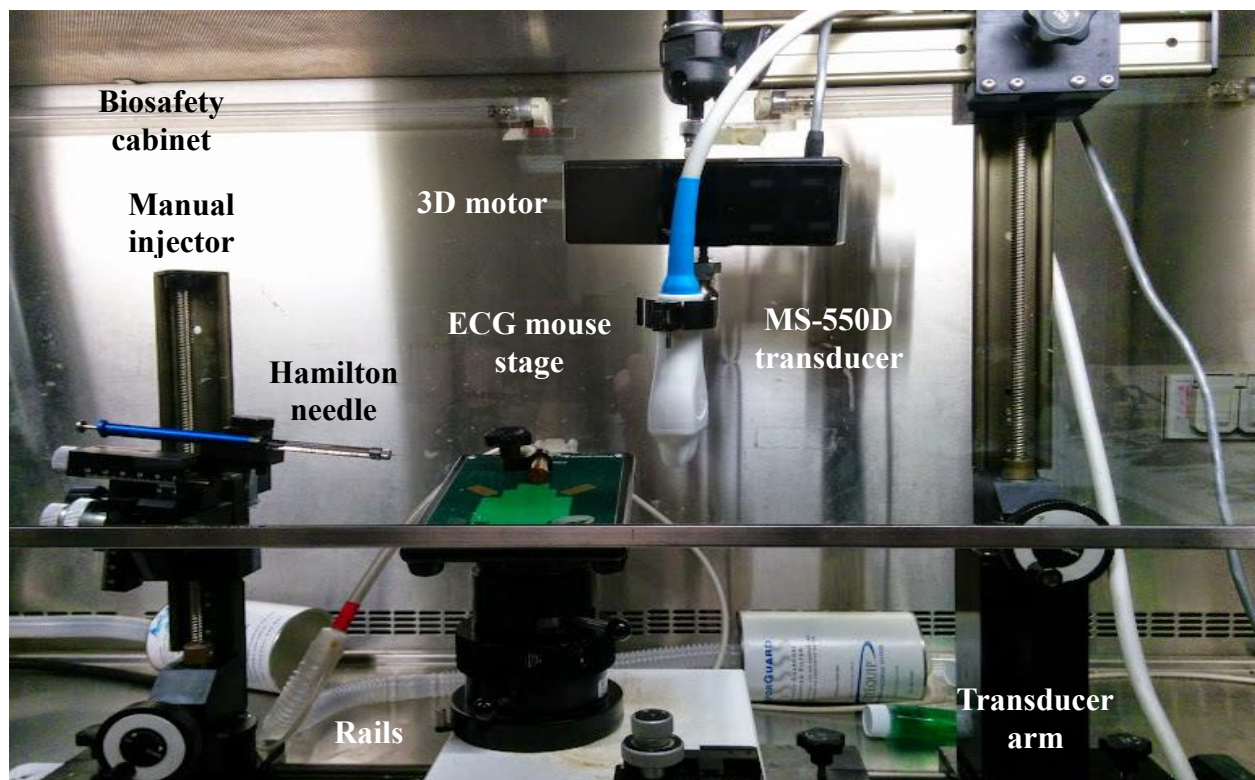


Figure 10: VisualSonics provides a railing system equipped with an adjustable transducer arm and manual needle manipulator. A specialized mouse stage allows for easy anaesthesia and ECG monitoring. The VisualSonics motor allows for 3D image acquisition by stepping the MS-550D transducer at small increments. This transducer is generally used for mouse abdominal, reproduction, tumour, and vascular imaging as well as some similar rat applications.

VisualSonics has developed an integrated railing system for ultrasound imaging and ultrasound-guided interventions (**Figure 10**). The railing system serves as a heavy base on which interchangeable components can be fixed. These components include an adjustable arm on which a transducer can be held, a basic mouse stage, and, in the case of guided injections, a manual injection system which a needle can be fixed to and finely manipulated (4 DOF: 1 insertion, 1

rotation, 2 translation) during an intervention. In place of the VisualSonics micro-manipulator injection system, the ultrasound-guided robot was installed onto the railing system for image-guided interventions. A 3D stepper motor may be installed onto the ultrasound-transducer arm to enable 3D image acquisition. VisualSonics also offers a specialized physiological monitoring system that is fixed to the mouse stage via a magnetic lock. It allows for electrocardiography (ECG), heart rate, and temperature monitoring, and serves as a tool for easy manipulation of the mouse, or rat, using its ball-and-socket joint; an optional clamp also exists as an anaesthetic-hose fixture for imaging animals knocked out using isoflurane gas.

Adapting our mechatronic device to ultrasound relieves us from some of the design constraints previously placed for CT-guidance (**Figure 11**). The robot no longer must fit in a micro-CT bore, and its material choice has no effect on ultrasound imaging. Therefore, minor changes were made to the original device designs in order to maintain the performance accuracy achieved by Bax *et al.* [30]. For example, the robot was fixed onto a base plate which slides on to the VisualSonics rail system. Overriding manual locks were installed to fix the roll and pitch of the robot if necessary, and considerable height (~15 cm) was added to enable the robot to reach the imaging workspace and in order to allow for a $\pm 180^\circ$ range in robot's roll necessary for our registration procedure (discussed later). Significant effort was put into fine-tuning designs, monitoring fabrication, and adapting to manufacturer resources and abilities to recreate the high-precision image-guided device.

A potential end-user application of intranodal injections of a dendritic cell (DC) cancer vaccine into mice has led to necessary redesigns of the robot's needle driver. Previous needle driver designs by Bax *et al.* [30] assumed the use of a cannula and medical tubing would be appropriate for the delivery of substances in most preclinical studies. Our immunology collaborator, Dr. Greg Dekaban, deems this technique inefficient for the delivery of human DCs as only a relatively small volume (10 μL) is needed per intervention, while unacceptable amounts of the vaccine would be lost in tubing as waste. Instead, a low dead-volume Hamilton syringe (25 μL , series 802) was recommended. Not only does its use minimize the DCs wasted, but a single syringe can be used for multiple procedures as the cannula can be replaced. The syringe is 'front-loaded': meaning that a separate 'dummy' syringe is used to fill the Hamilton with the DC solution while its cannula and securing twist cap are temporarily removed. This is convenient for a few

reasons. For the intended application of direct lymph node injections in mice, a small needle gauge of 30G (~ 160 μm interior and 315 μm exterior diameter) must be used. A bevel angle of 12° is the sharpest option available to obtain the best skin-piercing ability and therefore minimize tissue deformation and mouse movement during an injection. Due to the small outer diameter and sharp tip of the custom cannula specifications, a user is likely to destroy DCs due to shearing if a regular solution-withdrawal technique is used to load the Hamilton. Therefore, the dummy syringe used to front-load the temporarily disassembled Hamilton syringe using a much larger needle gauge (e.g. 22 G). The 30G cannula is secured onto the Hamilton syringe using the twist cap after loading is complete.

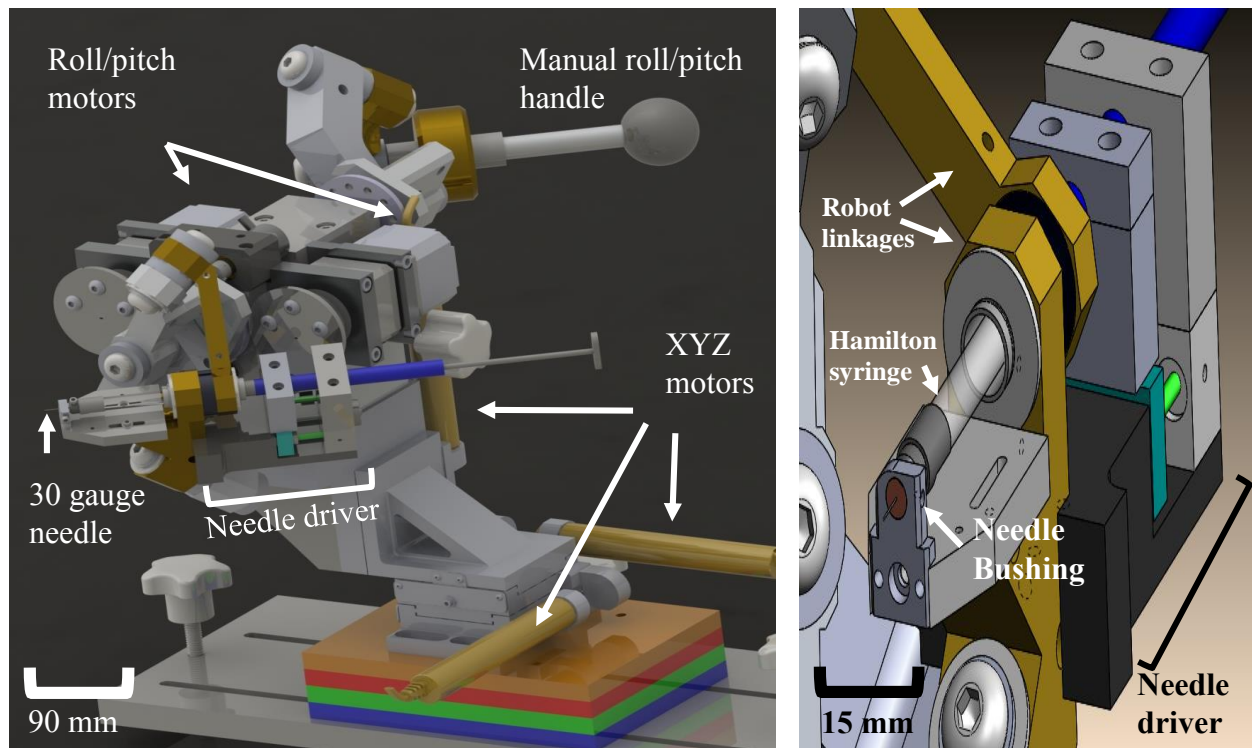


Figure 11: (a) Solidworks model of new ultrasound-guided needle positioning robot. (b) Solidworks model of modified needle driver mechanism mounted external to the robot's spherical linkages. A linkage joint was hollowed to allow the zero dead-space Hamilton syringe to pass through.

The needle driver designed by Bax *et al.* [30] was located at the front end of the spherical linkages, near the RCM point, and was designed to only support a cannula connected to tubing. The zero dead-space Hamilton syringe is much too large (23 cm in length) to fit on to the robot's end-effector region. Instead, one of the steel cylinders connecting two linkages at a joint was

hollowed out to allow room for the Hamilton syringe to pass through. Design specifications from our collaborators did not permit the syringe to be clamped to the robot's driver at the front end since it is made of glass and contains necessary-to-read volumetric markings. Therefore, the entire driver assembly was shifted beyond the linkages in order to firmly clamp the steel base of the syringe. Optical switches were used to control the depth of the injection to the RCM position, while the hard stop technique used by Bax *et al.* was not implemented. This was partly an oversight; however, using the optical switch alone should be enough to repeatedly stop the needle tip at the same RCM position, and it ensures that the non-encoded stepper motor used for syringe driving was not accidentally burned-out by a hard stop before tripping the optical switch during the testing phase.

2.2 Remote Centre of Motion Needle Calibration

2.2.1 Earlier Generation Techniques: Camera Calibrations and Fixture-Based

A needle was calibrated at the RCM point of the micro-CT guided version of the device using one of two methods: a cumbersome camera calibration technique or a fast fixture-based calibration. In the camera based calibration, each rotational axis of the robot was validated separately. A charge-coupled device (CCD) camera equipped with a macro lens was placed orthogonal to the plane of each rotational axis of the robot. Each axis was moved to points along its full length of motion, capturing an image each time of the conical needle tip. The needle position was adjusted accordingly until all images indicated minimal deviation of the needle tip when manipulating its orientation. A 12.5 μm deviation was reported, and the procedure could take over one hour to complete [30]. The fast fixture-based technique involved attaching a flat delrin block onto the robot such that its top surface was at the RCM position (based on precision assembly techniques – through use height and pressure gauges) and advancing a robot-mounted needle until its tip was just barely at the surface of the block as determined by sliding a thin (25.4 μm) steel shim across the calibration block's flat surface until it caught the sharp needle tip. This calibration block technique was validated using the camera calibrations technique and was found to yield an error of 75 μm and 12 μm in the robot's roll and pitch, respectively [41]. For our ultrasound guided robot, a fixture-based RCM calibration approach was used; however, there was one minor alteration.

2.2.2 Electrical-Contact Calibration

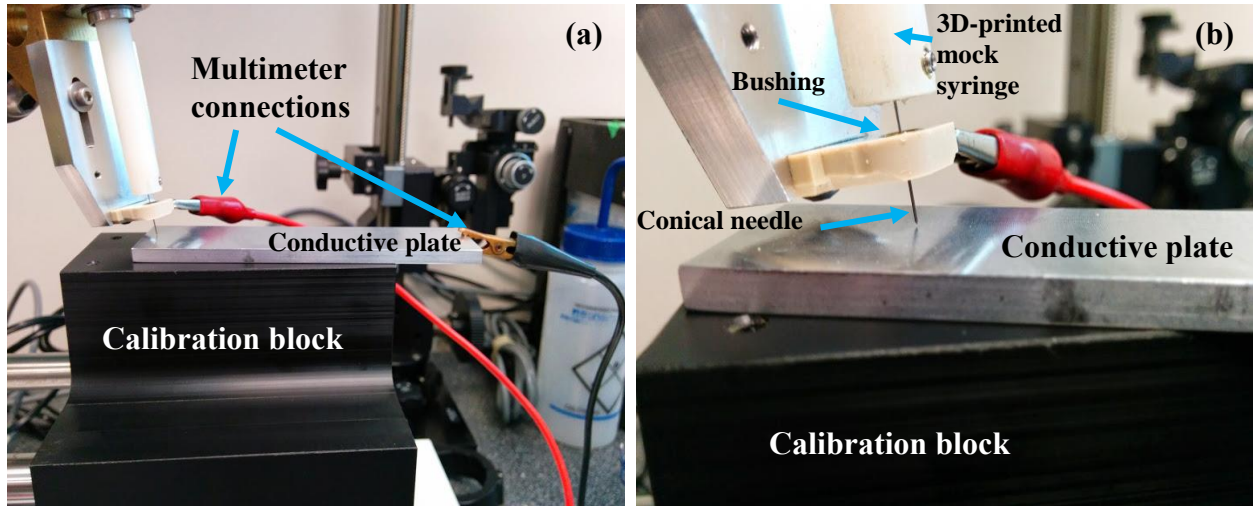


Figure 12: Overview of RCM needle calibration technique developed for the ultrasound-guided device. The top surface of the conductive plate meets the RCM point. Contact between the needle tip and plate is detected by a multimeter. The closed circuit path is such: multimeter → brass bushing → steel needle → aluminum plate → multimeter.

Near the RCM, both CT and ultrasound versions of our robot utilized a tight-fit bushing through which an interventional needle would pass for support, and to ensure it is aligned correctly with the linkage axis approaching the theoretical RCM point. Unique to the newer ultrasound-guided device, we connected this bushing to a multimeter such that when the needle tip would come into contact with a metal surface also connected, a continuity alarm would set off indicating contact (**Figure 12**). Therefore, the calibration-block technique Bax *et al.* used was modified to have a top surface made of electrically conductive steel. Rather than relying on human haptic perception, a connectivity test indicated that the needle tip has reached the RCM point. This is believed to have marginally improved workflow, and comparable calibration error is to be expected although validation of said error could not be determined for lack of CCD camera and macro-lens of equivalent specifications.

2.2.3 Compensation for Needle Bevel

While the robotic device was originally designed to position a conical needle, bevelled needles are typically used in research for general applications. Due to the bevel angle chosen for the application of intranodal injections, it was found there is a considerable offset between the

bevelled needle's tip and the centre of its lumen where substances, such as microbubbles or DCs, exit. Having chosen a 30G needle with an outer diameter of 292 μm and a bevel angle of 12° , there would be an estimated offset between needle tip and lumen centroid of 687 μm . A set of newly ordered 30G needles were scanned in micro-CT for 2.75 hours at 80 kV and 450 μA , and reconstructed yielding an isotropic image with a voxel size of 20 μm (**Figure 13**). The offset between the needle tip and its lumen centroid was manually determined in Microview 3D Image Viewer and Analysis Tool. The average offset measurement was $666 \pm 32 \mu\text{m}$; this mean was chosen as the offset value. The localization error associated with determining this offset was found to be 22 μm .

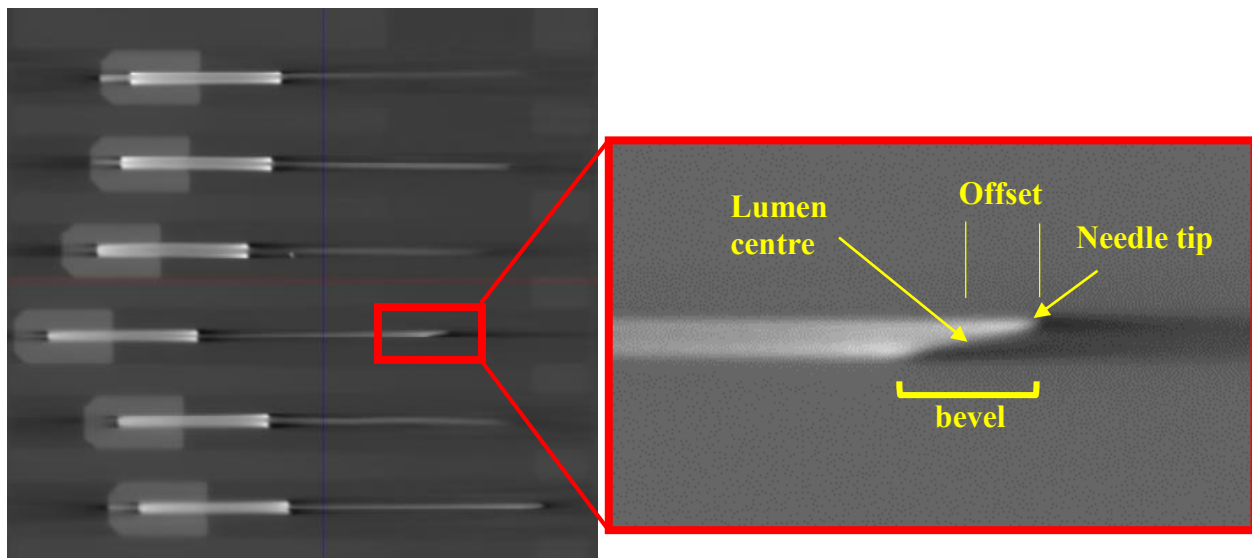


Figure 13: Micro-CT image of 30G needles with 12° bevel angle. Offset was determined by calculating the axial distance between the centre of the lumen and the needle tip.

Two techniques were developed to RCM calibrate a bevelled needle while accounting for the offset between its tip and lumen centroid. The first approach involved two steps. First, a conical needle was RCM calibrated using the fixture-based technique involving electrical contact detection by a multimeter (**Figure 12**). A delrin fixture was then attached to the robot's end-effector. A brass block was placed in a tight-fitting slot in the fixture and slowly advanced towards the needle until contact was made with the needle tip as determined by the multimeter. This depth was then marked using an adjustable dowel pin by locating a precisely placed pin hole in the brass block. The block was then flipped to use the opposite face and set inside the slot of the delrin fixture using the now-fixed dowel pin as a locating point of reference. The distance between each dowel hole and its

corresponding face differed by the lumen-tip offset previously measured in CT ($666\ \mu\text{m}$). After this procedure is completed, it is possible to use this delrin-fixture/brass-block assembly as a tool to set a bevelled needle's lumen centroid at the RCM (**Figure 14**). At the time of design, machining resources were not available to fabricate this assembly. 3D printed versions were also designed; however, the quality of the surface finish and tolerances of the rapid-prototype part were inadequate for this application. This two-step procedure was cumbersome and impractical.

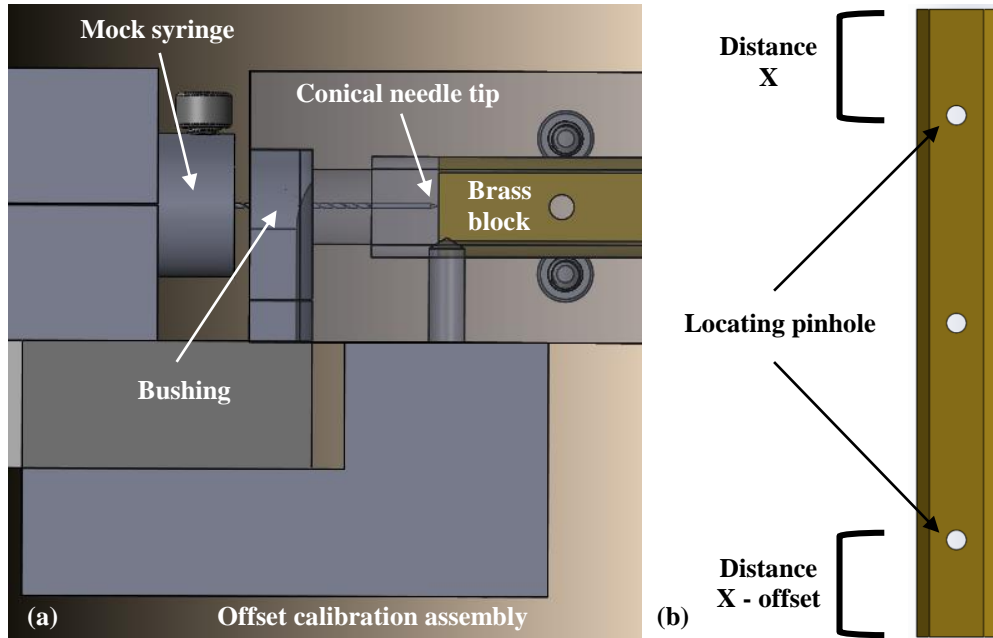


Figure 14: (a) Solidworks model of calibration tool designed to shift the RCM calibration of a bevelled needle mounted on the robot from its tip to the centre of its lumen. (b) Conductive brass block with two precisely placed locating pinholes on either side. The distance between each pinhole and its corresponding side face differed by the lumen-tip offset ($666\ \mu\text{m}$) previously measured in micro-CT.

A one-step technique was also designed to set a lumen centroid at the robot's RCM. This simply involved reducing the height of the conductive plate in the electrical-contact RCM calibration technique for conical needles (**Figure 12**) by a small amount ($650\ \mu\text{m}$), allowing the theoretical RCM point to be located at the centre of a bevelled needle's lumen. This approach was not initially considered since the robot's pitch axis cannot orient the needle normal to the ground (deviation of $\sim 8^\circ$), and a 30G bevelled needle's tip is laterally offset from its centre axis by $145\ \mu\text{m}$. However, these potential sources of error were estimated through basic geometric calculations. More importantly, error in positioning a bevelled needle's lumen on the order of tens

of micrometers is negligible as the lumen, or opening of the cannula, has a considerable length of $\sim 1200 \mu\text{m}$.

2.3 VisualSonics Rail System Error

The VisualSonics railing system serves as a convenient rigid-body structure on which the ultrasound-guided robot and ultrasound transducer can be fixed. This allows for a registration between the two to be maintained during an injection procedure. Target localization in a mouse intervention must be done separately from the injection (i.e. injections are targeted using ultrasound but not monitored in real time). Therefore, after the robot is registered to the ultrasound transducer, it is slid away on the VisualSonics rail. After a target of interest is identified in a mouse using ultrasound, the transducer is slid away from the workspace and the robot is brought back. A hard stop is used as point of reference to return both the robot and ultrasound transducer to the workspace when necessary. This was a potential source of positioning error that needed to be investigated in order to justify not redesigning a custom high-precision rail system.

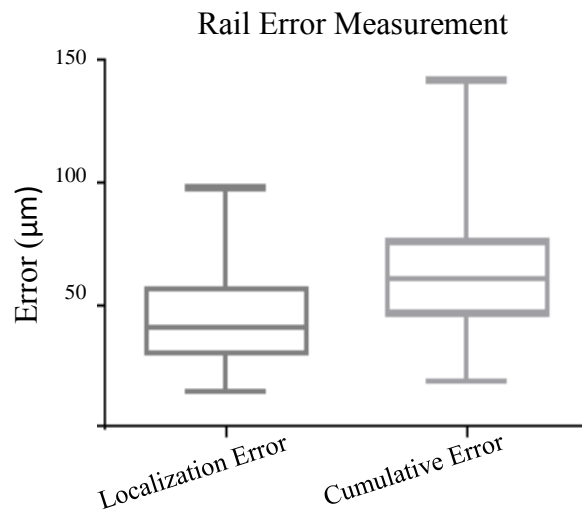


Figure 15: Boxplot comparing the localization error found from consecutive 3D scans of a bead-phantom with the localization error found when removing and repositioning the transducer over the phantom by gliding it along its railing system.

A water-based ultrasound phantom was designed to determine the error attributed to using the VisualSonics railing system. The phantom contained a pattern of 8 fiducial tungsten beads (400 μm diameter). A series of 6 consecutive 3D images were taken of the phantom without moving either the phantom or transducer in between each scan. A second series of 6 images were taken

after moving the transducer away from the workspace by a distance of ~ 8 cm then repositioning at the workspace by relying on a hard stop fixed along the railing. The localization error found from the series of consecutive images was 44 ± 19 μm , while the cumulative error found by localizing beads in images taken after repositioning the transducer was 64 ± 26 μm . Using a nonparametric Mann-Whitney rank-sum test these two values were found to be significantly different ($p < 0.0001$) (**Figure 15**). Subtracting them in quadrature, the estimated error of using the hard stop to reposition the transducer was found to be 20 ± 18 μm . This error is deemed to be marginal in context to our overall targeting injection accuracy of 500 μm . It was decided that developing a more robust railing system for the purpose of image-guided robot injections was not justified. Furthermore, relying on the railing system provided by VisualSonics reduces the cost for an end-user to operate to purchase and operate the robotic device for research purposes.

2.4 Registration Approach

2.4.1 Two-Step Registration Phantom

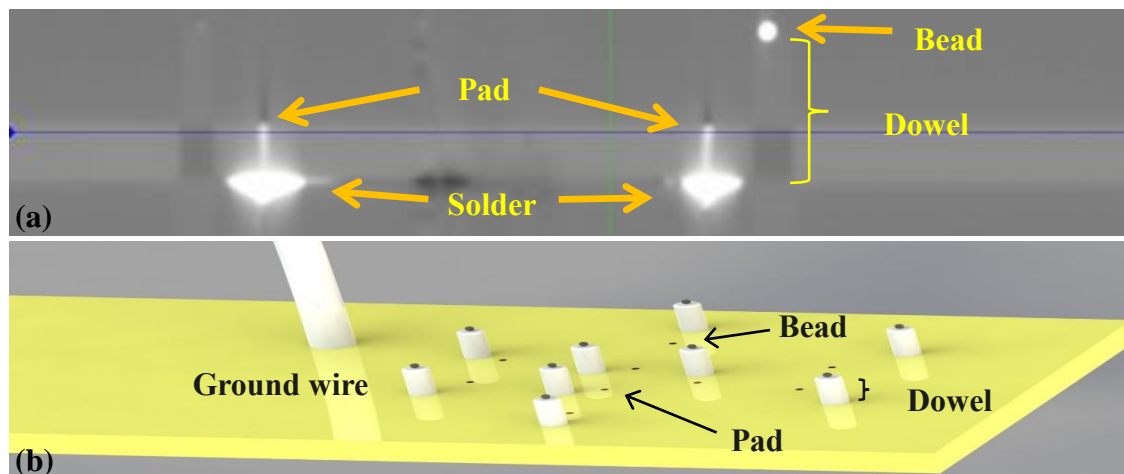


Figure 16: (a) Micro-CT slice of first-generation two-step registration phantom at 49.6 μm isotropic voxel size. (b) Solidworks representation of registration phantom. Each electronic pad is connected to multimeter set to Continuity Test.

As part of the author's ECE 4416 design project, the first technique developed for registering a VisualSonics ultrasound scanner to the robotic device employed printed circuit boards containing a prescribed pattern of nine 317.5- μm diameter conductive pads serving as fiducial markers (6 pads) and targets (3 pads) arranged in a coplanar pattern (**Figure 16**). A three-dimensional stage, controlled by three high-precision (~ 2.5 μm) actuators with encoders, was used

to advance the needle to each fiducial pad. Electrical contact between the needle's tip and each pad was used to determine the pad positions in robot coordinates. Within the registration phantom were 9 small (400 μm diameter) tungsten carbide/cobalt spheres mounted on plastic dowels near each pad. The spatial relationship between each pad and its paired bead was determined beforehand by analyzing a micro-CT scan (with 49.6 μm isotropic voxels) of the phantom. A single 40 MHz 3D ultrasound scan was sufficient to localize all beads. A point-based rigid-body transformation was performed between the ultrasound and micro-CT volumes using the beads as fiducials. A second transformation, between the micro-CT volume and the robot's coordinate system, was performed using the pads as fiducials thereby registering the robot's needle tip location in ultrasound coordinates in two steps (**Figure 17**).

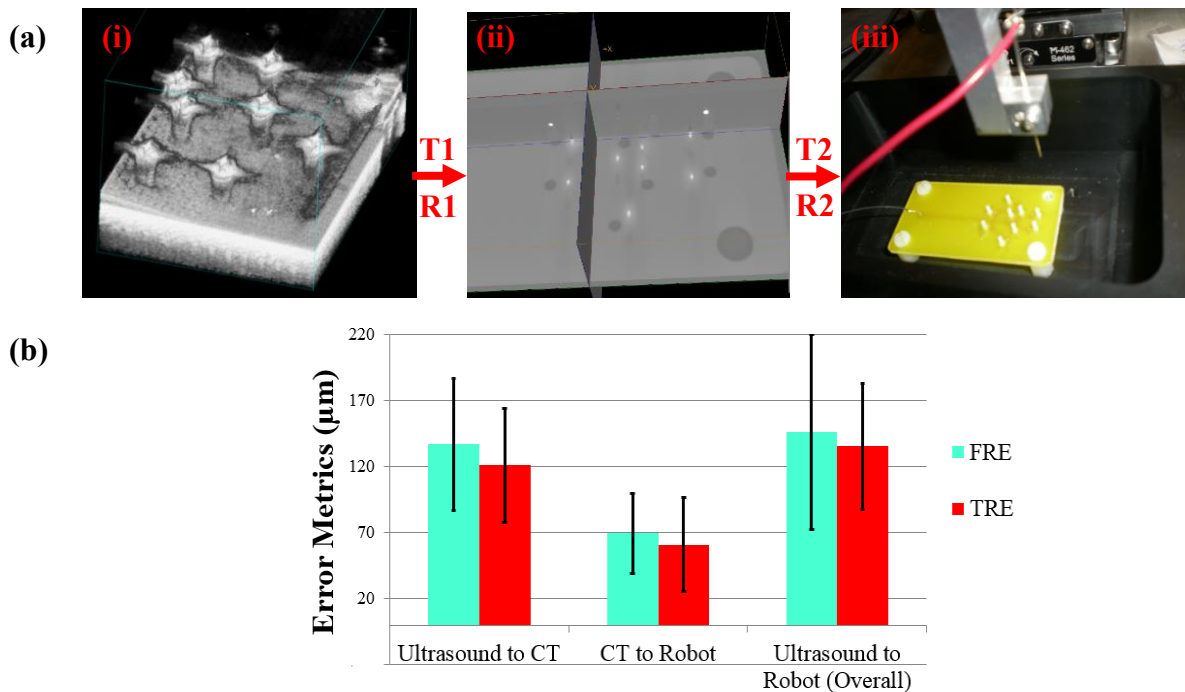


Figure 17: Ultrasound and CT scans of the phantom are linked by a rotation (R1) and translation (T1), while the CT scan of the phantom and the robotic workspace are linked by a rotation (R2) and translation (T2). **(a-i)** Rendering of 3D ultrasound scan of phantom. **(a-ii)** Multiplane view of micro-CT scan of phantom. **(a-iii)** Prototype registration setup. **(b)** The two-step rigid registration process produced an overall FRE and TRE of $146.23 \pm 73.86 \mu\text{m}$ and $135.38 \pm 47.83 \mu\text{m}$, respectively.

The main disadvantage to this initial registration phantom design was that it was water-based. Electrical detection of the fiducial pads by the robot would be performed prior to ultrasound imaging, which used water as coupling agent. This meant that a registration procedure could only

be performed once per day as there was no protocol in place to dry the phantom should it be necessary to repeat. Natural-air drying was relied on. Furthermore, the phantom was vulnerable to damage as the fiducial beads were exposed and easily accessible. The spatial relationship between the fiducial pads and beads, determined from a pre-operative micro-CT scan, was essential to a successful registration. If these beads were displaced by even a single millimeter, it could affect the overall registration accuracy. Therefore, a new design was made.

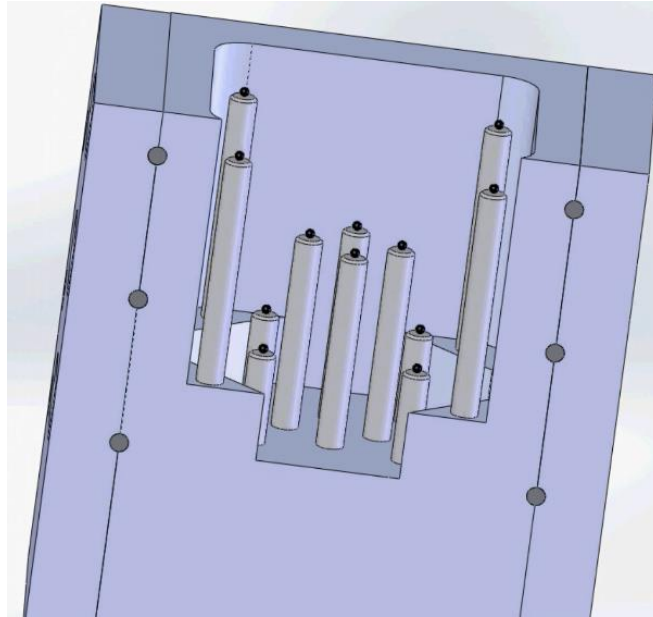


Figure 18: Cross-sectional view of second-generation registration phantom containing 8 outer fiducial beads and 4 inner target beads (observable in ultrasound and micro-CT). Six 2 mm \varnothing steel rods were sharpened at each end to create 8 fiducial, and 4 target, $\sim 50 \mu\text{m}$ \varnothing point-like pads (observable in micro-CT and detectable by the robot's end-effector).

A second-generation two-step registration phantom was designed. Shaped as a cubed box with an open top, the phantom contained 12 (400 μm diameter) tungsten carbide/cobalt spheres strategically placed in a non-coplanar pattern (**Figure 18**). The inside of the phantom was then filled with tissue-mimicking material to allow for ultrasound scanning. On the outside of the cube phantom, 12 robot fiducial pads were placed at heights that roughly corresponded to that of their paired beads located on the inside of the phantom. The same procedure was to be used as in the first-generation two-step registration phantom: a micro-CT scan of the phantom would be taken prior to a procedure to determine the spatial relationship between each bead-pad pair, the robot end-effector would be advanced to each pad until contact was detected by a connected multimeter,

and the fiducial beads would be manually localized from a 3D ultrasound scan of the inner contents of the phantom. However, after construction of the phantom, it was realized that the procedure was too cumbersome. Advancing a needle tip using the robot's 3D stage to multiple pad-like landmarks was a technique that would take several hours to complete. Given that the ultrasound scanner in use for image guidance was not a system solely dedicated to robotic interventions, the registration procedure designed must be completed within a reasonable time frame. Although sufficiently accurate for the small scale of our intended application, this registration technique is not suitable when taking into account several considerations of preclinical workflow. During a targeted injection, a mouse is typically anesthetised using isoflurane; this requires constant monitoring of dosage, body temperature, and heart rate to maintain sufficient anesthesia without overdosing. While the two-step registration allows for good image-to-robot registration, it can take over one hour to complete – close to the maximum knock-out time specified by many animal protocols. Unless done pre-operatively, without an accidental break in registration during a procedure, this registration method is not feasible, and a technique yielding similar accuracy is required.

2.4.2 One-Step Registration

A direct ultrasound-to-robotic workspace registration technique has been developed by visually localizing the lumen of the needle in ultrasound while moving the robot to a number of predefined positions (fiducials) within the ultrasound FOV (**Figure 20**). Some criticisms of direct needle localization in ultrasound versus in CT, as in our first registration technique, include: 1) CT has a higher resolution than ultrasound when radiation dose is not a consideration. 2) Ultrasound images are anisotropic while CT's are isotropic. 3) In ultrasound imaging of needles, there are a variety of artifacts, such as reflection, reverberation, and side-lobe artifacts, which may act as a source of error when localizing the needle lumen.

An experiment was designed to determine the average error introduced by using a registration technique which relies on the ability to accurately and repeatedly localize a needle's lumen in ultrasound. A phantom was constructed to contain a pattern of 8 fiducial beads in the inner corners of a small box, and 3 target beads at the centre of the fiducial arrangement. A needle tip was also placed as the 4th target. The phantom was scanned once in micro-CT (isotropic 20 μm voxel size), and ten times in micro-ultrasound. Registration was performed using the fiducial beads as the common point-set between each image. It was found, using a Mann-Whitney rank-sum test,

that the TRE calculated using target beads was significantly lower ($p < 0.001$) than the TRE of the needle lumen (**Figure 19**). The mean difference in TRE between the target beads and the needle lumen was $\sim 75 \mu\text{m}$. This can be interpreted as saying that localization of the needle lumen in high-frequency ultrasound (the intended image-guidance modality) introduces an additional $\sim 75 \mu\text{m}$ error compared to micro-CT (our gold standard for fiducial localization). This additional error was deemed acceptable and justified a change in registration technique from a cumbersome two-step registration to a faster one-step direct ultrasound-to-robotic-workspace registration.

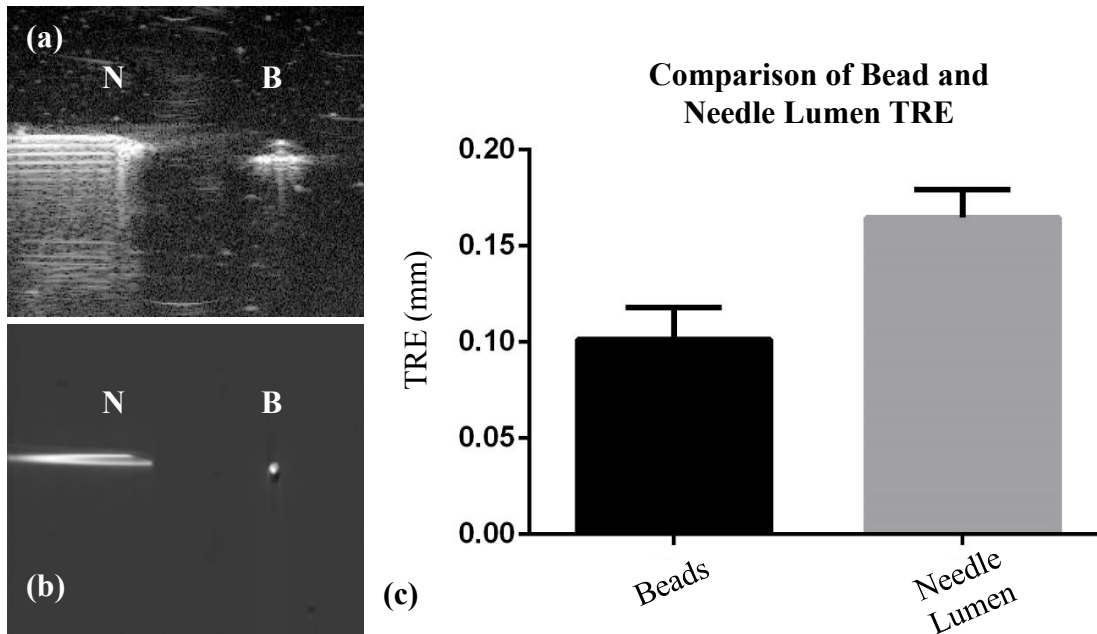


Figure 19: Cross-sectional view of 27 gauge needle, N, and 400 μm tungsten bead, B, scanned in (a) high-frequency ultrasound and (b) micro-CT. A phantom was constructed to determine the error introduced by ultrasound artifacts in localizing a needle lumen in ultrasound versus CT. Ten ultrasound images of the phantom were registered to its micro-CT scan and a Mann-Whitney rank-sum test (c) showed that there is a significant increase ($p < 0.001$) in error when localizing a lumen in ultrasound versus fiducial beads (by $\sim 75 \mu\text{m}$).

The one-step technique was chosen to register the robot to a 40 MHz linear array ultrasound transducer. Using its 3D stages, the robot would move its needle tip to 4 predefined fiducial positions within the field of view of the ultrasound image (**Figure 20**). This was done while the needle was oriented parallel to the transducer and immersed in ultrasound coupling gel within a plastic box. 4 fiducial positions were chosen out of simplicity, although adding more would likely decrease the registration error [45]. Over ten rigid-body registration trials, an FRE and TRE of $113 \pm 105 \mu\text{m}$ and $121 \pm 52 \mu\text{m}$ were found, respectively. Target positions were chosen at the centre

of the fiducial arrangement, which was also the focus of the ultrasound image where a target of interest would likely be positioned during a procedure. The small difference between FRE and TRE was likely attributed to the landmark arrangement. This procedure took 25 minutes on average and yielded results comparable to that of the much more tedious two-step registration. At this stage, a registration technique appropriate for the workflow requirements of the intended application had been developed, and a method to validate the targeting accuracy of ultrasound-guided robotic injections needed to be designed.

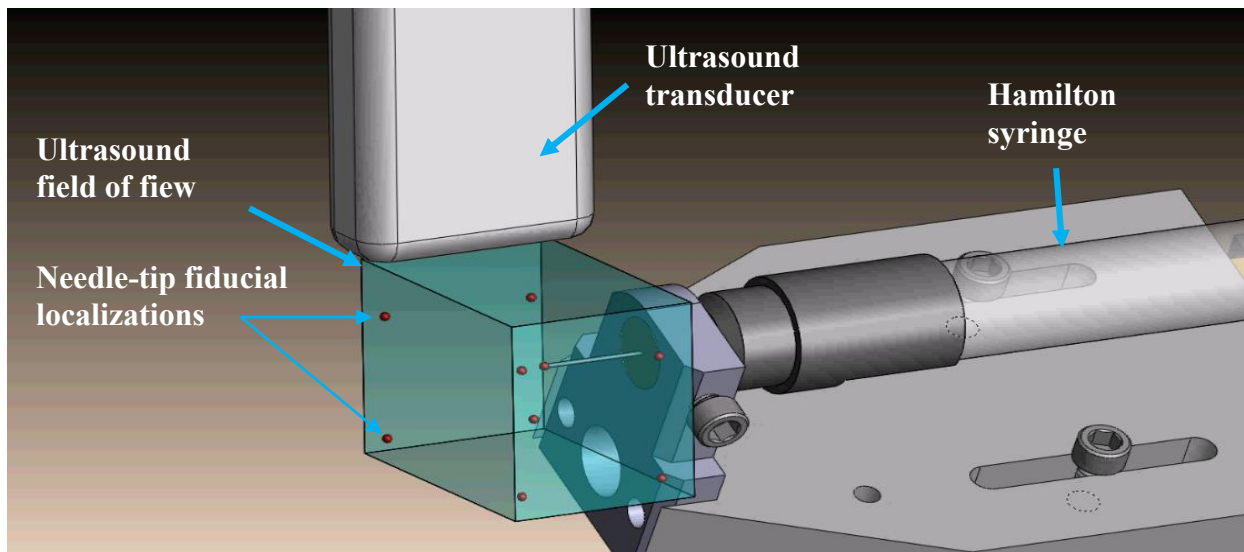


Figure 20: The robot stages are used to move the needle tip to multiple positions in the 3D ultrasound field of view. At each point, the needle tip's lumen centre is localized to collect a fiducial point in ultrasound, while also recording the stage coordinates. Eventually, a common point set is obtained to perform a rigid-body point-based registration.

3 Targeting Accuracy Experiments

Various procedures to quantify the ultrasound-guided needle-positioning robot's accuracy were designed. Six of these procedures are reviewed in the following sections. The most practical validation technique (Section 3.4) was chosen to give end-users the ability to easily assure the quality of the device intermittently throughout their research studies. The chosen approach was also deemed the least likely to introduce intrinsic error to the device's positioning accuracy measurement.

3.1 Air-Track Intersection Targeting Phantom

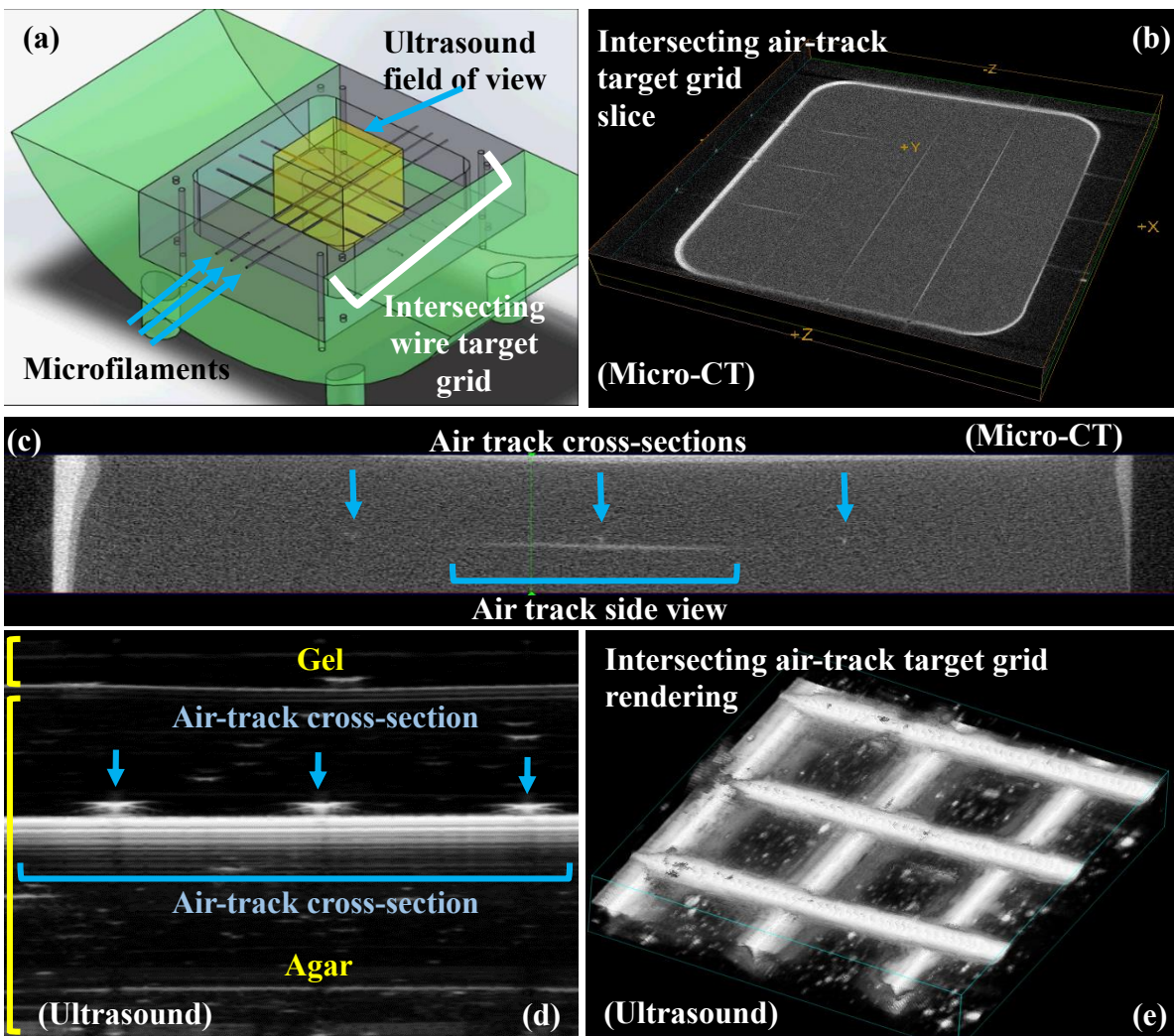


Figure 21: (a) Solidworks model of air-track intersection targeting phantom. (b) Micro-CT slice of targeting phantom with pixel intensities negated. Faint white lines indicate grid pattern of 100 μm \varnothing air channels. (c) Single side-view slice of targeting phantom in micro-CT (negated). Poor

contrast between the air channels and surrounding agar mixture prevented from accurate localization of an intersection target. (d) Single ultrasound frame depicting a typical intersection of air-channels for targeting experiments. (e) Rendering of 3D ultrasound image of targeting phantom. Compared to micro-CT, ultrasound volumes of the phantom contain enough contrast to localize a target accurately and repeatedly.

A targeting phantom was designed and fabricated to contain physical targets to be visualized in ultrasound and validated in micro-CT. This design was based on the first-generation ultrasound-guided robotic device developed by Waspe *et al.* [29]. The phantom was constructed to have a grid pattern of intersecting air channels. Before pouring the agar tissue-mimicking material in this phantom container, a set of six 100 μm diameter microfilament tubes were intertwined to create 9 intersections (**Figure 21 (a)**). Once the poured agar had cooled, the tubes were removed to reveal the air tracks. Each intersection was regarded as a 100 x 200 μm oval target that could be used as a target of interest in an ultrasound-guided injection. In ultrasound, these tracks are easily detected (**Figure 21 (d)** and **(e)**); however, when scanned in CT, there is not enough contrast between the tracks and the surrounding tissue-mimicking material to reliably localize the targets (**Figure 21 (b)** and **(c)**). The experiment protocol involved localizing the intersection target in ultrasound, instructing the robot to position its RCM at the point of interest, driving the needle tip to the RCM point within the phantom, and injecting a barium contrast agent as the robot retracts the needle from the phantom. The contrast-enhanced needle track would be segmented from a micro-CT image of the phantom, and the perpendicular distance would be calculated between the target's centroid and the track's line of best fit (**Figure 22**). This protocol was adapted from Waspe *et al.* [38].

There are some limitations to this approach. First off, this technique provided no sense of depth as the injected contrast agent would leak into air channels and diffuse slightly into the surrounding agar itself. Secondly, the procedure was time dependent as the contrast agent would slowly diffuse into the surrounding agar, making it difficult to segment the needle track. There is also no reliable method to inject the barium contrast agent during needle withdrawal at a constant rate unless medical tubing and a syringe pump are used, which are not compatible with the Hamilton syringe used in the intended application.

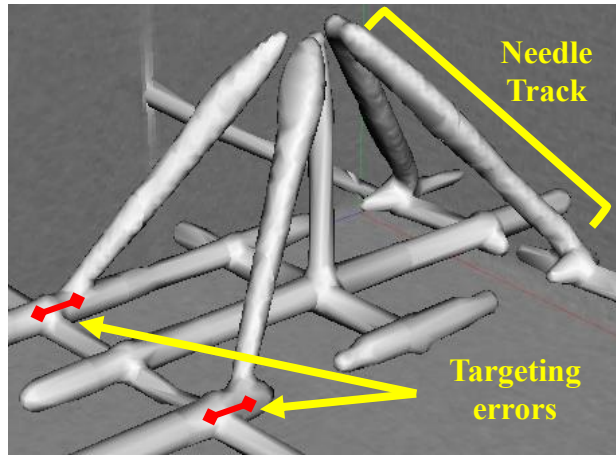


Figure 22: Micro-CT image acquired after injection of barium into air-track intersection targets showing estimation of needle targeting errors. (Adapted from Waspe *et al.* [38]).

3.2 Physical Micro-CT Validation Markers

Rather than relying on the injection of a contrast agent for micro-CT validation of a targeting experiment, the use of physical markers was investigated. In the simplest case, a bead could be deposited as a marker to indicate the exact position of needle tip post-injection. This technique could not be used due to the small needle gauge being used (30 G, 160 μm interior and 315 μm exterior diameter). Miniature certified spherical beads of appropriate CT-compatible material choice could not be found at a size below 200 μm . Instead, two types of markers were used: zirconium oxide beads (2411107, Pacific Star, Houston, TX) and tungsten powder (10402, Alfa Aesar, Ward Hill, MA). Zirconium oxide is a ceramic biomaterial that is being researched as a replacement for titanium dental implants [59]. It has a high Hounsfield unit (HU) of 17,000, while tissue is typically between 100-300 HU. Injecting these small particles into a targeting experiment phantom would leave a small cluster behind. A region of interest would be specified by a user and a threshold-based segmentation could then be performed in MicroView. The segmented volume's centroid would be determined in MATLAB to estimate the correct position the inserted needle reached, and then that coordinate is compared to the intended target of interest. Similarly, tungsten powder of 12 μm ϕ was tested as a physical marker. Incorporated into an agar mixture, this powder can be used in conjunction with 3D printing to create a casting of a biological structure, such as a liver or kidney, that is imaged in CT as a phantom [60]. In both cases, the CT-contrast physical markers were difficult to use in phantom injections. Despite their small size, the

flow of the markers through a 30G needle could not be controlled. The zirconium oxide markers and tungsten powder would rarely fit through the 160 μm inner diameter of a cannula because they tended to clump up in the syringe itself.

Due to the small needle gauge being used for the intended preclinical application, an approach similar to that of brachytherapy, where pellets are loaded into a large needle and deposited after injection, was not feasible. However, a similar technique was investigated. An adapter and larger needle bushing were designed to attach to the Hamilton syringe. Several 2mm \varnothing steel posts were sharpened to create pellets that may be loaded into the syringe (**Figure 23**). The guided injection would be performed by driving the needle into a phantom as usual. Upon retraction, the Hamilton syringe's plunger would be physically fixed such that as the syringe is retracted by the step motor, the plunger pushes the stack of needle pellets forwards, allowing the outermost pellet to be deposited at its driven position. In micro-CT these pellet could easily be segmented due to the high contrast between steel and air in the image; the pellet tip would then be localized manually. Unfortunately, this approach was not taken as 3D printing did not produce an adapter and bushing rigid enough for this application. Machining resources were also necessary to create the fine-point conical pellets. Due to the complexity of the design, manufacturing cost, and several potential sources of error associated with using physical markers for targeting validation (discussed shortly), this approach was not used.

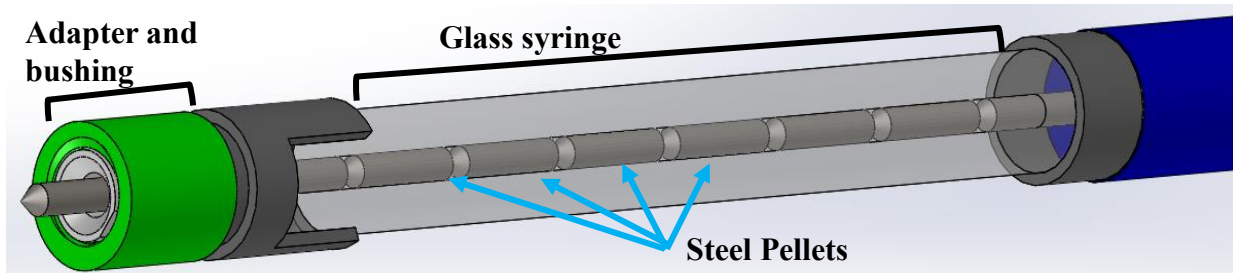


Figure 23: Solidworks model of Hamilton syringe adapted to deposit concentrically sharpened steel pellets. Design was based on 'stacking pencil'.

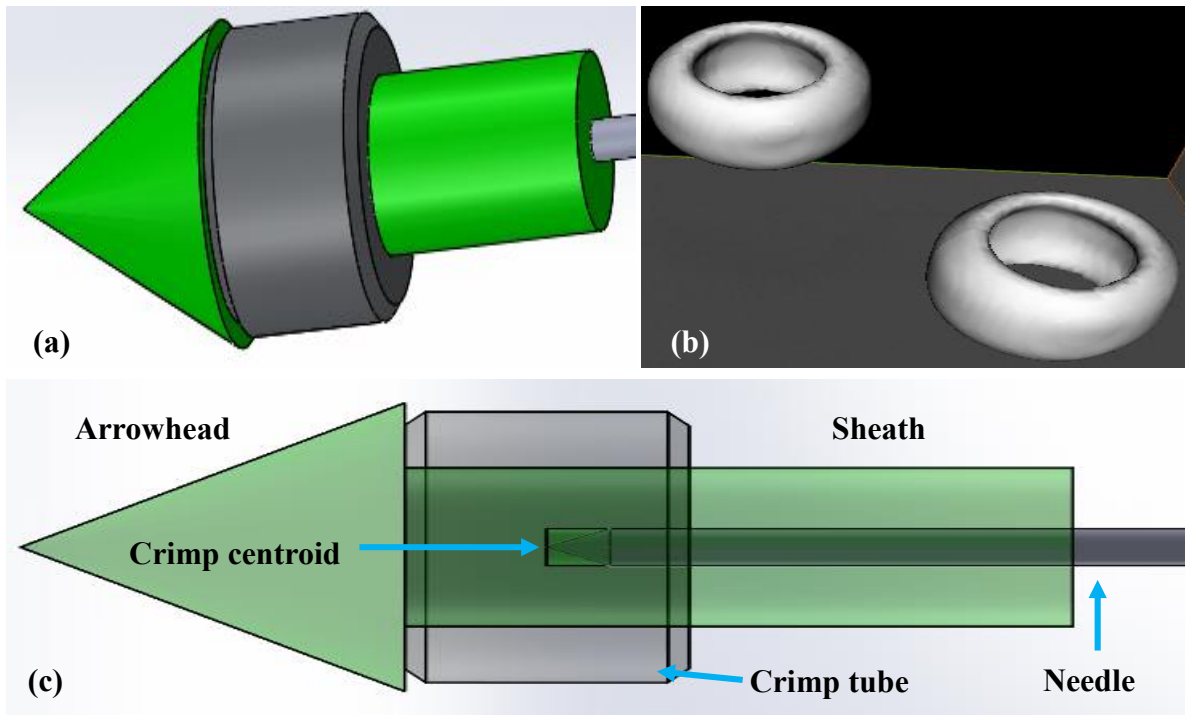


Figure 24: (a) Solidworks model of plastic sheath and silver crimp marker fitted onto a needle. (b) Micro-CT isosurface of silver crimp segmented in MicroView. (c) Transparent Solidworks view of sheath and crimp marker on a needle. The sheath is 3D printed such that the needle tip is placed roughly at the centroid of the surrounding silver crimp.

Another physical validation CT marker designed involved a 3D printed barbed plastic sheath covering the robot-mounted needle (**Figure 24**). The sheath was tightly fitted over the tip of a conical 30G needle. A 1.35 mm long silver crimp, commonly used in jewelry making, was fixed onto the shaft of the sheath such that its centroid was located at the needle tip's position. During a targeting phantom experiment, the sheath would be inserted into the tissue-mimicking material using the robot's driver. During withdrawal, the barbs of the sheath should allow for the ejection of the sheath at its driven position. In micro-CT, the crimp fixed onto the shaft of the sheath should indicate where the RCM-calibrated needle tip was located during the ultrasound-guided robotic injection. A simple threshold-based segmentation was used in order to determine the crimp centroid.

Overall, this validation technique was simple and straightforward, although the fabrication proved otherwise. The durability of the 3D-printed sheaths at such a small size was low because they were sometimes brittle. Furthermore, the support material inherently bound to a freshly

printed part was difficult to completely clean off due to the small size of the part. Stratasys claims the resolution of their Objet 30 Pro printer to be 30 x 30 x 40 μm in the XYZ [61]; the Z resolution was heavily relied upon for accurate placement of the needle tip and crimp centroid at the same position. However, there are several potential sources of error when using a physical marker for a validation experiment. In construction of the barbed sheath, the crimp may have been placed out of position when fixing it manually using adhesives (on the order of tens or hundreds of microns). When transferring a targeting phantom from a procedure to a micro-CT bore, it is possible to knock a marker accidentally. Also, over ~ 2 hours of being exposed to dry air, the tissue mimicking phantom begins to shrink due to the evaporation of the water it contains. While not troublesome for clinical testing, in the pre-clinical setting, when validating the accuracy of a device specified to perform within 500 μm error, the shifting of a physical target due to shrinking of the agar material over several hours during a scan may lead to insufficiently accurate results in defence of the device's accuracy.

3.3 Use of Contrast Agents for Micro-CT Validation

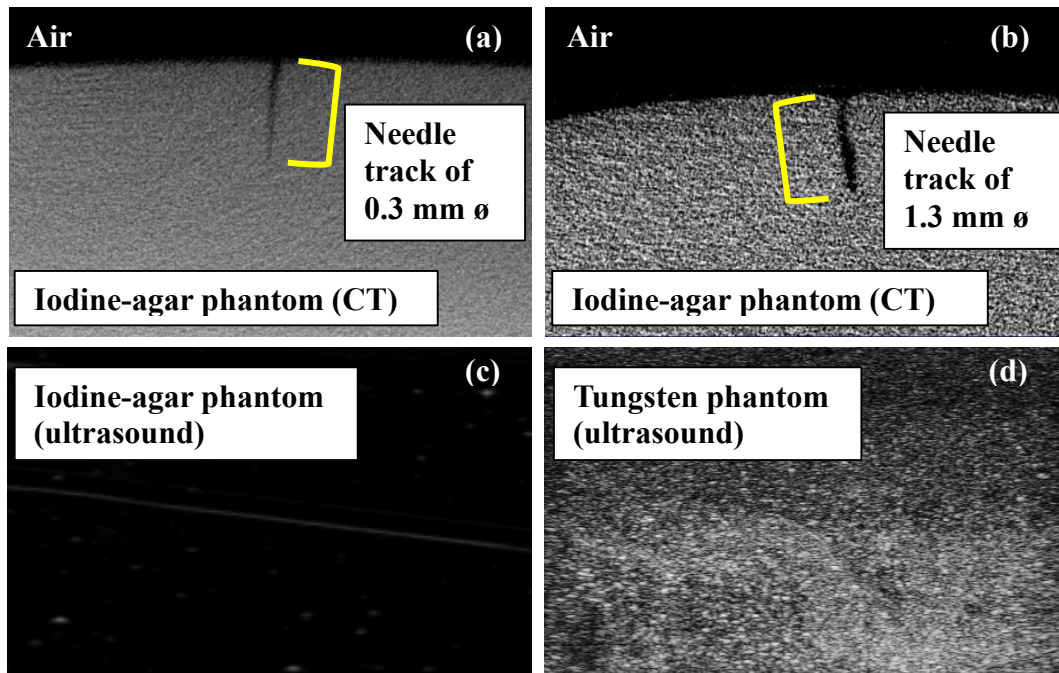


Figure 25: (a) Micro-CT image of agar phantom enhanced with iodine contrast agent. A 30 G needle was used to pierce its surface. (b) Micro-CT image of iodine-enhanced phantom pierced with 18 G needle. This technique could be used to localize needle-track tips in micro-CT for clinical applications, but not preclinical. (c) Anechoic iodine-agar phantom in ultrasound. (d) Tungsten-agar phantom in high-frequency ultrasound.

CT contrast-enhanced phantoms were also developed to view injection tracks in targeting experiments. An organically-bound iodine radiopaque contrast medium (DIN 01904914, Omnipaque 300, Markham, ON) was mixed with agar, glucose, and water to create a contrast-enhanced phantom. The addition of this contrast agent to the agar mixture did not affect ultrasound imaging (**Figure 25 (c)**). The needle gauges used for the intended preclinical application, however, produced tracks that were still not easily detectable in micro-CT (**Figure 25 (a)**) in comparison to clinical-gauge needles (**Figure 25 (b)**). The FLE found when localizing the track tips observed in micro-CT were compared to those found using high-frequency ultrasound as the visualization tool (discussed in **Section 3.4**). The FLE for the tip of a preclinical needle track was significantly lower ($p < 0.0001$) using ultrasound than micro-CT (**Figure 26**).

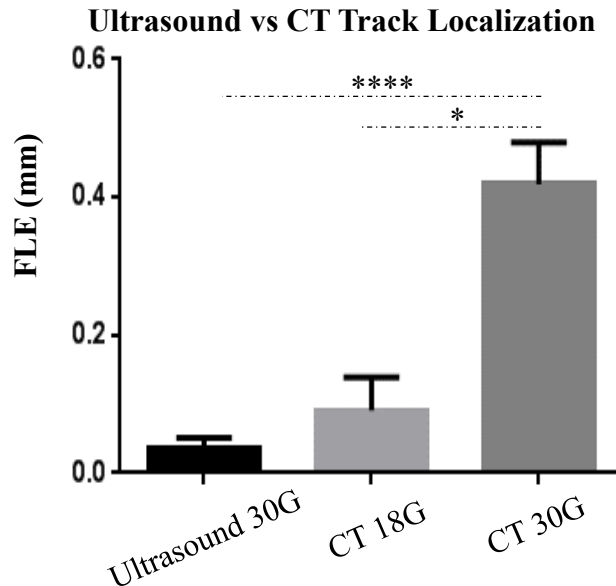


Figure 26: Mean needle-track endpoint FLE in ultrasound and CT for different needle gauges. (Nonparametric one-way ANOVA, Kruskal-Wallis, multiple comparisons, *: $p < 0.05$, ****: $p < 0.0001$, error bars denote standard deviation of 10 trials).

A similar approach was taken by mixing tungsten powder (10402, Alfa Aesar, Ward Hill, MA) into phantoms instead. It was found that at the high imaging resolution of preclinical CT and ultrasound scanners, the 12 μm tungsten particles caused highly granular texture of the tissue-mimicking material (**Figure 25 (d)**) that could easily confuse an operator when localizing targets in such a phantom.

The development of contrast-enhanced phantoms was abandoned; however, the idea of observing the actual track left behind from an injection was much more appealing than depositing a physical marker which may not accurately represent the position of needle tip resulting from an ultrasound-guided injection. The injection of barium, as a contrast agent, into the void generated by the needle track within the phantom brought on diffusion issues of the agent into the surrounding tissue due to its water-solubility. A Microfil® silicone-rubber compound containing lead (MV-122, Flow Tech, Carver, MA) was also tested in phantoms (**Figure 27**). This compound is typically used in non-surviving animals to observe their vascular network structure. It is prepared as a liquid and slowly solidifies with time over several hours post-injection. This agent did not suffer from diffusion issues, however, like other liquid contrast agents, there was a consistent failure to completely fill a needle track over several trials. This was likely due to 1) the tendency of the track void to collapse as the needle is retracted, squeezing out the contrast agent, and 2) the surface tension of the liquid agent injected into the track to that pooled on the top of the phantom.

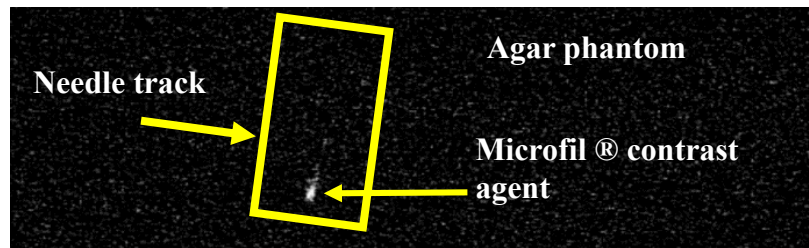


Figure 27: Micro-CT image of Microfil ® contrast agent used in tissue-mimicking phantoms to reveal needle tracks.

3.4 High-Frequency Ultrasound for Validation of Needle Tracks in Tissue-Mimicking Phantoms

A 3D ultrasound image with $40 \times 80 \times 180 \mu\text{m}^3$ resolution acquired using the Vevo 2100 scanner provided acceptable visualization of a needle track in a tissue-mimicking phantom. The localization of needle tracks could be used to validate the targeting accuracy of an injection into phantoms. To investigate the validity of this technique in adequately representing the needle position within an agar phantom, ten injections were performed in a featureless tissue-mimicking phantom. In these experiments, the needles were set in-plane and parallel to the transducer. Fully inserted into the phantom, the needle tip position (**Figure 28 (a)**) would be localized, yielding an

FLE of $37 \pm 14 \mu\text{m}$ (mean \pm standard deviation). Once removed from the fixed phantom, another 3D ultrasound image would be acquired and the track tip positions (**Figure 28 (b)**) were localized (FLE = $57 \pm 35 \mu\text{m}$). For each FLE calculation, a single feature (needle or track tip) was localized ten times within one image. To remove operator bias, the image was closed and reloaded in between localizations. The error between the localized needle tips and track tips was $251 \pm 76 \mu\text{m}$. The magnitude of impact this track-needle error had on the final targeting accuracy results of the manual and robotic injections is discussed in **Section 3.5**.

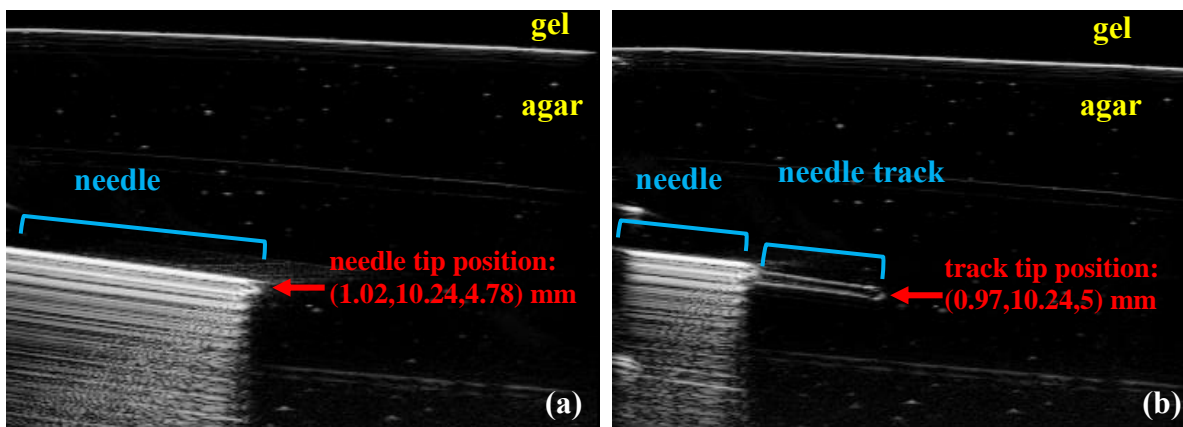


Figure 28: (a) Ultrasound frames of 30G needle inserted into a tissue-mimicking phantom. (b) Needle being removed from phantom, leaving a distinct track that may be localized to estimate where the needle tip was positioned. The Euclidean distance between the needle tip localization and the track tip is the ‘Track-Needle Error’. Ultrasound cine loop of this procedure indicated no deformation of the tracks or surrounding phantom material.

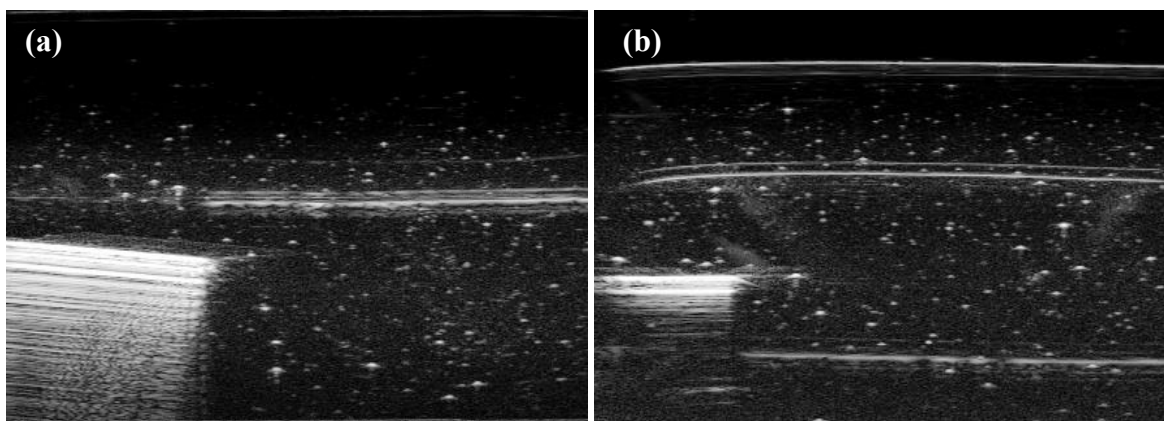


Figure 29: Steel (a) and 3D-printed plastic (b) needles inserted into an agar phantom. Plastic needles appear to result in slightly less artifacts; however, this did not improve needle-tip localization.

Ultrasound visualization of metal needles is plagued by various artifacts; namely reflections and reverberations (**Section 1.5**). The high amplitude reflections tend to overcome apodization leading to apparent side lobe artifacts (see **Figure 8** for example of side lobes). These artifacts make it difficult for an operator to determine where the correct position of a needle tip is within a 3D volume. It was believed that the needle tracks themselves were a better representation of the true injection position than when localizing a metal needle. In an effort to examine the degree of influence metal artifacts had in the offset between needle and track tip localization, 3D-printed replicas of the 30G needles were made (**Figure 30**). They were designed to have a 317 μm diameter with a conical tip, and were connected to an adapter hub to fix onto the Hamilton syringe used for all injection experiments in this thesis. Qualitatively, the ultrasound images of the plastic needles appear to have only slightly less artifacts than images of the stainless needles (**Figure 29**). A nonparametric one-way ANOVA (Kruskal-Wallis) was used to compare the FLE of needle tracks, metal needles, and plastic needles within an otherwise anechoic agar phantom. No significant difference ($p = 0.3241$) was found between each FLE (**Figure 31 (a)**). When comparing the error associated with needle tip localizations, there was no significant difference ($p = 0.9873$) between plastic and metal needles (**Figure 31 (b)**). So the slight reduction in reverberation artifacts using a plastic needle is not sufficient to improve localization of the needle tip. Therefore, the constraint of using standard stainless steel needles imposed by the end user does not appear to have substantially affected the validity of the robot-versus-manual-injector experiment (**Section 3.5**). Use of the methods reviewed in the thesis introduction to mitigate needle artifacts, such as beam steering or echogenic needles (**Figure 3 (c) and (d)**), probably would not have altered the conclusions of this project.

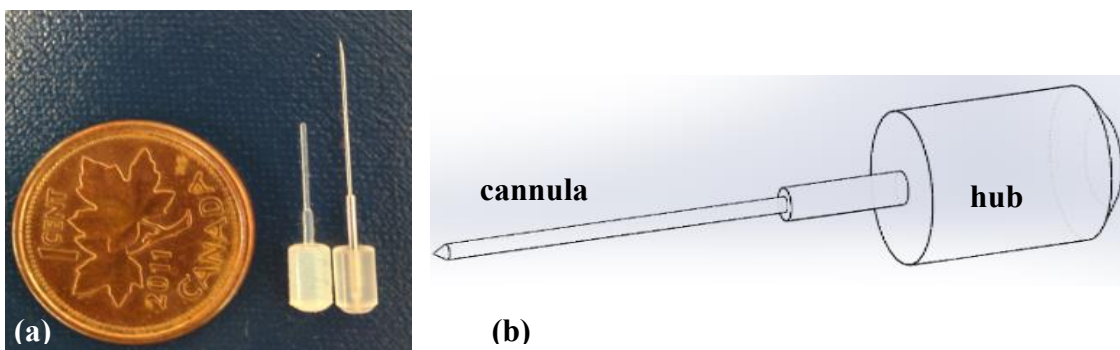


Figure 30: (a) Image of 3D printed plastic needle (left) next to 30G steel needle (right). (b) Solidworks wireframe schematic of plastic needle.

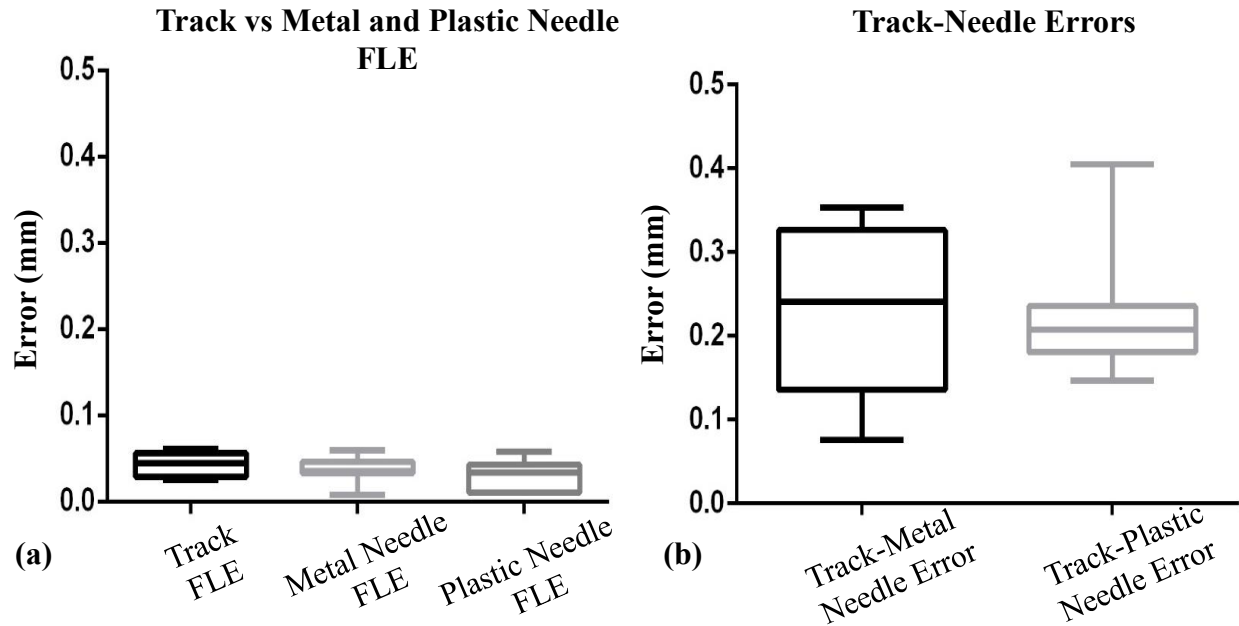


Figure 31: (a) Boxplot depicting the FLE estimate from localizing metal needles, plastic needles, and needle tracks in ultrasound. A nonparametric one-way ANOVA (Kruskal-Wallis) found no significant difference ($p = 0.3241$) between each FLE. (b) Boxplot depicting the track-needle errors found when using both metal and 3D-printed plastic needles. A nonparametric Mann-Whitney test found no significant difference ($p = 0.9873$) between the track-metal needle and track-plastic needle errors.

3.5 Targeting Accuracy of Ultrasound-Guided Robot Versus VisualSonics Micromanipulator

A targeting phantom was designed as a 3D printed box containing an agar material. An array of cones lay 4 mm beneath the top surface of the agar. The vertices of these cones were localized in ultrasound and the midpoint between two adjacent points was considered as the virtual target (**Figure 32**) at which the robot was commanded to place its needle tip. The position that the robot guided the needle toward was estimated using the needle track left behind from each injection.

An ultrasound-guided robot injection trial consisted of localizing ten of these virtual targets in a phantom. An FLE of $39 \pm 16 \mu\text{m}$ was determined by localizing a single virtual target 120 times while ensuring independent trials by reloading the image within the Vevo 2100 software each time. Over ten ultrasound-guided robot-injection trials, a mean \pm standard deviation targeting accuracy

of $285 \pm 94 \mu\text{m}$ was found. This result was comparable to the accuracy of the micro-CT guided device which achieved $149 \pm 41 \mu\text{m}$ [30].

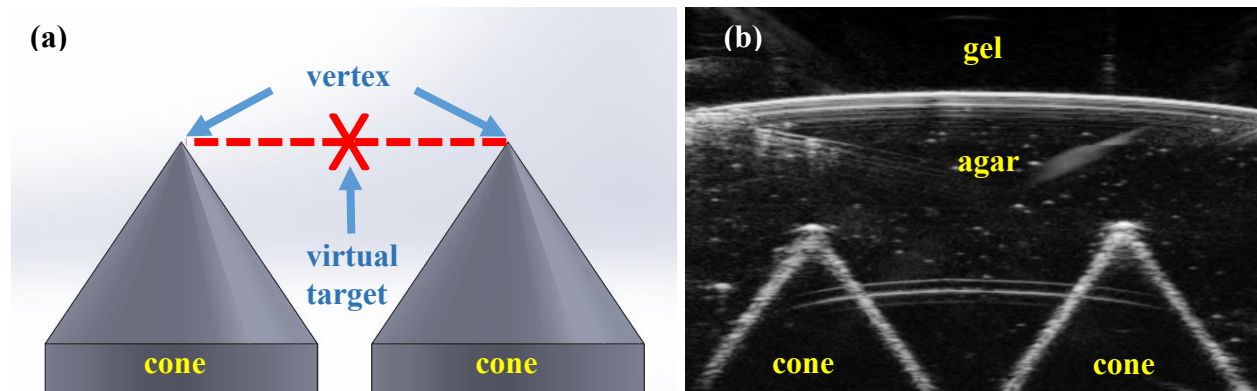


Figure 32: Solidworks model (a) and ultrasound image (b) of targeting phantom. The vertex of each cone is localized to determine the midpoint virtual target for needle placement.

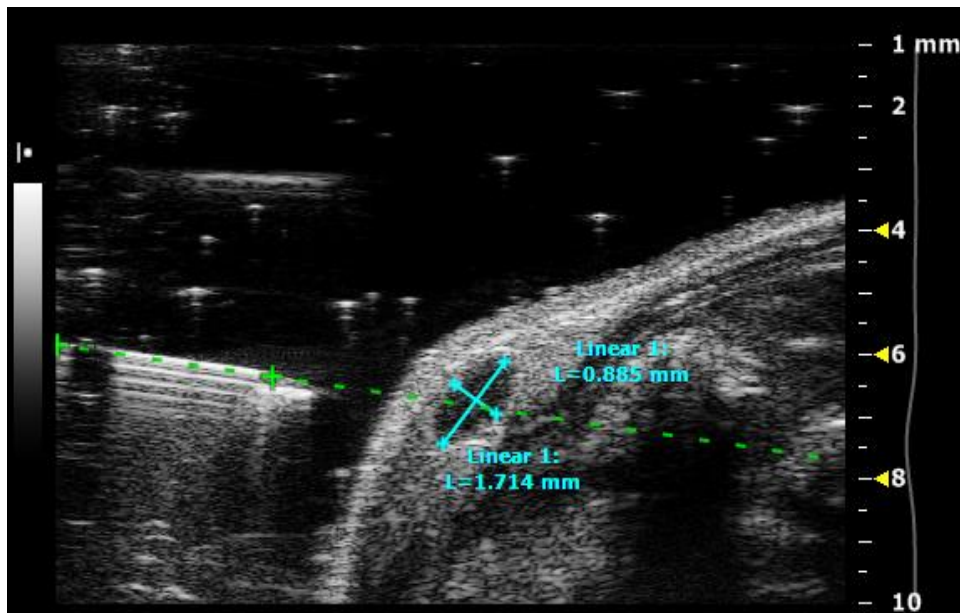


Figure 33: Ultrasound image of a lymph node located within the mammary fat pad of a mouse. The cross-sectional inner-diameter measurements of $0.885 \text{ mm} \times 1.714 \text{ mm}$ indicate the size and position of the lymph nodes. A 30 gauge needle on the left-hand side of the image has been localized within the VisualSonics software, generating an estimated path when driven forward into the lymph node. In this example image, this was the maximum advancement of the needle just prior to the manual manipulator contacting the transducer's side.

The accuracy of the ultrasound-guided robot and manual needle manipulator (**Figure 10**) provided by VisualSonics were compared. When performing image-guided injections using the

manipulator, the needle must be delicately adjusted in position such that it is in-plane with the image, parallel to the transducer. For such an intervention, there is not much space within the field of view to contain both the needle and an object of interest (**Figure 33**). The manipulator contains four degrees of freedom: XYZ translation and a rotation to adjust a needle's angle of approach. Since the Hamilton syringe is clamped at its base when using the manipulator, there is a considerable distance (> 15 cm) between the needle tip and the pivot point about which a rotational adjustment is made during initial setup for an intervention. For this reason, when adjusting the needle's angle of approach, the height and depth of the needle tip must also be adjusted. This procedure can be tedious and tiring as the operator must perform this fine-tuning in several small steps, due to the limited ultrasound-image field of view within which the needle must remain, while monitoring the ultrasound scanner's screen located at least 90° away from the two-handed calibration task located within a biosafety cabinet to permit experiments with immunodeficient mice.

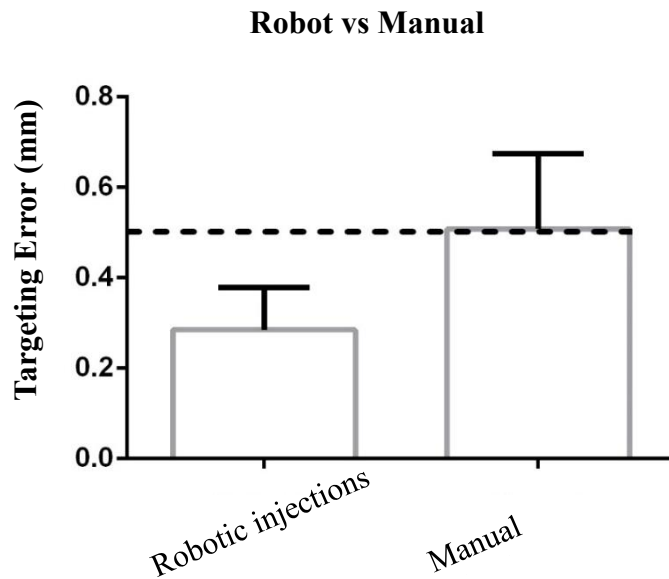


Figure 34: A Mann-Whitney test yielded a significant difference ($p = 0.0029$) between the targeting accuracy of robot and manual injections into tissue-mimicking phantoms. Their means (bars) and standard deviations (error bars) are $285 \pm 94 \mu\text{m}$ and $508 \pm 166 \mu\text{m}$, respectively. Dotted line denotes design goal of 0.5 mm maximum targeting error.

Once an appropriate needle orientation is found, a line is drawn using the Vevo 2100 software by selecting two points along the length of the needle observed in the ultrasound image. The software then extends this line past the length of the needle to give the user an estimated needle trajectory. Once the tedious task of further adjusting the needle is completed, such that its trajectory intersects with the target position within the phantom, the needle is manually driven using the manipulator. The driving depth suffers from a lot of operator dependence as the interpretation of the real-time image feedback during the injection may vary. Over ten trials, using the same needle track localization technique as with the robotic injections, a targeting accuracy of $508 \pm 166 \mu\text{m}$ was found when using the VisualSonics needle manipulator for injections into tissue-mimicking phantoms. A nonparametric Mann-Whitney test was performed comparing the targeting accuracy of the robotic and manual injections and a significant difference ($p = 0.00290$) was found between the two (**Figure 34**).

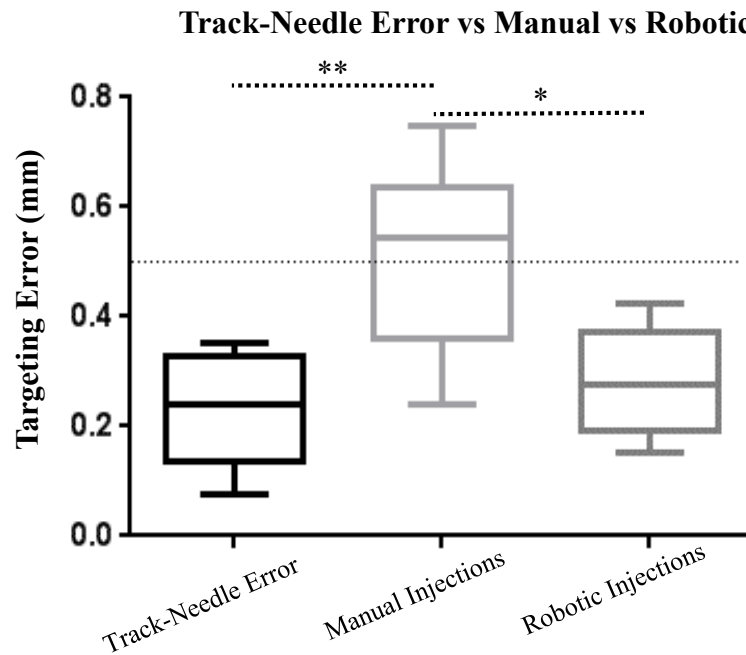


Figure 35: Boxplot depicting the error found when comparing the localization coordinate of a needle tip in ultrasound during an injection into a phantom with the localization of the tip of the track left behind after removal of the needle from the phantom; the manual injection accuracy; and the robotic-aided injection accuracy. A nonparametric one-way ANOVA (Kruskal-Wallis) showed a significant difference between the track-needle error and manual injections, but not with robotic injections. (*: $p < 0.05$ **: $p < 0.01$, error bars denote standard deviation of 10 trials).

In a nonparametric one-way ANOVA (Kruskal-Wallis), the error between the localization of a metal needle and the track it leaves behind (**Figure 28**) in an agar phantom was compared to

the estimated robot and manual injection targeting accuracies, which relied on needle track localization in ultrasound. A significant difference ($p < 0.01$) was found between this track localization error and the manual injection accuracy, but not between the track error and robotic injection accuracy ($p > 0.05$) (**Figure 35**). This suggests that the error in the validation technique of track localization represented a substantial portion of the estimated robotic and manual needle-targeting errors found.

3.6 Ultrasound-Guided Robotic and Manual Injections Performed on Mice

All animal procedures performed for this thesis conformed with Canadian Council on Animal Care guidelines and were approved by the Western University Animal Use Subcommittee.

In preparation for an ultrasound-guided injection using VisualSonics's manual manipulator for steady control of the needle handling, a Black-6 (C57/B6) mouse was stripped of its body hair in the region of interest using depilation cream (Nair®, Church & Dwight Co., Inc., Princeton, NJ). For induction of anaesthesia, 3% isoflurane was used with medical oxygen. 2% isoflurane was used for maintenance during pre-procedural preparation, and the mouse was dosed with 4% isoflurane during the intervention. A centerline incision was made through the dermal layer exposing the abdominal wall cavity. A lateral incision was made at the midline and slightly above the groin to create a flap. The skin flap was slowly peeled back as a scalpel was used to dissect the connective tissue between the dermal layer and the fat pad (**Figure 36**). The skin was then pinned to an agar pad at approximately the same height as the animal's profile. Acoustic coupling gel (Aquasonic, Parker Laboratories, Fairfield, NJ) was applied at the incision area. The MS-550D ultrasound transducer was used to localize the lymph node. Upon aligning the needle in the VisualSonics manually actuated positioning device to be in-plane of the image and en route to the target (**Figure 37**), it was driven towards the lymph node manually while the operator used the real-time image-feedback to determine how far the bevelled tip needed to be driven to break through the soft-tissue wall of the node without accidentally piercing through the structure entirely (**Figure 38**). Once successfully within the target, 25 μL of a tissue marking dye (Triangle Biomedical Sciences Inc., Durham, NC), diluted to 5% concentration, was injected into the lymph node. Immediately after the injection, the animal was euthanized and the node was excised to

determine if the marking dye stained the organ as a supplementary form of confirmation that the target was hit. Close examination showed no sign of staining using the maximum dispensing volume of the syringe (25 μ L). It is postulated that using the tissue dye, at 5% concentration, yielded insufficient colour contrast to visualize the injection bolus.

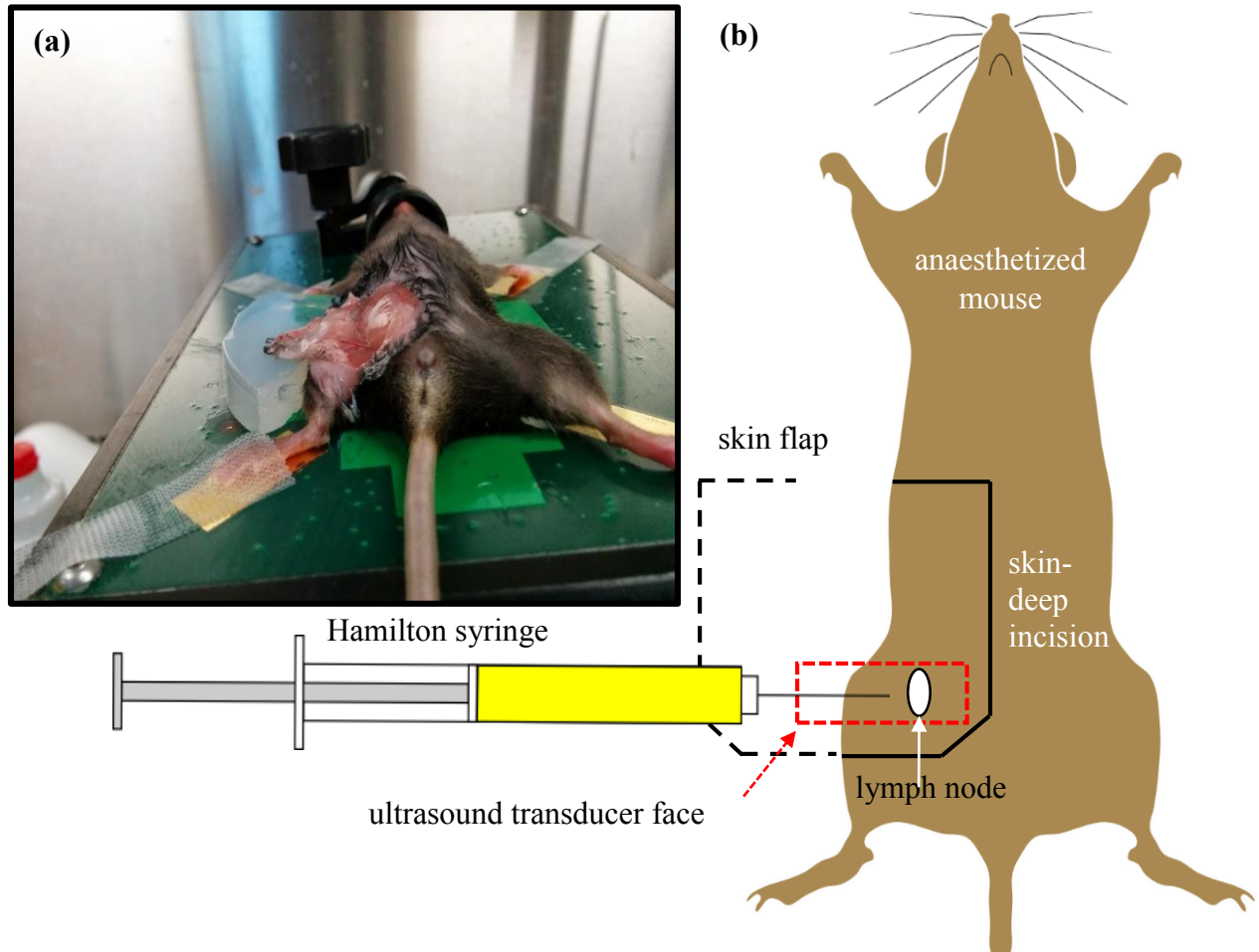


Figure 36: (a) Photograph of mouse surgical preparation prior to ultrasound-guided injection. (b) Illustration of manual injection setup. The solid black line section indicates the region of incision through the dermal layer. The dotted black line indicated where this flap of skin was pinned during the injection. The dotted red line indicates the placement of the ultrasound transducer. The needle is advanced in-plane to the ultrasound image between the transducer face and the mouse's body towards the lymph node.

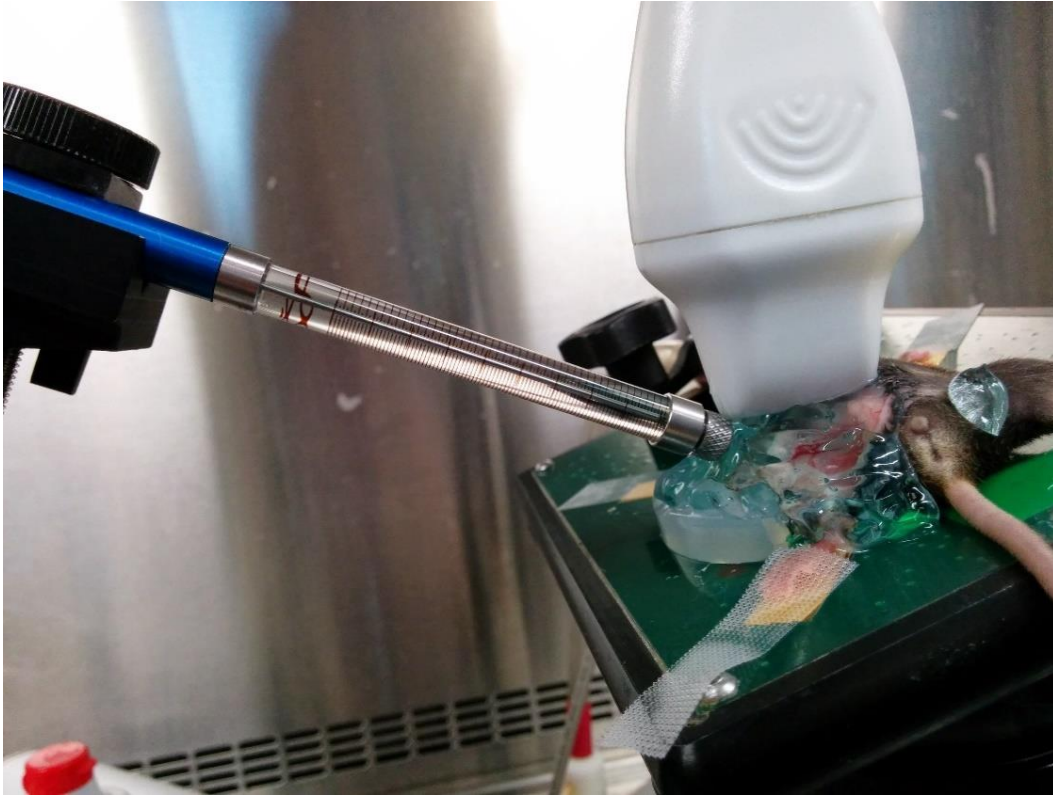


Figure 37: Photograph of ultrasound-guided manual injection in mouse. The needle is carefully positioned between the transducer and the mouse.

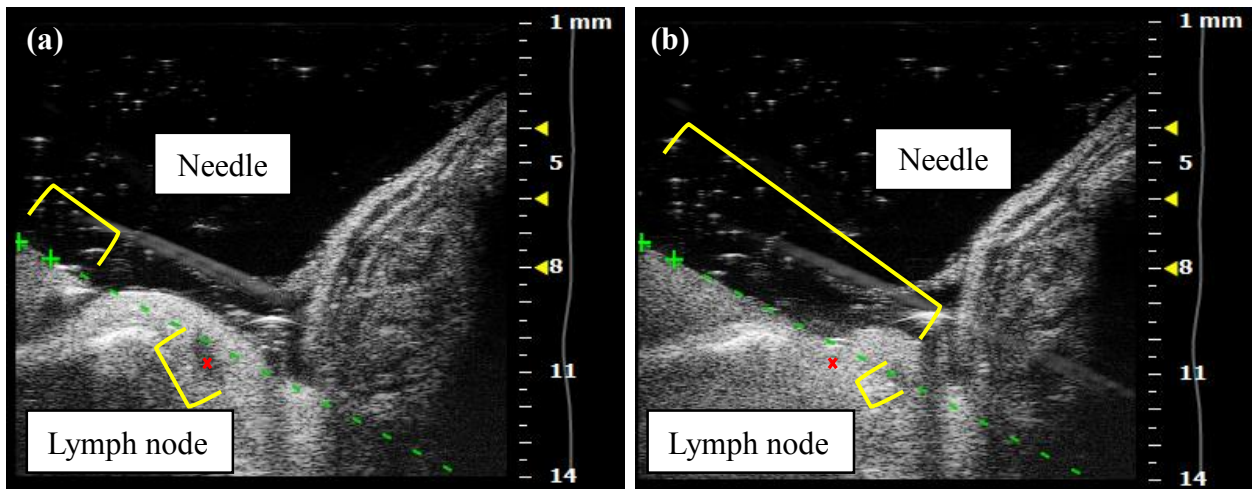


Figure 38: Ultrasound frames of VisualSonics's micro-manipulator manual injection into inguinal lymph node located within the mammary fat pad of a mouse (~ 0.8 x 1.3 mm internal diameter). When visualising such a small target, it is difficult to make adjustments such that both the target and the needle are within the field of view. The needle must be angled appropriately at an inclination that allows the syringe to avoid hitting the transducer upon being driven forwards and for the target to be reached. In (a), a short length of the cannula is visible to position two points

(green +) along the shaft to create a projected trajectory (green dashed line). In (b), the needle has been driven through the mammary fat pad and the bevelled tip is buried within the lymph node. Considerable deformation has taken place, and the initial guess (red 'x') as to the required needle insertion depth has been overshoot by 1.5-2.0 mm.

An ultrasound-guided robotic injection was performed on a live mouse using the same protocol as described above (**Figure 39**). The one-step registration technique was used to link the robotic device's coordinate system with the ultrasound transducer (see **Section 2.4.2**). After registration was completed, the robot was slid away from the workspace on the railing system. The mouse was then prepared and scanned in ultrasound to localize the target lymph node. Once localization was completed, the transducer was slid away from the workspace and the robot was repositioned for injection. Due to the small needle gauge being used (30G) to inject into such a delicate structure, the maximum length of the cannula allowed to extend past the bushing, which keeps it in-axis to the RCM point of the robot, was ~ 14 mm. For this reason, the needle could not be visualized during an injection by the ultrasound probe for image feedback. Robotic targeting accuracy results from phantom experiments were good enough to justifiably say that the robot likely placed the needle where the target was pre-operatively selected within the ultrasound image. But, as in the case of manual injections, the force applied by the needle tip caused a high degree of tissue deformation without piercing the node. Post-injection analysis using ultrasound found no break in the lymph node's outer membrane.

The mechatronic device currently outperforms the manual actuator in terms of simplifying the workflow of an animal injection and in needle placement accuracy, while manual injections outperform in efficacy due to real-time image feedback. VisualSonics's manual manipulator has a cumbersome setup procedure. The needle must be aligned in-plane of the ultrasound slice and must always be visible in the frame. This is because the guidance 'tool' presented in VisualSonics's software package simply involves selecting two points along the cannula visible within the ultrasound frame to create a line which is extended across the screen to project the assumed trajectory of the needle if driven forward. While it has already been shown that this technique yields a larger placement error when compared to that of the robot in tissue-mimicking phantom experiments (**Section 3.5**), it is also very cumbersome, requiring ~ 25 minutes of fine adjustments per injection.

The robotic lymph-node injections, although unsuccessful in terms of validation, demonstrated that the ultrasound-guided mechatronic device developed in this thesis is capable of positioning a needle in an anaesthetised, live mouse within the workflow (and protocol) requirements of *in vivo* animal injections. Performing this experiment allowed for the identification of design modifications necessary to improve the success of minimally-invasive, robotically-actuated intranoal injections in mouse cancer models for the study of dendritic-cell cancer vaccines.

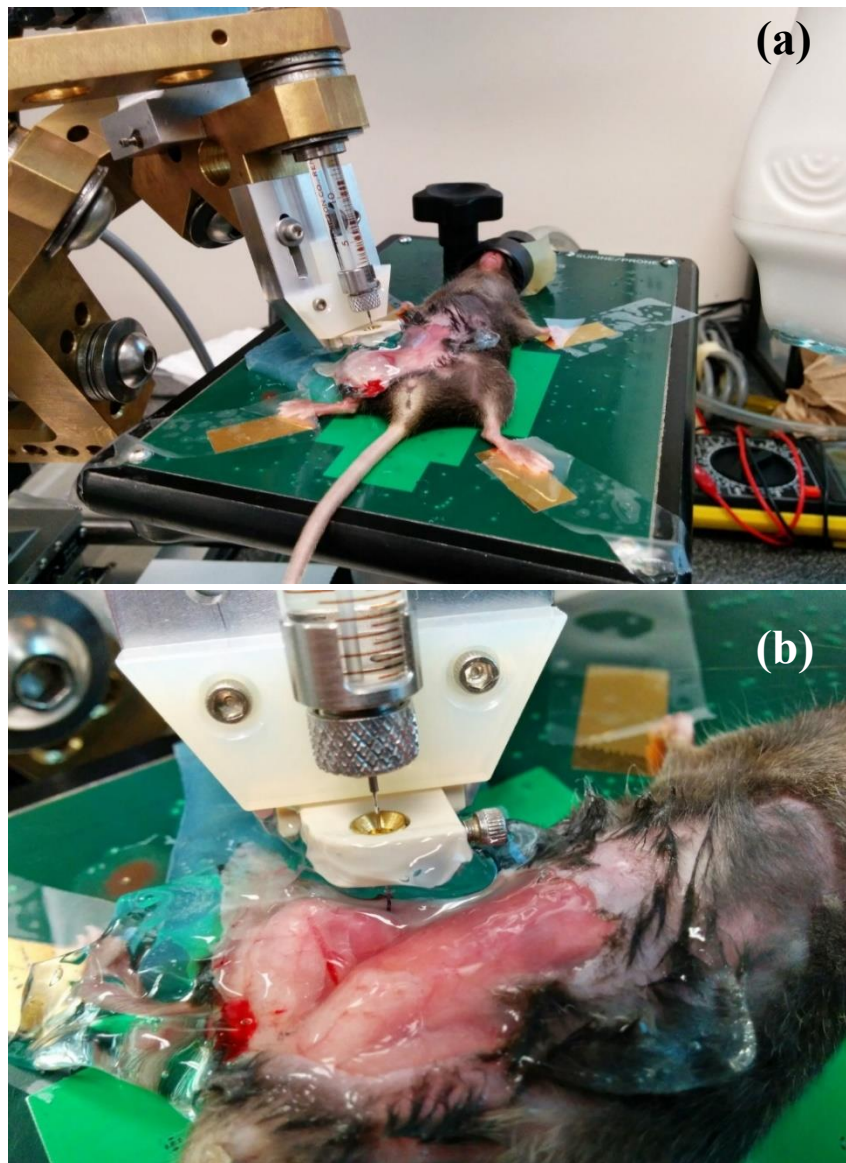


Figure 39: (a) Photograph of robotic injection into anaesthetised mouse's lymph node targeted using high-frequency ultrasound as the guidance modality. (b) Close-up of robotic injection.

4 Summary, Conclusions, and Future Work

4.1 Summary and Conclusions

The purpose of this project was to adapt a micro-CT guided needle positioning robot for ultrasound guidance in small animal experiments involving injections into lymph nodes for dendritic cell cancer vaccine research. This involved designing specific mechanical adaptations, an image-to-robotic-workspace registration technique with reasonable accuracy and workflow, and an appropriate validation method.

4.1.1 Mechanical Hardware

The micro-CT guided injection robot by Bax *et al.* [30] is an RCM design with 6 degrees of freedom: pitch, roll, XYZ, and needle driving. An adaptation of this device to ultrasound guidance allowed for fewer spatial constraints as it does not have to fit within the bore of a micro-CT scanner. However, certain aspects of the device had to be redesigned to allow for smooth operation during an intranodal injection in a mouse. For example, the immunology collaborators strictly specified the use of a near-zero dead-space Hamilton syringe with 30G cannula for injections. This is to avoid the unacceptable loss of precious dendritic cells if delivered through medical tubing. In comparison to the original needle-and-tubing end-effector design of the CT robot, the Hamilton syringe was much too large. One joint of the spherical linkage design of the robot was hollowed out to compensate for the Hamilton syringe, and the needle driver assembly was mounted external to the linkage mechanism in a fashion that would not have fit the requirements of the CT-compatible device.

The ultrasound-guided robot was adapted to operate on a railing system provided by VisualSonics. The railing system serves a rigid structure on which the robot, mouse stage, and transducer is fixed. During a guided intervention, the transducer and robot cannot both fit within the area of interest within the workspace. Therefore, the robot and transducer must take turns and be slid in and out of the workspace as appropriate. This approach may serve as a source of error to the ultrasound-device registration. In order to determine the extent of error introduced, an experiment was performed in which a water-based fiducial-bead phantom was 3D scanned 6 times with the transducer fixed in one position, and then another 6 times after sliding the transducer away

from, and repositioning it to, the region of interest. The localization error found from the control set was $44 \pm 19 \mu\text{m}$ while the cumulative error found by localizing beads in images taken after repositioning the transducer was $64 \pm 26 \mu\text{m}$. A nonparametric Mann-Whitney test found these results to be statistically different, but an estimated repositioning error of $20 \pm 18 \mu\text{m}$ seemed marginal enough to decide against the design and fabrication of a more robust railing system for ultrasound-guided interventions.

4.1.2 Calibration

Bax *et al.* [30] developed two techniques to RCM calibrate a needle on the robotic device. Camera calibrations were more accurate, yielding a $12.5 \mu\text{m}$ error on average. While using a CCD camera for RCM calibration is tedious and time-consuming, a faster approach was also designed such that a delrin block fixture, precisely fixed onto the robot base through high-tolerance machining and assembly techniques, would provide a physical landmark indicating the RCM position. Through trial and error, the needle tip is adjusted gradually towards the top surface of the delrin block until a thin steel shim ($25.4 \mu\text{m}$ thickness), being slid on the delrin surface, is caught by the sharp needle tip. This method yielded an error of $75 \mu\text{m}$ and $12 \mu\text{m}$ in the robot's roll and pitch, respectively. The RCM calibration on the ultrasound-guided device implemented a similar approach; however, rather than relying on a shim to detect correct calibration, a conductive steel plate was used in combination with a multimeter linking the needle and plate. Quantitative validation of this technique was not measured; results comparable to the second approach by Bax *et al.* are expected.

In bevelled needles, there is an offset between the needle tip and centre of the lumen, where substances are ejected from the syringe. Using a 30G ($292 \mu\text{m}$ outer diameter) needle specified to have a sharp 12° angle, there is an estimated $687 \mu\text{m}$ offset between the RCM of the robot and the lumen centre if uncorrected. Five bevelled needles were scanned in micro-CT. The images were analyzed and an offset of $666 \pm 32 \mu\text{m}$ was found. Two techniques were developed to account for this offset when using a bevelled needle on the robotic device. The first fixture-based technique involved calibrating a conical needle on the robot beforehand (using previously mentioned techniques), then mounting a delrin fixture onto the end-effector of the robot. A brass calibration tool is tightly slid into a slot of the fixture until physical contact between its end face "A" and the

conical needle is established using a multimeter. The position of the brass piece is marked using a dowel pin. Flipping the brass piece over to its “B” side and inserting it into the delrin fixture until it reaches the dowel-pin marker allows for an offset adjustment as the difference between side A and B’s spatial relationship to their corresponding dowel holes is equal to the offset of 666 μm . Using this brass and delrin assembly, a beveled needle can now be mounted onto the robot and positioned such that its lumen centre is placed at the RCM. A second technique for correcting this offset involves using the metal-plate RCM calibration technique used for conical needle, while reducing the thickness of the metal plate to account for the offset. This technique relies on estimation because the robot’s pitch axis cannot orient the needle such that it is perfectly normal to the steel plate for calibration, and a bevelled needle’s tip is offset from its centre axis; however, it is simpler and was the preferred calibration technique for all robot injection experiments in this thesis.

4.1.3 Registration

Initially, a two-step rigid-registration technique was designed that relied on a phantom containing fiducial markers that could be localized in high-frequency ultrasound, micro-CT, and using the robot’s positioning stages in combination with an electrical-contact probe. The overall FRE and TRE of this registration were $146.23 \pm 73.86 \mu\text{m}$ and $135.38 \pm 47.83 \mu\text{m}$, respectively. These results, in comparison to the 500 μm needle-positioning accuracy goal of the robot, were acceptable; although, the procedure itself contained workflow issues. A revision to the two-step registration phantom was developed. Electrical pad fiducials were separated from liquid ultrasound coupling agents, and the all fiducials were arranged in a non-coplanar pattern to reduce registration error [45]. Overall, this two-step technique was not feasible due to the time constraints of preclinical workflow.

A one-way registration technique, directly linking an ultrasound image to the robotic workspace, simplifies the initial setup workflow; however, the artifacts produced by a metal needle in ultrasound served as a potential source of error. To investigate this error, a phantom was constructed containing ultrasound/CT-compatible fiducials and a single metal needle. By registering an ultrasound and CT volume of the phantom, it was found that the needle was localized in ultrasound with an estimated error of $\sim 75 \mu\text{m}$ compared to its position as depicted in the gold-

standard 20 μm isotropic voxel micro-CT scan. This additional error was deemed acceptable and justified a change in registration technique from a cumbersome two-step registration to a faster one-step direct ultrasound-to-robotic-workspace registration. By choosing 4 fiducial positions to move the robot-mounted needle tip within the ultrasound field of view, the 3D stages of the mechatronic device were rigidly registered to yield an FRE and TRE of $113 \pm 105 \mu\text{m}$ and $121 \pm 52 \mu\text{m}$, respectively, over ten trials.

4.1.4 Targeting Experiments

Several techniques were developed in pursuit of an appropriate validation technique to quantify the robot's needle-positioning accuracy. The final approach used was chosen based on several factors, including: fabrication feasibility, cost, and inherent error.

A targeting phantom was designed containing agar within which 100 μm \varnothing microfilament tubes were intertwined to create 9 intersections (**Figure 21**). Each intersection could serve as a 100 x 200 μm oval target for an ultrasound-guided robotic injection. To validate the accuracy of an injection in micro-CT, a barium contrast agent could be injected to enhance the track left behind from the piercing cannula. A line of best fit could then be used to determine the minimum perpendicular distance between the injection profile and the intended target, as done by Waspe *et al* [38]. This method could not provide a Euclidean distance error between the target and injected needle tip, and the CT contrast agent tended to diffuse throughout its agar surroundings during a lengthy micro-CT scan.

Due to the small inner diameter of a 30G needle (160 μm), depositing a CT compatible physical marker during a targeting experiment injection was difficult. Miniature certified spherical beads of appropriate CT-compatible material could not be found at a size below 200 μm ; however, two substitutes were found. With a Hounsfield unit of 17,000 HU, zirconium oxide beads, typically used in dental implants, could be easily segmented in a micro-CT image of a post-injection targeting phantom to validate the positioning accuracy of the guided robot. Tungsten powder was also tested as a physical marker for these tests. Overall, these micro-bead markers could not be used reliably for these injections as their flow through the syringe could not be controlled and they tended to clump.

An adapter was designed and 3D printed to modify the Hamilton syringe such that it would be capable of depositing conically sharpened steel rod pellets (**Figure 23**), similar to the approach taken in brachytherapy. While depositing a steel pellet into a tissue-mimicking phantom during a targeting experiment would allow for simple threshold-based segmentation in a micro-CT image to validate its position within the phantom relative to the intended target, 3D printed components and assemblies did not meet the tolerance requirements while machining the product was not time- or cost-efficient. Furthermore, using pellets as a substitute for a preclinical needle for injections would not accurately represent the needle profile expected during an animal procedure.

A 3D printed barbed sheath was designed to be fitted onto a 30G needle as a physical marker for targeting experiments (**Figure 24 (a)**). A silver crimp ring was attached to each sheath, and served as a CT compatible marker which could be easily segmented from a volume by thresholding (**Figure 24 (b)**). During an injection, the sheath would be mounted onto the needle such that the centroid of the silver crimp ring coincides with the needle tip, calibrated at the robot's RCM (**Figure 24 (c)**). During a guided injection, the sheath is driven into a tissue-mimicking phantom, and left behind upon needle withdrawal. A post-injection micro-CT scan could be used to reveal the needle's tip position within the agar phantom by segmenting the highly attenuating crimp ring and determining its centroid in Matlab. This physical marker design was abandoned due to concerns related to the brittleness of the sheaths being rapidly prototyped, as well as the resolution of the 3D printer itself since the accuracy of the CT validation technique heavily relied upon the positioning of the crimp ring and the mounting of the barbed sheath onto a needle.

Adding an organically-bound iodine radiopaque contrast medium to an agar mixture can create tissue mimicking phantoms that reveal needle tracks with good contrast in micro-CT. This approach works well for clinically relevant needle gauges (**Figure 25 (b)**); however, in the case of preclinical gauges, the track, specifically its tip, does not exhibit enough contrast for reliable localization (**Figure 25 (a)**). The FLE calculated when localizing needle tracks in a micro-CT scan of a contrast-enhanced agar phantom was significantly lower ($p < 0.05$) for injections using clinical needles versus preclinical needles. Furthermore, preclinical micro-CT needle tracks have a significantly higher ($p < 0.0001$) FLE than that of preclinical needle tracks imaged using high frequency ultrasound (**Figure 26**).

The injection of a contrast agent into a plain agar phantom to better visualize the track left behind is an alternative to this design which faces its own set of caveats: 1) a needle track formed from piercing a tissue-mimicking phantom with a preclinical needle tends to collapse and squeeze out any contrast agent that may be deposited during the procedure; 2) pooling of contrast fluid on the pierced surface of the agar phantom tends to draw out fluids deposited into the track through surface tension. These issues were not only observed when injecting medical-grade iodine contrast agents into phantoms, but also when using silicone-rubber based contrast compounds which solidify post-injection, such as Microfil®.

A set of 10 needles were injected into a tissue-mimicking phantom and imaged using micro-ultrasound (**Figure 29 (a)**). While both the phantom and the transducer were fixed, the needles were carefully removed from the phantom (**Figure 29 (b)**). The FLEs from localizing a needle and its track in ultrasound are $37 \pm 14 \mu\text{m}$ and $57 \pm 35 \mu\text{m}$, respectively (no significant difference). The error between each needle and its corresponding track it creates upon removal (“track-needle error”) was found to be $251 \pm 76 \mu\text{m}$. A plastic replica of the 30G needle used in this project’s application was 3D printed (**Figure 30**) in an attempt to reduce the influence of ultrasound needle artifacts to more accurately determine the error associated with relying on needle track tip localization as an estimate of the metal needle’s true tip position at the endpoint of a targeted injection. The plastic track-needle error found over ten injections into a plain agar phantom was comparable to that of the metal needle-track error determined (**Figure 31**). Therefore, substituting a different end effector for the metal needle would not substantially change the estimated targeting accuracy.

The validation technique chosen to determine the ultrasound-guided robot’s accuracy involved visualizing two plastic fiducial cones in a 3D printed tissue-mimicking phantom in ultrasound, determining the midpoint of the cone vertices, and performing an injection to that target (**Figure 32**). Post-injection, the track left behind could be visualized using ultrasound, and a targeting accuracies of $285 \pm 94 \mu\text{m}$ and $508 \pm 166 \mu\text{m}$ (**Figure 34**) were found for the robot and VisualSonics manual needle manipulator, respectively. The robot outperformed the manual manipulator in needle positioning accuracy as a significant difference was found between the two ($p < 0.05$). It was necessary to determine how strongly the track-needle error, introduced by using this validation technique, influenced the final robot and manual manipulator targeting accuracy

results. In a one-way ANOVA, the track-needle error was compared to the estimated robot and manual injection targeting accuracies which relied on needle track localization in ultrasound (**Figure 35**). This track-needle error and the manual injection accuracy were significantly different ($p < 0.01$), but the track-needle error and robotic injection accuracy were not ($p > 0.05$). This suggests that the error in the validation technique of track localization represented a substantial portion of both the manual and robotic needle-targeting errors.

Injections were performed on anaesthetized Black-6 mice using both the developed ultrasound-guided robotic device and the VisualSonics micro-manipulator. A centerline incision was made through the dermal layer of each mouse to expose the abdominal wall cavity. The ultrasound transducer was used to visualize the target lymph node. When using the micro-manipulator, the needle was positioned in-plane and near parallel to the transducer; while driving the needle forwards to pierce the lymph node, the operator monitored the real-time image feedback from the ultrasound scanner. Once successfully within the target, 25 μL of a tissue marking dye, diluted to 5% concentration, was injected into the lymph node. Immediately after the injection, the animal was euthanized and the node was excised to determine if the marking dye stained the organ as a supplementary form of confirmation that the target was hit. During robotic injections, the ultrasound transducer was momentarily used for target visualization, then removed from the workspace to introduce the robot. Using the registration between the robot and transducer, the robot was capable of targeting the lymph node. However, without the ability to monitor the injection in real time due to a maximum exposed cannula length of 14 mm for this preclinical application, validation was not possible. In both manual and robotic injection, no tissue staining was observed from the marking dye.

4.2 Future Work

4.2.1 Ultrasound-Guided Interventional Platform Modifications

The VisualSonics railing system serves as a platform to attach a high-frequency ultrasound transducer and a needle-driving device. It is important that the system be rigid and withstand deflection from outside forces, either accidental or routinely applied within the typical workflow. Adapting the presented robotic device to the VisualSonics railing system, rather than developing a custom railing, allows for a reduced cost to the end user, and increases the likelihood of future

researchers adopting such a tool. However, there are disadvantages to its use. The material of the arm on which the ultrasound probe is fixed has a relatively low stiffness, and the joints have a low tolerance, leading to a considerable amount of play, potentially causing an error in the robot-to-ultrasound registration. Furthermore, the transducer arm of the railing system has no counterbalance. Application of the manual locks/breaks, after moving the transducer from one position to another, caused the transducer to sway to a degree that is visible to the naked eye. The transducer arm, mouse stage, and robot all ran across the railing using plastic plain bearings that rely on the surface rubbing contact. This made for the sliding of a component to be quite rough, sometimes leading to vibration. The robot itself weighed approximately 50 lbs, making its movement across the railing quite a strenuous step for the operator.

To ensure the functional accuracy of the overall robotic system, it is paramount to create a dedicated railing system to rigidly maintain the accuracy of a robot-to-ultrasound registration. High-tolerance joints and a linear ball-bearing railing system should be used to ensure smooth transport of the robot or transducer arm (aluminum or steel) from one point to another during a procedure. Magnetic hard stops may be used to repeatedly remove and reposition a component to a point of reference; such a system was developed by Waspe *et al.*[29]. This investment into the image-guided system to minimize the sources of error when using the robot device in practice will be worthy of the time and effort put into designing and fabricating the device to perform with such great accuracy and precision.

4.2.2 Compensation of Tissue Deformation

Control of needle-tissue interactions is a critical factor in the development of small-animal robotic needle-positioning systems. Two options exist to control needle and tissue deflections: minimization of the deflections and correction of the remaining deflections. The magnitude of needle and tissue deflection can be minimized using several techniques. Studies have suggested that high-speed needle insertions can reduce needle deflection and tissue deformation [62], [63]. In one variation, needles may be gradually driven, or tapped, towards the target in the tissue at high velocity to reduce deformation [64]. To achieve high velocities or tapping motions needle drivers may implement high-speed actuators such as spring-loaded mechanisms or pneumatics. Deformation can also be reduced by rotation of the needle, in a fashion similar to drilling, during

insertion [62], [65]. However, when rotating the needle lower insertion speeds may better reduce deformations. Rotation could be accomplished using either a lead screw or torsional spring mechanism. Several techniques can also be implemented to correct any needle or tissue deformation which does occur.

Needle deflection can be predicted through simulation [66] or determined experimentally for the robotic system in various tissues and needle gauges. The targeting position of the robot could be adjusted an amount corresponding to the deflection to cause the needle tip to deflect back towards the target. Alternatively, Abolhassani *et al.* [62] demonstrated that needle deflection can be estimated intraoperatively by measuring forces and moments acting on the needle base. The needle trajectory can be corrected in real time to adjust for the estimated deflection. Using this technique needle deflection error was reduced by 90%. Assuming the technique can be scaled to the micron scale of small animal interventions it could be used to significantly reduce the effects of needle deflection. A number of promising methods exist that can be incorporated into future robotic systems for small animal interventions to reduce the effect of needle and tissue deformation on targeting accuracy [62], [66].

Pilot injections into the lymph nodes of mice were performed using both VisualSonics's manual actuator and the ultrasound-guided robot developed. In both cases, it was observed that tissue deformation was the main issue. This means that when planning an ultrasound-guided injection, it is often required to overshoot past the initial planned depth to reach the target. For this reason, the outer dermal layer of the mice used in our pilot injections was removed.

While the ultrasound-guided mechatronic device provides for minimal positioning needle placement error ($285 \pm 94 \mu\text{m}$) and efficient workflow, modifications must still be made to compensate for tissue deformation when targeting any internal structure of a mouse. Due to the delicate nature of intranodal injections in mice, small needle gauges must be used (30 G - 32 G). For this reason, a relatively short length of cannula ($\sim 14 \text{ mm}$) may be extended past the robot's RCM-aligning end-effector bushing. This current setup prevents coincident transducer imaging of the lymph node during a robotic injection. In order to compensate for this lack of real-time image feedback to monitor tissue deformation, future studies in which a manual syringe manipulator, operated with ultrasound image feedback and equipped with a force sensor, may be used to

correlate force signals from the sensor with ultrasound observations of a structure (i.e. mouse skin layer, lymph node outer membrane, etc.) being pierced. Using this information, force feedback may be used as an alternative to image feedback, which must be the case with mouse models being injected with small needles gauges. Controlling the depth of needle insertion is paramount to dealing with tissue deformation, so the needle driver of the mechatronic device will have to be modified accordingly. Alternatively, if a larger animal were used for the intended preclinical studies, such as rats, it may be possible to use larger, more rigid needle gauges (23 G – 27 G) which can be extended further past the robot's bushing. Using rigid, longer needles would provide a greater opportunity to introduce the ultrasound transducer to the workspace during a procedure to provide image feedback without colliding into the robot's end-effector itself. With support from VisualSonics Inc. to allow either live streaming images through an output port on the scanner or to modify their software to perform target tracking, it could be possible to enable closed-loop guidance using a Vevo 2100 transducer. Tracking the deformation of tissue during an injection would allow for optimized depth insertion for a selected needle trajectory.

An immunology study will be performed on small-animal cancer models to compare the migration rate of dendritic cells into the lymph node between two delivery methods. 1) Freehand injections will be performed either subcutaneously or more invasively by surgically exposing the target of interest and injecting directly into it. 2) Direct intranodal injections will also be performed using the image-guided robotic device developed in this thesis. After examining the effectiveness of these two delivery methods, the biological efficacy of the cancer vaccine may be evaluated as well – although there are a number of biological factors outside the control of the robot that will affect the therapeutic efficacy. Post-procedure, the animal will be euthanized and the lymph node excised for quantitative histological analysis. The future hypothesis will be that ultrasound-guided intranodal injections improve the efficacy of dendritic-cell cancer vaccines over conventional drug delivery methods such as subcutaneous or intradermal injections.

4.2.3 Clinical Translation

The robotic device should make cancer immunotherapy experiments in mouse models more efficient and repeatable. Such preclinical experiments have the potential to improve understanding of the factors that influence the effectiveness of DC-based cancer vaccines in human

patients. In addition, while lymph node injections in humans may be done manually due to the relatively larger size of the targets, our immunology collaborators hypothesize that specific subcapsular regions of human lymph nodes should be targeted for cancer vaccine delivery, requiring an accuracy comparable to that of the presented device. Based on the current designs and techniques developed for animal interventions, a larger scale ultrasound-guided device could conceivably be made to aid in such a human application.

4.3 Conclusion

A mechatronic needle positioning device has been adapted for high-frequency ultrasound guidance. The device was redesigned from its original CT-guided edition to be easily integrated onto a commercially available VisualSonics imaging rail system. Subtle modifications were made to ensure simple workflow that allows for live-animal interventions that fall within the maximum anaesthesia periods (typically < 1 hour) stated in study protocols. The robot's remote centre of motion calibration technique was modified to account for the offset between a needle's tip and the centre of its lumen, where substances are ejected. A fast one-step robot-to-ultrasound registration technique was developed in which, using its 3D stages, the robot would be moved to 4 fiducial positions. The needle tip would be localized in the ultrasound image at each position and related to the robot's coordinate system through a rigid registration. Fiducial and target registration errors of $113 \pm 105 \mu\text{m}$ and $121 \pm 52 \mu\text{m}$, respectively, were found for the one-step registration method. A validation technique was developed to determine the targeting accuracy of the needle-positioning robot to a precision sufficient to establish the effectiveness of the system for preclinical interventions. Ultrasound-guided injections into a tissue-mimicking phantom revealed a targeting accuracy of $285 \pm 94 \mu\text{m}$ for the robot compared to $508 \pm 166 \mu\text{m}$ for a commercial manually actuated injection device. The mean targeting accuracy of the robot therefore exceeds both the accuracy of the manually actuated device and the < 500 μm accuracy required for the initial intended application of injecting cell-based cancer vaccines into the lymph nodes of mouse cancer models. Pilot injections were performed using the robotic device in live mice to demonstrate the feasibility and relative workflow efficiency of the robot versus the manual actuator.

References

- [1] J.-P. Bonjour, P. Ammann, and R. Rizzoli, "Importance of Preclinical Studies in the Development of Drugs for Treatment of Osteoporosis: A Review Related to the 1998 WHO Guidelines," *Osteoporos. Int.*, vol. 9, no. 5, pp. 379–393, Apr. 1999.
- [2] A. Draube, N. Klein-González, S. Mattheus, C. Brilliant, M. Hellmich, A. Engert, and M. von Bergwelt-Baildon, "Dendritic Cell Based Tumor Vaccination in Prostate and Renal Cell Cancer: A Systematic Review and Meta-Analysis," *PLoS ONE*, vol. 6, no. 4, pp. 1–11, Apr. 2011.
- [3] G. R. Martin, "Isolation of a pluripotent cell line from early mouse embryos cultured in medium conditioned by teratocarcinoma stem cells," *Proc. Natl. Acad. Sci.*, vol. 78, no. 12, pp. 7634–7638, Dec. 1981.
- [4] Y.-Q. Zhou, F. S. Foster, B. J. Nieman, L. Davidson, X. J. Chen, and R. M. Henkelman, "Comprehensive transthoracic cardiac imaging in mice using ultrasound biomicroscopy with anatomical confirmation by magnetic resonance imaging," *Physiol. Genomics*, vol. 18, no. 2, pp. 232–244, Jan. 2004.
- [5] A. Liu, A. L. Joyner, and D. H. Turnbull, "Alteration of limb and brain patterning in early mouse embryos by ultrasound-guided injection of Shh-expressing cells," *Mech. Dev.*, vol. 75, no. 1–2, pp. 107–115, Jul. 1998.
- [6] M. L. Springer, "Closed-chest cell injections into mouse myocardium guided by high-resolution echocardiography," *AJP Heart Circ. Physiol.*, vol. 289, no. 3, pp. H1307–H1314, May 2005.
- [7] J. C. Slevin, L. Byers, M. Gertsenstein, D. Qu, J. Mu, N. Sunn, J. C. Kingdom, J. Rossant, and S. L. Adamson, "High resolution ultrasound-guided microinjection for interventional studies of early embryonic and placental development in vivo in mice," *BMC Dev. Biol.*, vol. 6, no. 1, pp. 1–14, Dec. 2006.
- [8] P. G. Koutrouvelis, "Stereotactic device," 5575798, 19-Nov-1996.
- [9] E. L. Ritman, "Micro-Computed Tomography—Current Status and Developments," *Annu. Rev. Biomed. Eng.*, vol. 6, no. 1, pp. 185–208, 2004.
- [10] A. Berger, "Magnetic resonance imaging," *BMJ*, vol. 324, no. 7328, p. 35, Jan. 2002.
- [11] P. Marzola, F. Osculati, and A. Sbarbati, "High field MRI in preclinical research," *Eur. J. Radiol.*, vol. 48, no. 2, pp. 165–170, Nov. 2003.
- [12] G. C. Kagadis, G. Loudos, K. Katsanos, S. G. Langer, and G. C. Nikiforidis, "In vivo small animal imaging: Current status and future prospects," *Med. Phys.*, vol. 37, no. 12, pp. 6421–6442, 2010.
- [13] Y. H. Huang, T. H. Wu, M. H. Lin, C. C. Yang, W. Y. Guo, Z. J. Wang, C. L. Chen, and J. S. Lee, "An automated robot arm system for small animal tissue biopsy under dual-image modality," *Nucl. Instrum. Methods Phys. Res. Sect. Accel. Spectrometers Detect. Assoc. Equip.*, vol. 569, no. 2, pp. 230–234, Dec. 2006.
- [14] J. C. Elliott and S. D. Dover, "X-ray microtomography," *J. Microsc.*, vol. 126, no. 2, pp. 211–213, 1982.
- [15] S. J. Schambach, S. Bag, L. Schilling, C. Groden, and M. A. Brockmann, "Application of micro-CT in small animal imaging," *Methods*, vol. 50, no. 1, pp. 2–13, Jan. 2010.
- [16] S. Bartling, W. Stiller, W. Semmler, and F. Kiessling, "Small Animal Computed Tomography Imaging," *Curr. Med. Imaging Rev.* vol. 3, no. 1, pp. 45–59, 2007.
- [17] J. M. Boone, O. Velazquez, and S. R. Cherry, "Small-Animal X-ray Dose from Micro-CT," *Mol. Imaging*, vol. 3, no. 3, pp. 149–158, Jul. 2004.
- [18] F. S. Foster, M. Y. Zhang, Y. Q. Zhou, G. Liu, J. Mehi, E. Cherin, K. A. Harasiewicz, B. G. Starkoski, L. Zan, D. A. Knapik, and S. L. Adamson, "A new ultrasound instrument for in vivo microimaging of mice," *Ultrasound Med. Biol.*, vol. 28, no. 9, pp. 1165–1172, Sep. 2002.
- [19] F. Kiessling and B. J. Pichler, *Small Animal Imaging: Basics and Practical Guide*. Springer, 2010.
- [20] F. Cavaliere, M. Zhou, and M. Ashokkumar, "The Design of Multifunctional Microbubbles for Ultrasound Image-Guided Cancer Therapy," *Curr. Top. Med. Chem.*, vol. 10, no. 12, pp. 1198–1210, 2010.
- [21] P. D. Bos, D. X. Nguyen, and J. Massagué, "Modeling metastasis in the mouse," *Curr. Opin. Pharmacol.*, vol. 10, no. 5, pp. 571–577, Oct. 2010.
- [22] M. Rodriguez-Porcel, O. Gheysens, I. Y. Chen, J. C. Wu, and S. S. Gambhir, "Image-Guided Cardiac Cell Delivery Using High-Resolution Small-Animal Ultrasound," *Mol. Ther.*, vol. 12, no. 6, pp. 1142–1147, Dec. 2005.
- [23] R. Khadem, C. C. Yeh, M. Sadeghi-Tehrani, M. R. Bax, J. A. Johnson, J. N. Welch, E. P. Wilkinson, and R. Shahidi, "Comparative tracking error analysis of five different optical tracking systems," *Comput. Aided Surg.*, vol. 5, no. 2, pp. 98–107, Jan. 2000.

- [24] F. S. Foster, J. Mehi, M. Lukacs, D. Hirson, C. White, C. Chaggares, and A. Needles, "A New 15–50 MHz Array-Based Micro-Ultrasound Scanner for Preclinical Imaging," *Ultrasound Med. Biol.*, vol. 35, no. 10, pp. 1700–1708, Oct. 2009.
- [25] A. Liu, "Alteration of limb and brain patterning in early mouse embryos by ultrasound-guided injection of Shh-expressing cells," *Mech. Dev.*, vol. 75, no. 1–2, pp. 107–115, Jul. 1998.
- [26] M. Olsson, K. Campbell, D. Turnbull, "Specification of Mouse Telencephalic and Mid-Hindbrain Progenitors Following Heterotopic Ultrasound-Guided Embryonic Transplantation," *Neuron*, vol. 19, no. 4, pp. 761–772.
- [27] M. Matinfar, "Image-guided small animal radiation research platform: calibration of treatment beam alignment," *Phys. Med. Biol.*, vol. 54, no. 4, pp. 891–905, Jan. 2009.
- [28] S. Nicolau, L. Mendoza-Burgos "In vivo evaluation of a guidance system for computer assisted robotized needle insertion devoted to small animals." *Medical Imaging and Augmented Reality*. Springer Berlin Heidelberg, 2008. 241-250.
- [29] A. C. Waspe, "Development of a robotic needle positioning system for three-dimensional image-guided interventions in small animals," University of Western Ontario, 2009.
- [30] J. S. Bax, C. S. R. Waring, S. Sherebrin, S. Stapleton, T. J. Hudson, D. A. Jaffray, J. C. Lacefield, and A. Fenster, "3D image-guided robotic needle positioning system for small animal interventions," *Med. Phys.*, vol. 40, no. 1, p. 011909, 2013.
- [31] A. C. Waspe, A. Chau, A. Kukic, R. Chopra, and K. Hynynen, "An MRI-compatible three-axis focused ultrasound system for performing drug delivery studies in small animal models," *Proc. SPIE*, 2010.
- [32] E. Hempel, H. Fischer, L. Gumb, T. Höhn, H. Krause, U. Voges, H. Breitwieser, B. Gutmann, J. Durke, M. Bock, and A. Melzer, "An MRI-Compatible Surgical Robot for Precise Radiological Interventions," *Comput. Aided Surg.*, vol. 8, no. 4, pp. 180–191, Jan. 2003.
- [33] P. Kazanzides, "Development of an image-guided robot for small animal research," *Comput. Aided Surg.*, vol. 12, no. 6, pp. 357–365, Jan. 2007.
- [34] O. Bebek, M. J. Hwang, B. Fei, and M. C. Cavusoglu, "Design of a small animal biopsy robot," in *30th Annual International Conference of the IEEE Engineering in Medicine and Biology Society, 2008. EMBS 2008*, 2008, pp. 5601–5604.
- [35] O. Bebek, "Design of a Parallel Robot for Needle-Based Interventions on Small Animals," *IEEEASME Trans. Mechatron.*, vol. 18, no. 1, pp. 62–73, Feb. 2013.
- [36] L. Ramrath, U. G. Hofmann, and A. Schweikard, "A robotic assistant for stereotactic neurosurgery on small animals," *Int. J. Med. Robot.*, vol. 4, no. 4, pp. 295–303, Dec. 2008.
- [37] A. C. Waspe, "Design, calibration and evaluation of a robotic needle-positioning system for small animal imaging applications," *Phys. Med. Biol.*, vol. 52, no. 7, pp. 1863–1878, Jan. 2007.
- [38] A. C. Waspe, D. D. McErlain, V. Pitelka, D. W. Holdsworth, J. C. Lacefield, and A. Fenster, "Integration and evaluation of a needle-positioning robot with volumetric microcomputed tomography image guidance for small animal stereotactic interventions," *Med. Phys.*, vol. 37, no. 4, pp. 1647–1659, Apr. 2010.
- [39] R. H. Taylor, J. Funda, B. Eldridge, S. Gomory, K. Gruben, D. LaRose, M. Talamini, L. Kavoussi, and J. Anderson, "A telerobotic assistant for laparoscopic surgery," *IEEE Eng. Med. Biol. Mag.*, vol. 14, no. 3, pp. 279–288, 1995.
- [40] M.J. Huang, O. Bebek, F. Liang, B. Fei, M. C. Cavusoglu, "Kinematic Calibration of a Parallel Robot for Small Animal Biopsies," *IEEE/RSJ International Conference on Intelligent Robots and Systems*, Oct. 2009
- [41] C. S. R. Waring, *Development of a three-dimensional image-guided needle positioning system for small animal interventions*. London, Ont: School of Graduate and Postdoctoral Studies, University of Western Ontario, 2012.
- [42] J. Bax, "New Mechatronic Systems for the Diagnosis and Treatment of Cancer," *Univ. West. Ont. - Electron. Thesis Diss. Repos.*, Apr. 2012.
- [43] K. S. Arun, T. S. Huang, and S. D. Blostein, "Least-Squares Fitting of Two 3-D Point Sets," *IEEE Trans. Pattern Anal. Mach. Intell.*, vol. PAMI-9, no. 5, pp. 698–700, 1987.
- [44] J. Cepek, B. A. Chronik, U. Lindner, J. Trachtenberg, S. R. H. Davidson, J. Bax, and A. Fenster, "A system for MRI-guided transperineal delivery of needles to the prostate for focal therapy," *Med. Phys.*, vol. 40, no. 1, p. 012304, Jan. 2013.
- [45] J. M. Fitzpatrick, "Predicting error in rigid-body point-based registration," *Med. Imaging IEEE Trans. On*, vol. 17, no. 5, pp. 694–702.
- [46] J. M. Fitzpatrick, "Fiducial registration error and target registration error are uncorrelated," 2009, *Proc. SPIE 7261, Medical Imaging 2009: Visualization, Image-Guided Procedures, and Modeling*, vol. 7261, pp. 726102–726102–12.

- [47] J. B. West, J. M. Fitzpatrick, S. A. Toms, C. R. J. Maurer, and R. J. Maciunas, "Fiducial Point Placement and the Accuracy of Point-based, Rigid Body Registration," *Neurosurg. April 2001*, vol. 48, no. 4, pp. 810–817, 2001.
- [48] G. Reusz, P. Sarkany, J. Gal, and A. Csomos, "Needle-related ultrasound artifacts and their importance in anaesthetic practice," *Br. J. Anaesth.*, vol. 112, no. 5, pp. 794–802, May 2014.
- [49] B. D. Sites, "Artifacts and Pitfall Errors Associated With Ultrasound-Guided Regional Anesthesia. Part I: Understanding the Basic Principles of Ultrasound Physics and Machine Operations," *Reg. Anesth. Pain Med.*, vol. 32, no. 5, pp. 412–418.
- [50] M. K. Feldman, S. Katyal, and M. S. Blackwood, "US artifacts," *Radiogr. Rev. Publ. Radiol. Soc. N. Am. Inc.*, vol. 29, no. 4, pp. 1179–1189, Aug. 2009.
- [51] V. Filatov, "Reverberation in ultrasound flow meters," *Meas. Tech.*, vol. 36, no. 3, pp. 301–304, Mar. 1993.
- [52] J. G. Baun, *Vascular Ultrasound: Physics, Instrumentation, and Hemodynamics*. ProSono Publishing, 2010.
- [53] V. Cerundolo, I. F. Hermans, and M. Salio, "Dendritic cells: a journey from laboratory to clinic," *Nat. Immunol.*, vol. 5, no. 1, pp. 7–10, Jan. 2004.
- [54] "Dendritic cell-based vaccines in cancer immunotherapy: an update on clinical and immunological results," *Ann. Oncol.*, vol. 15, pp. iv145–iv151.
- [55] F. O. Nestle, A. Farkas, and C. Conrad, "Dendritic-cell-based therapeutic vaccination against cancer," *Curr. Opin. Immunol.*, vol. 17, no. 2, pp. 163–169, Apr. 2005.
- [56] P. Verdijk, E. H. J. G. Aarntzen, W. J. Lesterhuis, A. C. I. Boullart, E. Kok, M. M. van Rossum, S. Strijk, F. Eijckeler, J. J. Bonenkamp, J. F. M. Jacobs, W. Blokk, J. H. J. M. vanKrieken, I. Joosten, O. C. Boerman, W. J. G. Oyen, G. Adema, C. J. A. Punt, C. G. Figdor, and I. J. M. de Vries, "Limited Amounts of Dendritic Cells Migrate into the T-Cell Area of Lymph Nodes but Have High Immune Activating Potential in Melanoma Patients," *Clin. Cancer Res.*, vol. 15, no. 7, pp. 2531–2540, Apr. 2009.
- [57] E. Gilboa, "DC-based cancer vaccines," *J. Clin. Invest.*, vol. 117, no. 5, pp. 1195–203, May 2007.
- [58] W. L. Smith, K. J. M. Surry, G. R. Mills, D. B. Downey, and A. Fenster, "Three-dimensional ultrasound-guided core needle breast biopsy," *Ultrasound Med. Biol.*, vol. 27, no. 8, pp. 1025–1034, Aug. 2001.
- [59] S. Schultze-Mosgau, H. Schliephake, M. Radespiel-Tröger, and F. W. Neukam, "Osseointegration of endodontic endosseous cones Zirconium oxide vs titanium," *Oral Surg. Oral Med. Oral Pathol. Oral Radiol. Endodontology*, vol. 89, no. 1, pp. 91–98, Jan. 2000.
- [60] B. W. Miller, J. W. Moore, H. H. Barrett, T. Frye, S. Adler, J. Sery, and L. R. Furenlid, "3D printing in X-ray and Gamma-Ray Imaging: A novel method for fabricating high-density imaging apertures," *Nucl. Instrum. Methods Phys. Res. Sect. Accel. Spectrometers Detect. Assoc. Equip.*, vol. 659, no. 1, pp. 262–268, Dec. 2011.
- [61] Stratasys Ltd. © 2014, "Objet30 Pro Specifications." <http://www.stratasys.com/3d-printers/design-series/objet30-pro>.
- [62] N. Abolhassani, "Control of soft tissue deformation during robotic needle insertion," *Minim. Invasive Ther. Allied Technol.*, vol. 15, no. 3, pp. 165–176, Jan. 2006.
- [63] R. Alterovitz and K. Goldberg, "Needle insertion and radioactive seed implantation in human tissues: Simulation and sensitivity analysis," in *Proc. IEEE Int. Conf. on Robotics and Automation*, 2003, pp. 1793–1799.
- [64] V. Lagerburg, "Development of a tapping device: a new needle insertion method for prostate brachytherapy," *Phys. Med. Biol.*, vol. 51, no. 4, pp. 891–902, Jan. 2006.
- [65] T. K. Podder, D. P. Clark, D. Fuller, J. Sherman, W. S. Ng, L. Liao, D. J. Rubens, J. G. Strang, E. M. Messing, Y. D. Zhang, and Y. Yu, "Effects of Velocity Modulation during Surgical Needle Insertion," in *Engineering in Medicine and Biology Society, 2005. IEEE-EMBS 2005. 27th Annual International Conference of the*, 2005, pp. 5766–5770.
- [66] A. M. Okamura, "Force modeling for needle insertion into soft tissue," *Biomed. Eng. IEEE Trans. On*, vol. 51, no. 10, pp. 1707–1716.

Curriculum Vitae

Adem Nadjib Hadj Boussaad, B.E.Sc., M.E.Sc (Candidate), E.I.T

EDUCATION

- May 2012 – present Master's of Biomedical Engineering – Imaging/Robotics (Candidate)
Department of Biomedical Engineering
University of Western Ontario (UWO), London, Canada
Supervisor: James Lacefield, Ph.D, P.Eng.
Thesis: “Ultrasound-Guided Mechatronic System for Targeted Delivery of Cell-Based Cancer Vaccine Immunotherapy in Preclinical Models”
- 2008 – 2012 Bachelor of Electrical Engineering (Distinction Award)
Biomedical Signals and Systems specialization
Department of Electrical and Computer Engineering
UWO, London, Canada

POSITIONS

- 2012 – present Research Assistant, Graduate
Robarts Research Institute, London, Ontario, Canada
Supervisor: James Lacefield, Ph.D, P.Eng.
Collaborator: Aaron Fenster, Ph.D, FCCPM
Project: “Registration of High-Frequency Ultrasound to a Mechatronic System for Preclinical Interventions”
- 2013 Graduate Teaching Assistant
BME 9509 - Introduction to Digital Image Processing
Instructor: Dr. Hanif Ladak, PhD, P.Eng.
Department of Electrical and Computer Engineering, UWO, Canada
- 2012 Graduate Teaching Assistant
ECE 2205A – Electric Circuits I
Department of Electrical and Computer Engineering, UWO, London, Canada
- 2011 Research Assistant, Undergraduate
Department of Medical Biophysics, UWO, London, Canada
Supervisor: Charles McKenzie, Ph.D
Project: Development of hands-on learning guide to MRI fundamentals using Terranova-MRI: Earth's Field MRI Teaching System

ACADEMIC AWARDS, SCHOLARSHIPS and DISTINCTIONS

- 2013 – Ontario Graduate Scholarship (OGS), Province of Ontario
2014 Provincial, **\$15000**
- 2012 – NSERC – Collaborative Research and Training Experience Program Scholar
2014 UWO, London, Canada
Awarded to highly qualified graduate students and post-doctoral fellows involved in developing innovative interventional technologies and techniques for surgery and therapy.
Institutional
\$24000
- 2012 – Western Graduate Research Scholarship, UWO
2014 *Awarded to full time graduate student for stipend support who has maintained an average of 80% or more.*
Institutional
\$16820
- Jul. 2012 Western “Distinct Graduate” Designation
Awarded to graduating full time undergraduate students who have achieved an overall average of 80% and no grade lower than 70% on the entire program with no failed courses.
Institutional
- 2008 – Four Year Continuing Scholarship, UWO
2012 *Awarded upon admission to Western students who have an admission average above 95% and maintain an average of 80% or more.*
Institutional
\$10000
- 2009 – Dean’s Honour List
2012 *Awarded to full time students who have maintained an average of 80% or more.*
Institutional
- May 2008 A.I. Johnson Entrance Scholarship, UWO
Awarded upon admission to Western Engineering students who have demonstrated academic excellence at the high school level.
Institutional
\$1700

PUBLICATIONS and PRESENTATIONS

Refereed Conference Proceeding (1)

A. Hadj Boussaad, C. Waring, J. Bax, A. Fenster, J. Lacefield. “High-Frequency Ultrasound-Guided Robot for Preclinical Injections in Small-Animal Models”, 36th Annual International Conference of the IEEE Engineering in Medicine and Biology Society, Chicago, Illinois, (08/14)

Peer Reviewed Published Conference Abstracts (7)

A. Hadj Boussaad, C. Waring, J. Bax, A. Fenster, J. Lacefield. “Optimization of High-Frequency Ultrasound-to-Robot Registration to Meet Workflow Requirements of Preclinical Interventions”. Robarts Research Retreat, London, Ontario, Canada (02/14)

A. Hadj Boussaad, C. Waring, J. Bax, A. Fenster, J. Lacefield. “Optimization of High-Frequency Ultrasound-to-Robot Registration to Meet Workflow Requirements of Preclinical Interventions”. London Imaging Discovery, London, Ontario, Canada (06/14)

A. Hadj Boussaad, C. Waring, J. Bax, A. Fenster, J. Lacefield. “Optimization of High-Frequency Ultrasound-to-Robot Registration to Meet Workflow Requirements of Preclinical Interventions”. London Health Research Day, London, Ontario, Canada (03/14)

A. Hadj Boussaad, C. Waring, J. Bax, A. Fenster, J. Lacefield. “Optimization of High-Frequency Ultrasound-to-Robot Registration to Meet Workflow Requirements of Preclinical Interventions”. Imaging Network Ontario Symposium, Toronto, Ontario, Canada (02/14)

A. Hadj Boussaad, C. Waring, J. Bax, A. Fenster, J. Lacefield. “Registration of High-Frequency Ultrasound to a Mechatronic System for Preclinical Interventions”. London Imaging Discovery, London, Ontario, Canada (06/13)

A. Hadj Boussaad, C. Waring, J. Bax, A. Fenster, J. Lacefield. “Registration of High-Frequency Ultrasound to a Mechatronic System for Preclinical Interventions”. London Health Research Day, London, Ontario, Canada (03/13)

A. Hadj Boussaad, C. Waring, J. Bax, A. Fenster, J. Lacefield. “Registration of High-Frequency Ultrasound to a Mechatronic System for Preclinical Interventions”. Imaging Network Ontario Symposium, Toronto, Ontario, Canada (02/13)

Peer Reviewed Poster Presentations (8) (*presenter)

A. Hadj Boussaad, C. Waring, J. Bax, A. Fenster, J. Lacefield. “High-Frequency Ultrasound-Guided Robot for Preclinical Injections in Small-Animal Models”, Biomedical Engineering Research Day, Western University, London, Ontario, (10/14)

A. Hadj Boussaad*, C. Waring, J. Bax, A. Fenster, J. Lacefield. “High-Frequency Ultrasound-Guided Robot for Preclinical Injections in Small-Animal Models”, 36th Annual International Conference of the IEEE Engineering in Medicine and Biology Society, Chicago, Illinois, (08/14)

A. Hadj Boussaad*, C. Waring, J. Bax, A. Fenster, J. Lacefield. “Optimization of High-Frequency Ultrasound-to-Robot Registration to Meet Workflow Requirements of Preclinical Interventions,Robarts Research Retreat, London, Ontario, Canada (02/14)

A. Hadj Boussaad*, C. Waring, J. Bax, A. Fenster, J. Lacefield. “Optimization of High-Frequency Ultrasound-to-Robot Registration to Meet Workflow Requirements of Preclinical Interventions”. London Health Research Day, London, Ontario, Canada (03/14)

A. Hadj Boussaad*, C. Waring, J. Bax, A. Fenster, J. Lacefield. “Optimization of High-Frequency Ultrasound-to-Robot Registration to Meet Workflow Requirements of Preclinical Interventions”. Imaging Network Ontario Symposium, Toronto, Ontario, Canada (02/14)

A. Hadj Boussaad*, C. Waring, J. Bax, A. Fenster, J. Lacefield. “Registration of High-Frequency Ultrasound to a Mechatronic System for Preclinical Interventions”. London Imaging Discovery, London, Ontario, Canada (06/13)

A. Hadj Boussaad*, C. Waring, J. Bax, A. Fenster, J. Lacefield. “Registration of High-Frequency Ultrasound to a Mechatronic System for Preclinical Interventions”. London Health Research Day, London, Ontario, Canada (03/13)

A. Hadj Boussaad*, C. Waring, J. Bax, A. Fenster, J. Lacefield. “Registration of High-Frequency Ultrasound to a Mechatronic System for Preclinical Interventions”. Imaging Network Ontario Symposium, Toronto, Ontario, Canada (02/13)